UNIVERSITY OF CALIFORNIA

Los Angeles

Directed Shape Morphing of Soft Kirigami Deployables

A dissertation submitted in partial satisfaction
of the requirements for the degree
Doctor of Philosophy in Mechanical Engineering

by

Mrunmayi Mungekar

2024

ABSTRACT OF THE DISSERTATION

Directed Shape Morphing of Soft Kirigami Deployables

by

Mrunmayi Mungekar
Doctor of Philosophy in Mechanical Engineering
University of California, Los Angeles, 2024
Professor Mohammed Khalid Jawed, Co-Chair
Professor Vwani P. Roychowdhury, Co-Chair

This study explores deployable structures inspired by nature's morphogenesis, where biological systems inherently develop complex forms autonomously. Applying these principles, this research proposes a new approach where materials self-organize and morph from two-dimensional to three-dimensional shapes without traditional manufacturing constraints. Deployable structures offer significant advantages in compactness, simplifying storage and transportation, making them particularly valuable in fields like aerospace and biomedicine where tailored, precise forms are crucial. However, the transformation from planar to three-dimensional structures presents substantial challenges due to complex design interdependencies. To address this, the research develops kirigami based structures capable of deploying from a planar to a 3D shapes. Furthermore, these possess the ability of switching between stable states without continuous energy input, enhancing their functionality for various applications. Additionally, the study tackles the inverse design challenge through a novel integration of machine learning, optimizing design parameters for specific functional needs efficiently. This approach not only bridges the gap between static planar manufacturing and dynamic structural functionality but also creates a platform for a more intuitive, equipment-frugal way to tackle deployable systems, setting the stage for future innovations in the field.

The dissertation of Mrunmayi Mungekar is approved.

Mohiuddin Quadir

Jonathan Hopkins

Vwani P. Roychowdhury, Committee Co-Chair

Mohammed Khalid Jawed, Committee Co-Chair

University of California, Los Angeles

2024

TABLE OF CONTENTS

1 Introduction **1**

2 Soft Kirigami Deployables **6**

2.1 Background 6

2.2 Methodology 7

2.3 Variation of design parameters 9

2.4 Application to Wearables in Biomedicine 10

2.5 Drug Delivery Patches for Mice 11

2.6 Biocompatible Materials 12

2.7 Conclusion 13

3 Bistable Kirigami Deployables **15**

3.1 Motivation for Bistability 15

3.2 Design concept 17

3.3 Experimental Manufacturing 18

3.4 Material Modelling 21

3.5 Numerical Simulations 22

3.6 Analytical Formulation 27

3.7 Parametric Variation 31

3.8 Switching Force 32

3.9 Reversibility 35

3.10 Multistability 36

3.11 Soft Gripper 37

3.11.1 Introduction 37

3.11.2 Analytical Formulation . . . 39
3.12 Autonomous Flytrap . . . 41
3.12.1 Introduction . . . 41
3.12.2 Analytical Formulation . . . 42
3.13 Bistable Actuator . . . 43
3.13.1 Introduction . . . 43
3.13.2 Material Modelling . . . 45
3.13.3 Numerical Simulations . . . 49
3.14 Conclusion . . . 52

4 Inverse Design Algorithm for Kirigami Deployables . . . 53
4.1 Introduction . . . 53
4.2 Numerical Simulations . . . 55
4.3 Experiments . . . 57
4.4 Machine Learning Inverse Design Framework . . . 57
4.4.1 Overview . . . 57
4.4.2 Dimension Reduction: Efficient Encoding of Kirigami Patterns . . . 58
4.4.3 Active Learning for Optimizing Kirigami Designs . . . 58
4.4.4 Generation of Candidate Kirigami Patterns . . . 59
4.4.5 Optimization Process and Evaluation Metrics . . . 59
4.5 Exploration Design of Various 3D Kirigami Shapes . . . 62
4.6 3D Scanning and Point-by-Point Analysis . . . 65
4.7 Extension to trilayer structures . . . 67
4.8 Conclusion . . . 70

5 Shrinky Dink based Kirigami Deployables . . . 71

5.1 Motivation 71
5.2 Methodology 73
5.3 Experimental Method 74
5.4 Temperature Logging 76
5.5 Material Modelling 77
5.6 Numerical Simulation 79
5.7 Variation of Shapes 81
5.7.1 Heuristic understanding 81
5.7.2 Machine Learning assisted understanding 82
5.7.3 Combination of Existing Shapes 84
5.8 Parametric Variation 85

6 Conclusions **88**

LIST OF FIGURES

2.1 (A) Of two circular layers, the bottom layer is stretched and adhered to the unstretched top layer to obtain a soft composite. Upon releasing the constraints, the strain mismatch between the two layers induces symmetry breaking and the composite may assume a buckled shape (B) Arbitrary buckling shapes (experimental) of different prestretches [14] 8

2.2 Replacing the top circular layer with a kirigami layer (layer with cuts) can lead to a preprogrammed shape via the same procedure as before. The shape is governed by the kirigami pattern. In this case, the goal was to obtain an axisymmetrical cap.[14] 9

2.3 (A) Experimental images and (B) snapshots from finite element simulations at different values of prestretch: 1)$\lambda = 1.05$, 2) $\lambda = 1.15$, 3)$\lambda = 1.2$, and 4) $\lambda = 1.25$ to obtain the preprogrammed shapes [14] 10

2.4 Overview of the medical band (A) Shape and dimensions of the kirigami and (unstretched) substrate layer for manufacturing the bands (B) The mouse plush wearing the band designed for it 12

2.5 Medical patches made of different materials (A) VHB Substrate (B) Duraflex Substrate 13

3.1 Overview of the bistable soft structure design. The combination of two kirigami layers and strain mismatch creates 3D soft structures that are fully soft and bistable [67] 17

3.2 Experimental setup. (A1-A4) CAD model of the experimental setup (B1) Schematic representation of the system consist of two-knob stages on 250 mm tracks with reference segments in red (B2) Snapshot of the system when the substrate layer is stretched visible by the red stretched segments (B3) Attach one kirigami layer below the substrate layer, and the other one on top of the substrate layer (B4) Release the pre-stretch by cutting along the outline of the circular substrate. [67] 19

3.3 (A) Side view of the trilayer pyramid 2D precursor, and the free buckling shape of the trilayer pyramid 3D structure (B) Preliminary variation of normalized height as a function of the pre-stretch ($L = 60$ mm) [67] 20

3.4 Engineering stress-strain curves from the UTM Tensile testing data with the Mooney-Rivlin curve fit for (A) Substrate (B) Gray Kirigami (C) White Kirigami. 23

3.5 ABAQUS numerical simulations (A) 2D Mesh in MATLAB (B) (i) Undeformed trilayer structure showing the three main layers of the composite (ii) A close-up view of the multiple sublayers in the structure (C) Deformed configuration [67] . 25

3.6 (A-B) Effect of the mesh on final height output. (C-D) Effect of the mesh on simulation time. (A)(C) Varying mesh element size for L=60mm. (B)(D) Varying number of nodes along the thickness of each composite layer for L=60mm, $\lambda =$ 1.6 [67] 27

3.7 A) Cross-sectional view of the trilayer and bilayer composite structure (B) Sketch of the side view for a pyramid with height H. (C) Sketch of the side view for a spherical cap with height H [67] 28

3.8 (A) Comparison of the free-buckling shapes in (A1-A4) simulation and (B1-B4) experiment for the cross-shaped kirigami composite structure (L=40 mm) at different amount of pre-stretch $\lambda = 1.2, 1.4, 1.6, 1.8, 2.0$. The colorbars correspond to the distribution of stress in the deformed trilayer structure [67] 31

3.9 (A-C) The variation of the normalized height of the free-buckling shape as a function of the pre-stretch. Three examples showing different length/thickness ratio with diameter/width ratio fixed. (A) $\frac{L}{t_s} = 40$. (B) $\frac{L}{t_s} = 60$. (C) $\frac{L}{t_s} = 80$. (D) Variation of the energy landscape at different pre-stretch. Below a certain threshold, the composite structure hardly buckles [67] 33

3.10 (A) Experimental setup for measuring the switching force during indentation (B) To demonstrate its bistability, the force-displacement curve of the trilayer soft structure was obtained experimentally, indicating that the structure can switch from one stable configuration to the other. The force required to change the state is defined as the switching force. (C) Variation of switching force required to switch between the two configurations (L = 60mm) [67] 34

3.11 Cycling test of a bistable dome. The height of the dome as a function of cycling number over time. The switching of the dome between its two was achieved by manual manipulation by hands. After every 50 cycles, we measured the heights in both positive and negative configurations [67]. 35

3.12 (A) Sketches of free-buckling mode shape 1 and mode shape 2 in the "positive" and "negative" configurations. (B) The free buckling shapes for the cross-shaped kirigami composite structure (L = 80 mm) at different amount of pre-stretch λ = 1.2, 1.4, 1.6, 1.8, 2.0. The Mode 1 and Mode 2 are also predicted in simulations. (C) The simulated variation of normalized height of the two modes in the "positive" and "negative" configurations as a function of pre-stretch λ [67] . . . 37

3.13 A) The mechanism of a soft griper composed of a bistable dome actuated by an extending shape memory alloy(SMA) spring. (B) The detailed structure of the gripper with labels. (C) The gripper has the ability to gently grasp delicate objects of different shapes and sizes [67] 38

3.14 The sketch of a gripper grasping an object of mass m [67] 40

3.15 (A) This strategy can be mimicked by mechanically embedding sensing and actuation into structures by using a bistable dome. (B) A magnet was inserted into the bottom of the object. With the help of the magnetic force, the snap-through of the dome could be directly triggered by the touch of the toy. (C) Snapshots show the autonomous object detection and quick closing of leaves without requiring external sensing, control, and actuation. To help overcome the energy barrier of the bistable dome, we attached a permanent magnetic bead on the bottom of the object while placing another one underneath the platform [67]. 42

3.16 (A) Schematic view of bistable actuator (B) Picture of bistable actuator triggered from state I to state II (C) Creation of the frame with the included SMA wire (D) Putting together the layers - the two frames and the stretched membrane - of the composites to create the bistable actuator [71]. 44

3.17 (A) The stretch-stress curve fitting result of the Yeoh model. (B) The comparison of the Yeoh model's prediction of stable-state angle and the experimental data points. (C) The stretch-stress curve fitting result of the Ogden model. (D) The comparison of the Ogden model's prediction of stable-state angle and the experimental data points. (E) The stretch-stress curve fitting result of the Mooney-Rivlin model. (F) The comparison of the Mooney-Rivlin model's prediction of stable-state angle and the experimental data points [71]. 46

3.18 Testing the flexural rigidity of the frame (A) The default placement of the load cell and the stacked frame with a nonstretched VHB^{TM} membrane. (B) The structure bends to form a curved shape under a buckling load [71]. 48

3.20 Initial curvature of bistable actuator for experimental, analytic (Ogden) model and numerical simulation with different prestretch (λ_p) [71]. 50

3.19 Numerical simulation result. (A) Deformation and (B) stress result when λ_p = 1.3. (C) Deformation and (D) stress result when λ_p = 1.8. (E) Deformation and (F) stress result when λ_p = 2.4. (G) Deformation and (H) stress result when λ_p = 2.8 [71]. 51

4.1 Flow chart of the data-driven design and optimization of soft kirigami composite. A(i) A VAE to reduce the dimension of kirigami patterns to a small number of latent variables. A(ii) A Bayesian Optimization loop that iteratively searches the optimal combination of latent kirigami pattern variables, size of the structure, and amount of prestretch that results to the target 3D topology [81]. 55

4.2 Experimental setup. A(i) Schematic representation of the system consist of two-knob stages (1) on 250 mm tracks (2) knobs to adjust the stage location. A(ii) Snapshot of the system when the substrate layer (3) is stretched. A(iii) Attach a kirigami layer (4) on top of the substrate layer. A(iv) Release the prestretch by cutting along the outline of the circular substrate [81]. 57

4.3 (A) Kirigami patterns that have reflectional symmetry. (B) Kirigami patterns that have four-fold radial symmetry [81]. 59

4.4 A) Search trajectory Variation of SSIM between target peanut shape and predicted free buckling shape over iterations. B) Multiple optimal solutions B1–B4)The top four optimal design solutions, including the kirigami patterns, prestretch and kirigami size. The corresponding height distribution for each design is presented at the bottom. [81]. 61

4.5 Inverse design of shapes with two reflectional axes of symmetry: Target 3D shapes: the first column shows different 3D shapes (A. a peanut, B. a pringle, and C. a ship hull) input to the optimization algorithm. Height-coded 2D image representations: the second column shows distribution of height for the target 3D shape. Optimal design parameters: the third column presents the optimized kirigami patterns, prestretch, and radius selected after 100 iterations. Height-coded 2D image representations of the optimal predicted shapes: the fourth column presents the height distribution of predicted 3D topology obtained from finite element simulation using the optimal design parameters. The SSIM are approximately in 0.9. The predicted 3D shapes: the fifth column shows the predicted 3D shape in simulation. The maximum heights for the 3D images are shown in the bottom. Experimentally realized morphing 3D soft structures with desired shapes: the sixth column shows the experimental result of the 3D topology given the optimal parameters [81] 63

4.6 Inverse design of shapes with four-fold radial symmetry: Target 3D shapes: the first column shows different 3D shapes (A. a pyramid, and, B. a flower) input to the optimization algorithm. Height-coded 2D image representations: the second column shows distribution of height for the target 3D shape. Optimal design parameters: the third column presents the optimized kirigami patterns, prestretch, and radius selected after 100 iterations. Height-coded 2D image representations of the optimal predicted shapes: the fourth column presents the height distribution of predicted 3D topology obtained from finite element simulation using the optimal design parameters. The SSIM are approximately in 0.9. The predicted 3D shapes: the fifth column shows the predicted 3D shape in simulation. The maximum heights for the 3D images are shown in the bottom. Experimentally realized morphing 3D soft structures with desired shapes: the sixth column shows the experimental result of the 3D topology given the optimal parameters [81] . . 64

4.7 Inverse design of shapes with one axis of asymmetry: Target 3D shapes: the first column shows two different 3D shapes (A. an asymmetric peanut, B. a butterfly) input to the optimization algorithm. Height-coded 2D image representations: the second column shows distribution of height for the target 3D shape. Optimal design parameters: the third column presents the optimized kirigami patterns, prestretch, and radius selected after 100 iterations. Height-coded 2D image representations of the optimal predicted shapes: the fourth column presents the height distribution of predicted 3D topology obtained from finite element simulation using the optimal design parameters. The SSIM are approximately in 0.9. The predicted 3D shapes: the fifth column shows the predicted 3D shape in simulation. The maximum heights for the 3D images are shown in the bottom. Experimentally realized morphing 3D soft structures with desired shapes: the sixth column shows the experimental result of the 3D topology given the optimal parameters [81] 65

4.8 Comparison between experiments and numerical results. A) Qualitative comparison between the experimental 3D scans (gray surface) and the predicted shapes (green point cloud): (i) Peanut (ii) Pringle (iii) Ship (iv) Pyramid (v) Flower (vi) Asymmetric Peanut (vii) Butterfly. B) Quantitative comparison: The bar graph shows the relative error between experiments and numerics across various shapes considered in this paper. The error bars represent standard deviation of the error [81]. 67

4.9 Comparison of the free buckling shape for bilayer and trilayer soft kirigami composite. The kirigami patterns is fixed, and the structures can create three target shapes (A) Unilobe structure. (B) Bilobe structure. (C) Structure with negative Gaussian curvature. First column: kirigami patterns in red and circular substrate in blue. Second column: Bilayer structure with specific combination of pre-stretch and initial radius. Third column: Trilayer structure with the same combination of pre-stretch and initial radius as the bilayer counterpart. Fourth column: Trilayer structure with adjusted pre-stretch and radius [81]. 69

5.1 Introduction to Kirigami-Enhanced Shrinky Dink 3D Morphing A(i-ii) Nature portrays no-interference, growth-based morphology in various organisms (Images reproduced with permission from Sharon et.al. [5]) B(i-ii) The Shrinky Dink deployables mimic this process to morph from one form to other without design interference. C Using this technology, one can simply use easily available equipment to create practical objects such as (i) Soup bowl and spoon (ii) Functional mouse cover [84] 72

5.2 Schematic of the Shrinky Dink deployable method: Start by designing a kirigami pattern. Adhere it firmly with a Shrinky Dink sheet to create a Shrinkle composite. When ready, heat the composite, to deploy it to the 3D shape [84] . . . 74

5.3 Experimental process to manufacture Shrinky Dink deployables A(i) Cut or 3D print a kirigami design A(ii) Glue it firmly to a Shrinky Dink layer of suitable shape A(iii) When cured, heat the composite in the oven at home A(iv) The final shape of the composite [84] 76

5.4 This represents the temperature log portraying the fluctuation of temperature over the entire deformation process. It also displays the start time of the deformation [84] 77

5.5 This represents the material modelings of the involved materials: (A(i))Stress strain response of the Shrinky Dink sheet (A(ii))Stress strain response of the ABS layer (B) Thermal contraction of a designated square piece of each material on placing in an oven [84] 79

5.6 This represents the creation of the Shrinky Dink deployables through heuristic designs: (A) a hemispherical bowl, (B) a pyramid, (C) a shell and, (D) a mouse cover. The first column shows the inspiration [86] behind creating the shape, the second column shows the kirigami and Shrinky Dink shapes used to manufacture it and the third column displays the final manufactured shape [84] 83

5.7 This represents the creation of the Shrinky Dink deployables using the inverse algorithm [81]: (A) a peanut and, (B) a butterfly. The first column shows the inspiration [86] behind creating the shape, the second column shows the kirigami and Shrinky Dink shapes used to manufacture it and the third column displays the final manufactured shape [84] 84

5.8 This represents the creation of the Shrinky Dink deployables through combination of existing shapes: (A) The positioning of the Shrinky Dink and kirigami layers to create a shape with a smoothly changing curvature. (B) The first column shows the inspiration [86] behind creating the shape, the second column shows the kirigami and Shrinky Dink shapes used to manufacture it and the third column displays the final manufactured shape (i) a spoon (ii) a rimmed bowl 85

5.9 Variation of the 3D shape with change in radius ratio (A) A sketch of the various dimensions used in the parametric variation in (i) planar form (ii) 3D shape (obtained via simulations) (B) A graph portraying the experimental and the numerical variation of height with respect to radius ratio γ (C) Variation of height in experimental specimens with change in γ [84] 86

ACKNOWLEDGMENTS

I extend my deepest gratitude to my advisor, Prof. M. Khalid Jawed, whose unwavering guidance and supervision have been indispensable throughout this journey. His insights and expertise have profoundly shaped my research experience and academic growth. I am immensely thankful to all the esteemed professors at UCLA and beyond, from whom I have had the privilege to learn. Their teachings have enriched my understanding and contributed significantly to my scholarly development. Special thanks to my closest colleague, Prof. Leixin Ma, whose collaboration was crucial to the completion of my thesis. I am equally grateful to the numerous Postdocs and Ph.D. students whose contributions, both direct and indirect, have been invaluable to my work. My time at UCLA has been greatly enhanced by the wonderful company of my graduate friends at the SCI Lab. Their camaraderie and support made this challenging journey enjoyable and memorable. I owe a debt of gratitude to the undergraduates I had the opportunity to mentor. Through our interactions, they have taught me much, enriching my experience and broadening my perspectives. Last but certainly not least, I thank my parents, my brother, and my grandmother for their unyielding emotional support throughout the highs and lows of this Ph.D. journey. A special mention to my closest friends in Los Angeles who have become my family away from home, and especially to Varun, whose support has been crucial in helping me navigate through the toughest moments of mental blocks.

VITA

2016–2020 B.Tech., Mechanical Engineering, Indian Institute of Technology (IIT) Bombay, Mumbai, Maharashtra, India

2021–2024 Ph.D. Candidate, Mechanical Engineering, University of California Los Angeles, Los Angeles, California, USA

PUBLICATIONS AND PRESENTATIONS

[1] D. K. Patel, X. Huang, Y. Luo, **M. Mungekar**, M. K. Jawed, L. Yao, C. Majidi, "Highly Dynamic Bistable Soft Actuator for Reconfigurable Multimodal Soft Robots". *Advanced Materials Technologies*, 2023, 8, 2201259

[2] **M. Mungekar**, L. Ma, W. Yan, V. Kackar, S. Shokrzadeh, M. K. Jawed., "Design of Bistable Soft Deployable Structures via a Kirigami-Inspired Planar Fabrication Approach". *Advanced Materials Technologies*, 2023, 8, 2300088

[3] L. Ma, **M. Mungekar**, V. Roychowdhury, M. K. Jawed, "Rapid Design of Fully Soft Deployable Structures Via Kirigami Cuts and Active Learning". *Advanced Materials Technologies*, 2024, 2301305

[4] **M. Mungekar**, M. R. Shankar, M. K. Jawed, "Directed Shape Morphing using Kirigami-enhanced Thermoplastics". *Unpublished manuscript*

[5] M. K. Jawed, **M. Mungekar**, V. Kackar, S. Shokrzadeh, L. Ma, W. Yan, V. Roychowdhury, "Soft Kirigami Composite that Deploys into Pre-programmed Shapes", *Bulletin of the American Physical Society*, 2022

[6] M. K. Jawed, Y. Du, **M. Mungekar**, "A Modular Approach to Discrete Differential Geometry-based Simulation of Soft Robots", *Bulletin of the American Physical Society*, 2022

[7] L. Ma, **M. Mungekar**, V. Roychowdhury, M. K. Jawed, "A machine learning-aided approach to the rapid design of kirigami-inspired soft deployable structures", *Bulletin of the American Physical Society*, 2023

[8] **M. Mungekar**, V. Kackar, S. Shokrzadeh, L. Ma, W. Yan, V. Roychowdhury, M. K. Jawed "A study of pre-programmed soft Kirigami deployables exhibiting multistability", *Bulletin of the American Physical Society*, 2023

[9] **M. Mungekar**, M. R. Shankar, M. K. Jawed, "Shape Morphing with Shrinky Dinks and 3D Printed Kirigami", *SoCal Solids*, 2023

[10] M. Mungekar, L. Ma, W. Yan, V. Kackar, S. Shokrzadeh, M. K. Jawed, "Bistable Soft Kirigami Deployables", *SoCal Robotics*, 2023

[11] **M. Mungekar**, M. R. Shankar, M. K. Jawed, "Shape morphing structures with Shrinky Dink and 3D printed Kirigami", *Bulletin of the American Physical Society*, 2024

CHAPTER 1

Introduction

Morphing structures are a common spectacle in nature. The natural process of morphogenesis is a demonstration of the complexity and innate intelligence embedded within biological systems. It results from the complex interaction between genetic directives and environmental signals, directing the development and organization of life forms at various scales. From the initial embryonic stages that evolve into complex beings, to the intricate folding of the cerebral cortex [1], [2], and the structured arrangement seen in plants and flowers [3]–[5], each example of morphogenesis highlights the ability of biological systems to independently construct architecturally complex structures. These natural phenomena occur without the need for direct, external mechanical manipulation or predefined procedural blueprints, relying instead on a nuanced balance of growth dynamics and complex mechanical interactions. This autonomous assembly process illustrates the potential to embed complexity and functionality within the very fabric of materials, enabling the creation of structures that develop and shape themselves without outside intervention. In stark contrast to traditional manufacturing methods, where the shapes of components and their assembly are rigorously controlled from the outside, the principles of natural morphogenesis inspire a fundamentally different approach to the design of materials and structures. At the heart of this approach is the concept of embedding the "instructions" for shaping and functional assembly directly within the materials themselves, similar to genetic encoding in nature. This strategy suggests a shift away from the conventional dependence on external control systems and detailed procedural guidelines towards a model where materials inherently have the capacity to self-organize and respond to specific environmental stimuli, such as changes in temperature or light. By adopting these principles, it becomes feasible to imagine manufacturing processes that mimic the

spontaneous, self-regulating complexity found in natural systems. This opens up exciting possibilities for the development of materials and structures that are capable of dynamic adaptation and transformation, reflecting the autonomous features of their natural analogs.

This concept of morphogenesis allows for the design and fabrication of structures that are not only innovative but also immensely practical across a variety of applications. First, the compatibility of deployable structures with planar fabrication techniques, such as additive manufacturing, revolutionizes the production of complex devices [6]–[8]. Imagine a scenario where an entire robot, complete with embedded electronics and mechanical systems, is fabricated on a flat surface. Once manufacturing is complete, this robot would deploy into a three-dimensional operational state and walk away, ready for immediate use.

Furthermore, deployable structures offer remarkable convenience due to their compact nature, significantly simplifying storage and transportation. This capability is essential in sectors such as aerospace, where space efficiency is crucial, or in consumer products where portability can greatly enhance usability [9]–[13]. The ability to maintain these structures in a flat state until deployment not only reduces the physical footprint but also aligns with modern needs for efficiency and minimalism.

Additionally, the concept of form-finding in deployable structures allows for the creation of forms precisely tuned to specific functional requirements [14]. This adaptability is particularly valuable in fields such as architecture or biomedical devices, where tailored shapes can enhance interaction with the environment or fit individual anatomical needs [15]–[17]. By achieving any desired target shape, deployable structures can be designed to meet exact specifications, providing solutions that are not only effective but also aesthetically or ergonomically optimized.

The potential applications of deployable structures extend to the fields of emergency shelters, where quick assembly and disassembly are crucial, or in responsive wearables that adapt their form based on environmental or physiological changes. The intrinsic flexibility and adaptability offered by deployable structures, underpinned by the simplicity of their manufacturing and deployment processes, exemplify a significant advancement in how we

design and utilize materials and structures.

However, the challenge of transforming planar structures into predefined three-dimensional forms spans various scales and applications, presenting significant hurdles in engineering. Conventional manufacturing often limits production to two dimensions, making the morphing of these structures into functional 3D surfaces a complex task. This issue is especially critical in technologies where spatial constraints or specific functional forms are necessary, such as in deployable systems or integrated wearable devices. Despite numerous methods previously employed to address this challenge, which we will discuss later in the paper, the essential problem remains: how to effectively and efficiently transition flat designs into their three-dimensional counterparts without sacrificing functionality or structural integrity. This ongoing challenge in material science and engineering drives the need for innovative solutions that can seamlessly integrate adaptive responses to environmental stimuli and mechanical requirements, fundamentally reshaping our approach to material and structural design.

Continuing from the challenge, Zavodnik et al. [14] introduced a method using kirigami cuts within composite materials, enabling the transition from two-dimensional to three-dimensional shapes through controlled strain mismatches between layers. This technique allows precise control over the final 3D form, marking a significant evolution in form-finding technologies. This method's ability to precisely target any desired shape is particularly useful for medical applications as their shapes can adapt to the wearer's body. Herein, we expand upon the design of these structures focusing on such applications in biomedicine, offering new possibilities for minimally invasive treatments.

While the creation of structures that transition from two-dimensional to three-dimensional forms has been achieved, the next frontier lies in enhancing their functionality through multistability. Multistability is vital because it allows these structures to maintain multiple stable states without continuous energy input, crucial for their practical deployment in various environments. Ensuring that these structures can reliably and repeatedly switch between stable configurations under real-world conditions demands precise engineering and innovative material use. For example, in the case of a robot designed to walk out after fabrication on a flat surface, the legs of the robot need to embody this principle of multistability. Each

leg must be capable of assuming at least two stable states to facilitate walking motion. This dual functionality is essential for actuation, where the legs can switch back and forth in a controlled manner, driving the robot's movement. Herein, we extend the concept of soft kirigami deployables to create multistable structures by exploiting geometric symmetries in the design. This approach enables the structures to not only repeatedly switch between their stable configurations but also to assume specific, desired shapes, enhancing their interaction with the environment. Demonstrated uses of these advanced kirigami structures include soft grippers, biomimetic flytraps, and actuators—each benefiting from the minimal energy requirement to switch states and the capacity to take on precise shapes tailored to specific tasks or functions. These developments highlight the potential of kirigami-inspired designs to revolutionize deployable systems across various fields, offering efficient and adaptable solutions to complex engineering challenges.

Now that we have developed multistable structures capable of achieving desired shapes, the next challenge is to determine the design parameters necessary to precisely achieve these shapes through inverse design. Inverse design is vital for crafting structures that meet specific functional and operational criteria, but this process faces considerable challenges. The main difficulty lies in the vast search space and the complex relationship between the design parameters and the resulting structural behaviors. This necessitates the development of sophisticated algorithms and modeling techniques to efficiently explore potential solutions and ensure the structures perform as intended in their respective applications. Herein, we present a solution that utilizes machine learning, assisted by mechanical observations, to address the complexities of inverse design of kirigami structures. By integrating data-driven algorithms with empirical insights from the physical behavior of structures, this approach significantly enhances our ability to predict and optimize design parameters, and experimentally manufacture the structure of the exact desired target shape. This brings together our study from design to manufacturing of multistable kirigami structures.

Though the structures developed thus far effectively serve our purpose, they deploy immediately upon release from their planar precursor. This prompts the question: can we create structures that allow for the indefinite storage of the planar precursor, deploying only when

necessary? Such a capability would significantly enhance the practicality and versatility of deployable structures, making them more suitable for applications requiring on-demand deployment. Moreover, the creation of deployable structures often involves complex and expensive processes, which can limit their accessibility and scalability. Addressing this, can we develop these structures in a simpler, more intuitive, and equipment-frugal manner? As a conclusion to this study, we present form-finding structures that can not only be deployed at will but can also be manufactured using simple, readily available tools at one's home, thus democratizing the technology for wider use and application.

This thesis thus explores the nexus of material science, mechanical engineering, and design theory, illustrating how deployable structures can bridge the gap between static planar manufacturing and dynamic 3D functionality. Through the integration of bistability, advanced computational tools for inverse design, and frugal manufacturing approaches, this work not only addresses fundamental scientific challenges but also paves the way for practical applications that could revolutionize multiple industries. The narrative woven through this research encapsulates the evolution from conceptual frameworks to tangible, impactful technologies, highlighting the profound potential of deployable structures to transform our interaction with the material world.

CHAPTER 2

Soft Kirigami Deployables

2.1 Background

Deployable structures have been explored for centuries, beginning as early as the 1700s when clockmakers first utilized bimaterial strips to engineer basic 1D to 2D transformations. These strips buckled under the influence of heat, transitioning into two-dimensional configurations due to temperature differentials between the layers. This early innovation marked a foundational step in the evolution of deployable structures, paving the way for more sophisticated developments.

As the field matured, researchers expanded the scope from simple 1D structures to intricate 3D configurations. This included the development which showcased advanced deployability suitable for structural applications.

The research focus eventually shifted toward transforming two-dimensional planes into complex three-dimensional forms. This progression has been supported by a variety of actuation methods including heat [18], swelling [19], [20], light [21], electromagnetism [22], chemical gradients [23], pneumatics [23], biological growth [24] and material anisotropy [25]. Each method was selected based on its specific benefits and the requirements of the intended application.

Among the diverse techniques adopted, the traditional Japanese arts of origami[26]–[31] and kirigami [26]–[28], [32]–[34]—folding and cutting paper—emerged as prominent methods in engineering. These techniques proved highly effective in shaping the structures to predesired shapes or switching between different shapes of the structure.

All the approaches studied have created methods of morphing flat sheets into predefined

three-dimensional shapes. However many techniques still result in creating piecewise rigid structures often requiring additional mechanical components for deployment. Research by our lab [14] was driven by the ambition to develop deployable structures capable of transitioning from a flat, 2D form into a predetermined 3D topology without the reliance on rigid parts. This innovative class of deployables was built upon foundational research that involved applying mechanical loads and boundary conditions on sheets. Simple manipulations like pulling a thin elastic sheet were sufficient to induce complex three-dimensional deformations through mechanisms such as wrinkling instabilities [35]. Past studies, such as those by Grason and others [36], demonstrated that imposing curvature on elastic sheets could initiate various structural instabilities [37] arising from geometric frustration—this occurs when the imposed constraints are incompatible with the natural configuration of the materials.

To creatively address and harness these instabilities, we employed strategic material removal inspired by kirigami [38], [39]. This approach not only relieved geometric frustration but also allowed precise control over the morphing process, enabling the transformation of the deployable into its desired three-dimensional form. Moreover, it provided a method to fine-tune the ultimate shape of the deployable directly from its planar state.

Our study marked a significant paradigm shift in deployable technology, moving from basic mechanical responses to complex design principles that embed the final three-dimensional structure's blueprint within its two-dimensional precursor. This fusion of design and functionality illustrated a synthesis of art, science, and engineering, expanding the potential of deployable structures to meet future challenges.

2.2 Methodology

The objective was to fabricate a 3D structure from a planar precursor, aiming for complete control over the final shape. As discussed earlier, fully flexible deployables have various benefits, such as increased flexibility in shape morphing and the absence of numerous rigid sub-components.

This was achieved by implementing a stress mismatch technique [14]. Specifically, a

stretched rubber sheet (called the substrate layer) was adhered to an unstretched sheet. This mismatch in stress across the composite forced it to buckle out of plane, transforming into a 3D shape. Based on intuition, initial attempts to create a hemispherical shape started with circular sheets subjected to radial pre-stretch. However, as Fig. 2.1(A) demonstrates, the result was not a hemisphere but an arbitrary 3D shape. Further experimentation, as shown in Fig. 2.1(A), indicated that this method could lead to various distinct shapes, underscoring the necessity for precise control over the final form.

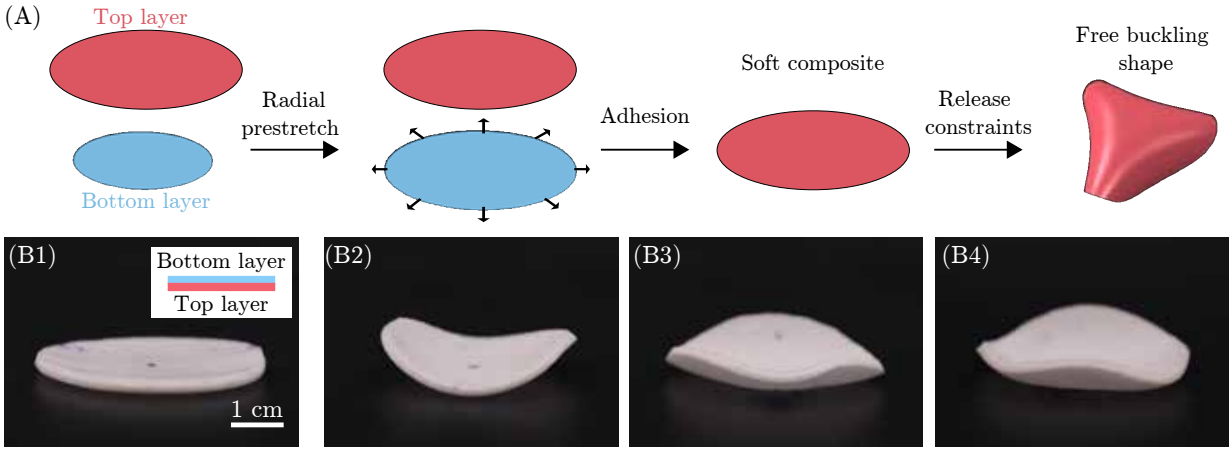

Figure 2.1: (A) Of two circular layers, the bottom layer is stretched and adhered to the unstretched top layer to obtain a soft composite. Upon releasing the constraints, the strain mismatch between the two layers induces symmetry breaking and the composite may assume a buckled shape (B) Arbitrary buckling shapes (experimental) of different prestretches [14]

To address this challenge, the solution involved the strategic relief of geometric frustrations at certain points. Herein the art of kirigami was implemented. Kirigami cuts were applied to the top, unstretched layer, as depicted in Fig. 2.2. A lotus kirigami design, determined heuristically, was utilized to achieve the specific hemispherical target shape. Thus, Zavodnik et al. [14] successfully took the first step towards creating a fully flexible 3D structure from a planar precursor, achieving a predetermined shape.

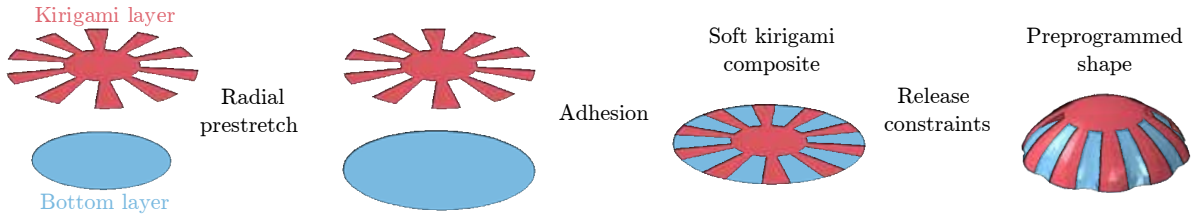

Figure 2.2: Replacing the top circular layer with a kirigami layer (layer with cuts) can lead to a preprogrammed shape via the same procedure as before. The shape is governed by the kirigami pattern. In this case, the goal was to obtain an axisymmetrical cap.[14]

2.3 Variation of design parameters

The research into soft kirigami deployables demonstrates that we can achieve precise control over the final 3D shape produced by the process. This control is primarily exerted through modifications to the kirigami design of the top layer, tailored to the requirements of the desired shape. Additionally, several design parameters influence the creation of these deployables, including the choice of materials, the overall size of the structure, and the degree of pre-stretch applied to the bottom or substrate layer. Fig. 2.3, based on simulations and experiments by Zavodnik et al., illustrates how variations in the pre-stretch of the bottom layer impact the final 3D shape. Increasing the pre-stretch from 5% to 25% not only alters the structure's height or curvature but also results in a non-axisymmetric structure from an axisymmetric precursor at certain levels of pre-stretch. It is crucial to recognize that the final 3D shape can be predetermined by carefully adjusting these initial design parameters. Our subsequent research further explores this concept.

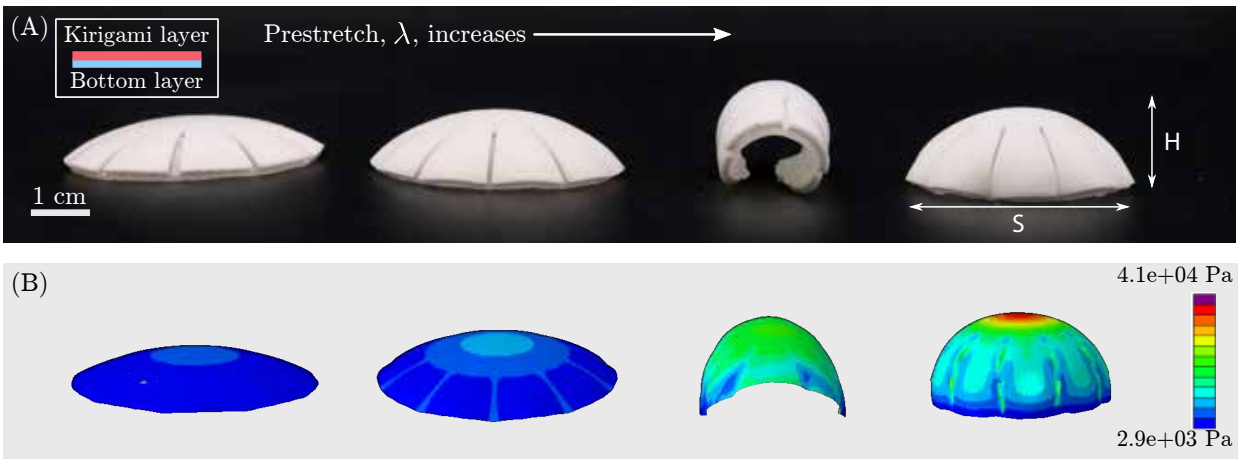

Figure 2.3: (A) Experimental images and (B) snapshots from finite element simulations at different values of prestretch: 1)$\lambda = 1.05$, 2) $\lambda = 1.15$, 3)$\lambda = 1.2$, and 4) $\lambda = 1.25$ to obtain the preprogrammed shapes [14]

2.4 Application to Wearables in Biomedicine

The advent of skin-wearable patches has transformed personal healthcare by utilizing non-invasive technology to gather essential health data and deliver medications effectively. [40]. Before this breakthrough, obtaining vital health metrics typically involved clinical visits with invasive and inconvenient testing that offered only intermittent data. Traditional methods of drug delivery, such as oral ingestion and injections, were hindered by inconsistent absorption rates, potential adverse effects, and lower patient adherence. Skin-wearable patches mitigate these drawbacks by providing ongoing, real-time monitoring of critical health indicators, including glucose levels, heart rate, and sweat composition, facilitating tailored health insights and more prompt interventions [41], [42].

Additionally, these patches have the potential for internal use within the body for targeted drug delivery. Presently, cancer treatment delivery is mainly through oral methods or systemic therapies like chemotherapy. However, in advanced cancer stages, these traditional administration routes may become inappropriate due to the patient's deteriorating health, coupled with the inefficiency of the medication reaching the tumor site directly. This has prompted a shift towards investigating novel drug delivery techniques, including the

development of tumor-targeting patches that could provide direct medication to cancer cells [43].

The engineering behind these patches is complex, aiming for compatibility with skin physiology, secure adhesion, and minimal irritation over long periods. Moreover, tailoring these patches for widespread use presents challenges, such as accommodating various body sizes and tumor shapes.

This brings us back to the concept of our fully flexible deployables designed to conform to any target shape, including the unique contours of a wearer's hand or specific internal anomalies. The use of initially planar precursors significantly simplifies the integration of electronic, mechanical, or biological subsystems for drug delivery onto the patches. This advancement could dramatically alter the landscape of soft wearable technologies and mark a significant milestone in biomedicine.

2.5 Drug Delivery Patches for Mice

In collaboration with NDSU, our project embarked on applying our deployable structures to develop preliminary skin-wearable patches for mice, aiming for a seamless fit that would remain secure despite the animal's movements.

For our experimental model, we chose a stuffed mouse specimen, specifically the HANSA Mouse Plush [44], to simulate the sizing and contours of a live mouse. The prototype patch consisted of a bimaterial strip. We started with a rectangular substrate, which we stretched to a specified length. Then, we added a rectangular kirigami strip atop the stretched substrate. It's important to note that the kirigami layer's length exceeded that of the original substrate strip, while its width was narrower. The kirigami strip's design was calculated based on a Poisson's ratio of 0.5, under the assumption that the material behaved as fully plastic. This configuration resulted in a band that snugly fit around the mouse's back.

We observed that bands subjected to very high pre-stretches tended to curl in on themselves, making them difficult to place on the mouse's back. Conversely, bands with very low

pre-stretches were too loose, leading to slippage. Similarly, bands made from very thick strips did not conform well to the mouse's back, while those from excessively thin strips applied more pressure than was ergonomically acceptable. Through heuristic testing, we identified optimal pre-stretch levels and dimensional specifications for the target mouse model. The precise measurements and pre-stretch values selected are detailed in Fig. 2.4(A).

We fitted this band on the HANSA plush mouse, and it conformed perfectly to the toy as shown Fig. 2.3(B). To simulate extreme movements, we vigorously threw the mouse around. Impressively, the band remained securely in place, attesting to its perfect fit on the mouse's body. This demonstration confirms the band's robustness and reliability under dynamic conditions.

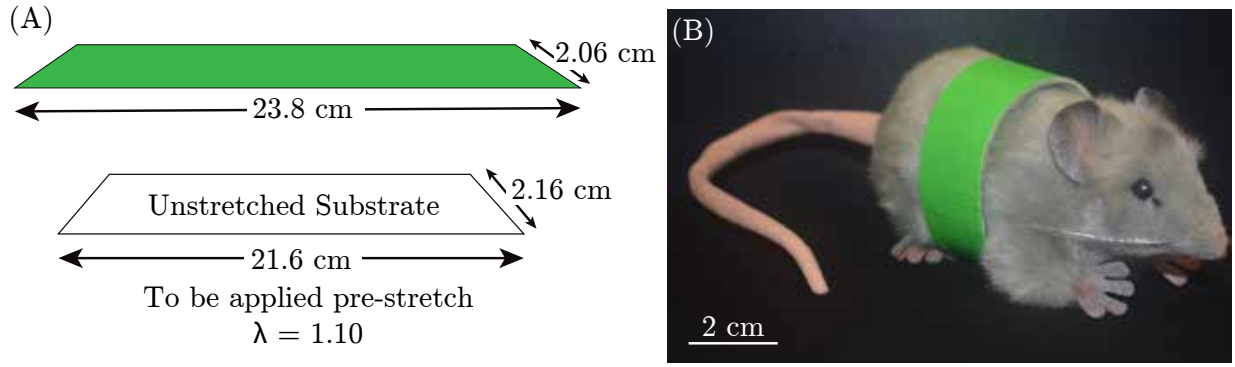

Figure 2.4: Overview of the medical band (A) Shape and dimensions of the kirigami and (unstretched) substrate layer for manufacturing the bands (B) The mouse plush wearing the band designed for it

2.6 Biocompatible Materials

Currently, to create these patches, we utilize VHB^{TM} tapes (Very High Bonding) from 3M^{TM}[45] due to their stretchability and adhesive nature Fig. 2.3(A). However, biomedical patches intended for wearable applications necessitate biocompatible materials. This requirement arises from their long-term contact with skin or potential internal use. Therefore, we have embarked on exploring biocompatible materials compatible with our bilayered patches.

Replacing the kirigami layer with a biocompatible material does not pose much of a chal-

lenge, as the primary requirement is a minimum stiffness. However, replacing the membrane material demands more consideration. We tested various biocompatible materials during this process. Popular materials like PLGA (Poly(lactic-co-glycolic acid)) [46] and CNF (Cellulose Nanofibers)[47] were considered but ultimately failed due to their brittleness, which led to breakdown before reaching 100% stretch. After multiple heuristic trials, Duraflex [48] was selected. Duraflex is a biocompatible elastomer that withstood up to 400–500% stretch, thus proving suitable for producing a medical kirigami patch as shown in Fig. 2.5(B).

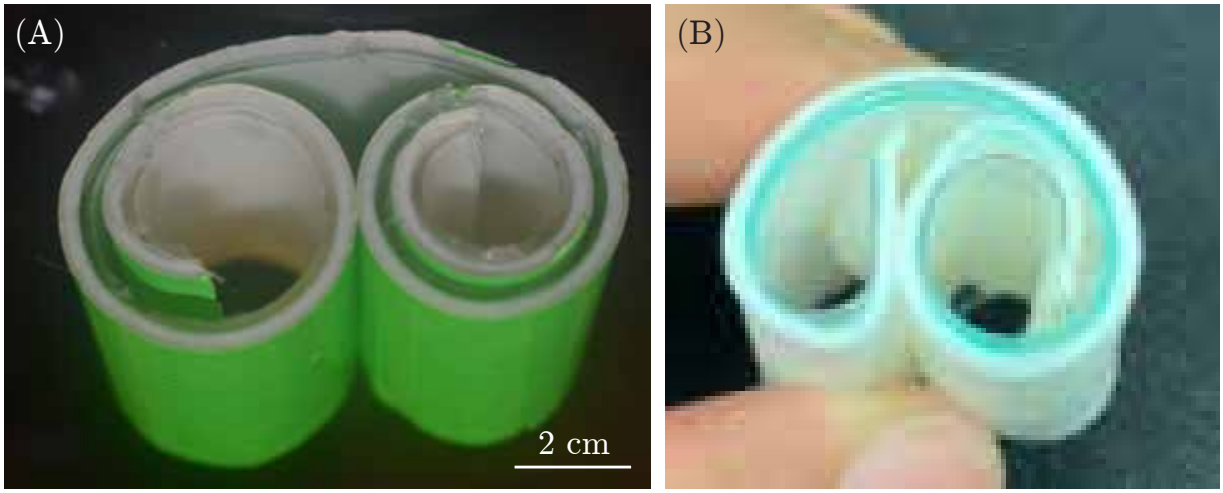

Figure 2.5: Medical patches made of different materials (A) VHB Substrate (B) Duraflex Substrate

2.7 Conclusion

In conclusion, the development of soft kirigami deployables showcases significant progress in the design of materials capable of morphing from two-dimensional precursors into intricate three-dimensional structures with precise control. This innovation is particularly promising for the field of medical wearables, where adaptability to complex anatomical forms is crucial. The application of kirigami techniques allows for the customization of wearable devices that can conform seamlessly to varied body contours, enhancing both the efficacy and comfort of medical treatments. As demonstrated in the research, these deployables are integral to the next wave of biocompatible wearables, offering potential advancements in non-invasive

monitoring and targeted drug delivery systems.

CHAPTER 3

Bistable Kirigami Deployables

3.1 Motivation for Bistability

In the evolving landscape of material science and robotics, the previous discussions have underscored the significance of structures that transition from 2D to 3D forms, highlighting their broad spectrum of applications. But the myriad of applications in today's world demands structures capable of multiple 3D configurations, akin to the adaptive nature of biological systems such as the Venus flytrap [49] or the dynamic locomotion of animal limbs [50]. The development of such structures, which can alternate between configurations, opens the door to enhanced flexibility in application scenarios ranging from adaptive architecture [51]–[53] to responsive wearables [54] and soft robotics [55]–[58].

The ability to switch between configurations, akin to the biological examples provided, is not just a novel feature but a requisite for the next generation of materials aimed at addressing the complex demands of today's technological advancements . The development of bistable or multistable structures, which can reside in multiple stable states and transition between them, marks a significant leap in material science [59], [60]. These structures can radically enhance the flexibility of applications, offering nuanced control mechanisms for devices that require precise actuation for functionality, such as the opening and closing of a gripping mechanism in robotics [61]–[64]. The transition between these stable states introduces a new dimension of functionality, enabling materials to adapt and respond to their environment dynamically [65], [66].

However, the creation of structures with multiple stable configurations still presents one complex challenge. It would be beneficial to not only fulfill the functional requirements, but

to also achieve a level of design flexibility that allows these structures to be custom-tailored to specific application needs. This adaptability is crucial for ensuring that the structures can integrate seamlessly into various environments, interact with objects of differing shapes and sizes, and perform functions with precision and efficiency.

Building upon the foundation of soft kirigami deployables [14], we present research that pushes the frontier by introducing structures that are not just morphable in shape but inherently bistable. These deployables, are engineered to be fully soft, ensuring a smooth transition between states without the complexity and limitations associated with rigid components. This adaptation of soft kirigami techniques further enables the fabrication of structures that can dynamically change their configuration in response to external stimuli, offering a smooth, reversible transformation between at least two stable states.

This innovative approach significantly widens the application spectrum for such 3D structures, making them suitable for a vast array of uses. For instance, in soft robotics, bistable kirigami structures can revolutionize robotic grippers, enabling them to mimic natural precision in holding and releasing objects through stable states, enhancing efficiency and functionality. This principle extends to wearable technology, where bistability can lead to garments that adjust their properties in response to environmental changes, providing tailored comfort. In the medical field, bistable devices can transform minimally invasive surgeries and targeted drug delivery by offering tools and implants that shift between functional modes with precision, optimizing treatment efficacy.

The essence of this research lies in its ability to blend artistic creativity with scientific innovation, resulting in the development of soft kirigami deployables that are not only functional but also versatile and adaptable. By creating such multistable deployable structures, this study further enables us to take great strides in creating tunable but highly functional robotics and wearables in today's' world.

3.2 Design concept

By applying a pre-stretch to one layer of a bilayered composite, we facilitated an out-of-plane deformation that transformed a planar precursor into a 3D shape. This transformation was further guided by designing the unstretched layer with kirigami cuts, allowing us to predetermine the shape of the final 3D object. However, to achieve a structure with more than one stable 3D state, we introduce another identical kirigami layer, attaching it to the opposite side of the substrate while maintaining complete geometric symmetry about the substrate layer. Consequently, the structure becomes equally likely to deform toward either kirigami layer, resulting in two stable configurations of the kirigami deployable Fig. 3.1.

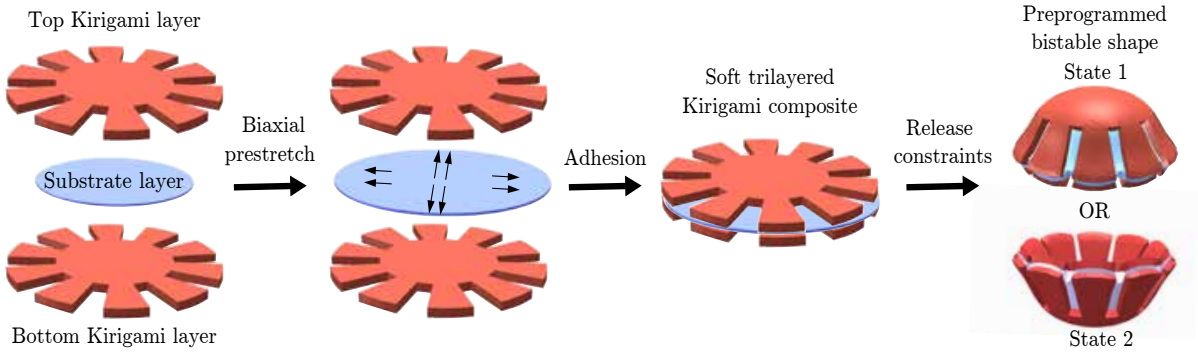

Figure 3.1: Overview of the bistable soft structure design. The combination of two kirigami layers and strain mismatch creates 3D soft structures that are fully soft and bistable [67]

Our experimental and analytical explorations of this design demonstrate the ability to switch at will between these two configurations, thus creating a bistable soft structure. Moreover, subsequent sections reveal that these structures are not limited to two configurations; they can exhibit multiple stable states if the design parameters are conducive to such outcomes. In pursuit of creating multistable structures, we thus, ingeniously extended the bilayered kirigami deployables [14] to trilayered deployables, thereby broadening their range of applications. Multiple demonstrations of these versatile structures have been showcased to emphasize their potential.

3.3 Experimental Manufacturing

While the original research [14] utilized a specially designed setup for applying radial stretch, this study introduces a simpler configuration that enables the manufacturing of a broader spectrum of shapes. Initially, we substituted the radial stretch with a bi-axial stretch. This adjustment not only fulfilled the original purpose for axisymmetric shapes but also facilitated the creation of non-axisymmetric structures. Moreover, the new setup accommodated larger structure sizes, which proves advantageous for subsequent phases of deployable research.

As depicted in Fig. 3.2(A1,B1), our arrangement comprised of four linear translation stages (250 mm travel, Thorlabs, Inc.) positioned perpendicularly to each other at specified distances on an optical breadboard. This configuration allowed us to adjust the distances between the stages as needed. For the substrate, we employed Very High Bonding (VHB$^{\text{TM}}$) hyper-elastic rubber sheets by 3M$^{\text{TM}}$, available in various thicknesses and stiffnesses tailored to different applications. The bilayered structures [14] utilized two specific types of VHB$^{\text{TM}}$ sheets for the bilayered kirigami composite experiments: the Clear VHB$^{\text{TM}}$ for the substrate and the White VHB$^{\text{TM}}$ for the top layer. For the trilayer structures, we used the Gray VHB$^{\text{TM}}$ to slightly modify the stiffness to compensate for the additional layer in the composite. The material properties of the layers have been modelled in the next section.

We placed an arbitrary sized square piece of substrate on the four linear stages as shown in Fig. 3.2(A2,B2) and marked three points in the central section: the center point and a point along each axis marked by the two sets of stages, illustrated by the redpoints in Fig. 3.2(A1,A2). We measured the lengths of the two segments formed, which served as our original reference dimensions for calculating the pre-stretch of this layer. Care was taken to ensure the stretching is controlled, keeping the central marked point centered throughout the process. We then incrementally pulled on the stages to apply a bi-axial stretch to the substrate, measuring the final lengths of the segments and continuing the stretching process until achieving the desired pre-stretch level.

The kirigami layer was crafted from the Gray VHB$^{\text{TM}}$ sheet, initially designed in software such as SolidWorks or AutoCAD and then cut using a laser cutter. This kirigami layer

was then carefully attached on top at the center of the stretched substrate, utilizing the adhesive properties of the VHB^{TM} tapes. An identical piece is attached to the bottom of the substrate Fig. 3.2(A3,B3). Care is taken to align the two layers to maintain the required top-down symmetry. To mitigate any remaining stickiness and prevent it from hindering the deformation, chalk powder was applied to the composite. Finally, as shown in Fig. 3.2(A4,B4), the excess substrate is cut away according to the desired resulting shape using a pair of scissors. This action relieved the stress in the substrate layer, allowing the composite to buckle and assume its predetermined 3D shape Fig. 3.3(A). We trim away any excess substrate further before we let the shape rest until it stabilizes.

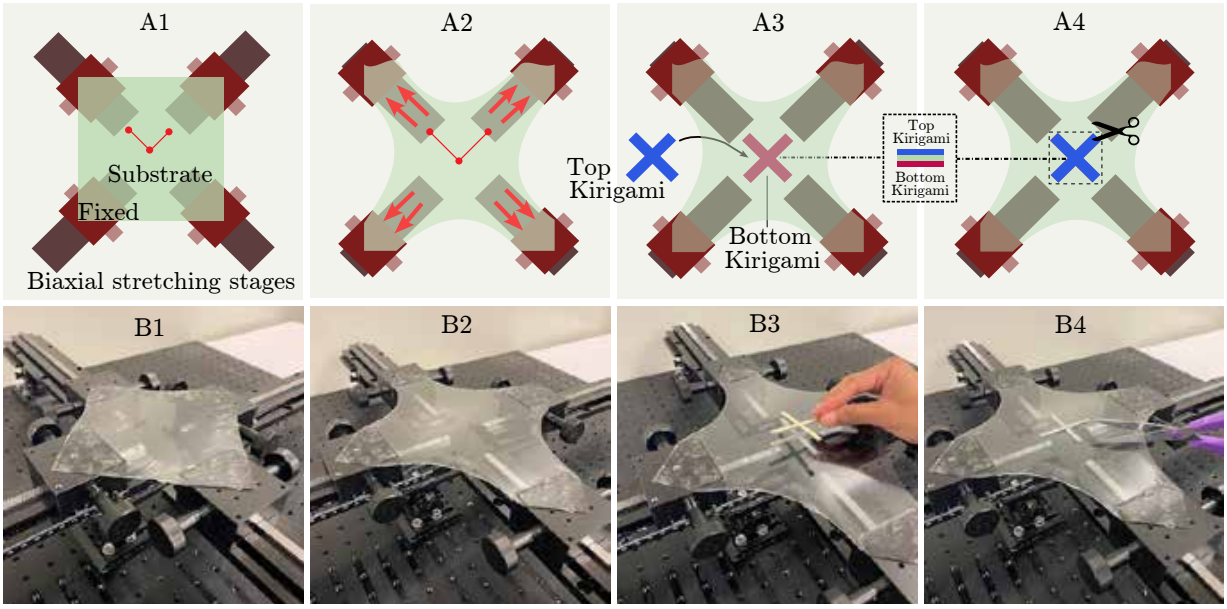

Figure 3.2: Experimental setup. (A1-A4) CAD model of the experimental setup (B1) Schematic representation of the system consist of two-knob stages on 250 mm tracks with reference segments in red (B2) Snapshot of the system when the substrate layer is stretched visible by the red stretched segments (B3) Attach one kirigami layer below the substrate layer, and the other one on top of the substrate layer (B4) Release the pre-stretch by cutting along the outline of the circular substrate. [67]

In our study, we opted for cross-shaped kirigami and square-shaped substrate layers for our experiments. The rationale behind selecting these specific shapes is based on heuristic considerations. With the correct pre-stretch value, denoted as (λ) these layer designs yield a 3D structure resembling a pyramid, as shown in Figure. The original length of the

2D cross shape (L), and the height of the emerged 3D pyramid (H), are detailed in the inset of Fig. 3.3(A). The immediate structure configuration post-removal of the boundary conditions is referred to as the "positive" configuration, whereas its inversion is termed the "negative" configuration. A settling period was allowed for both configurations before any measurements. As pre-stretch is increased, the pyramid's normalized height (H/L) escalates nonlinearly.For a composite of this size, with L=60 mm, the normalized heights of both configurations were comparable, as evidenced in Fig. 3.3(B).

It should be noted that the experimental approach imposes certain limitations on the choice of materials for fabricating these structures. Specifically, the substrate layer needs to be highly stretchable, while all layers must be amenable to cutting as per experimental needs. Consequently, brittle or highly rigid materials are unsuitable for the substrate layer due to the high degree of stretch required. However, the kirigami layer is less constrained, needing only to be precisely cuttable. Advances in laser cutting technology are expanding the range of feasible materials for this technique, though challenges remain in terms of precision and the manageability of thicker materials. These considerations regarding material properties are critical in the design phase of these structures.

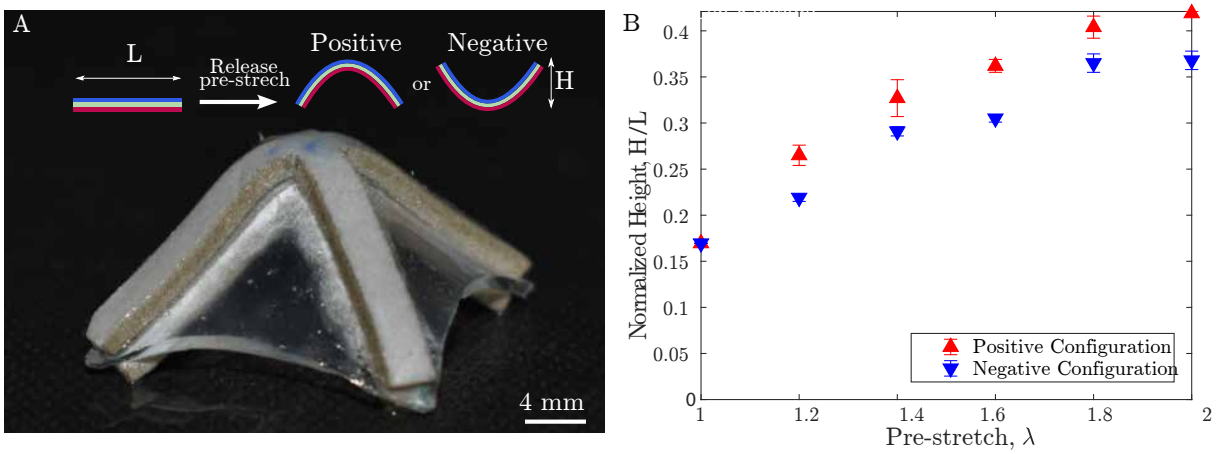

Figure 3.3: (A) Side view of the trilayer pyramid 2D precursor, and the free buckling shape of the trilayer pyramid 3D structure (B) Preliminary variation of normalized height as a function of the pre-stretch ($L = 60$ mm) [67]

3.4 Material Modelling

As discussed, material modeling presented a significant challenge due to the VHB^{TM} tapes not being composed of linearly elastic materials. Therefore, it was crucial to thoroughly analyze the mechanical properties of each material before proceeding with the numerical and analytical analyses of the structures.

To address this, we adopted a tensile testing approach to ascertain the stress-strain profiles of each material involved. This was conducted using the ASTM D412 dogbone sample [68], a standard predominantly utilized for vulcanized rubber and thermoplastic elastomers, thus making it an apt choice for our testing needs. The specimens were mounted on an Instron machine, subjected to a displacement rate of 0.01mm/s, while the force was monitored using a 2kN load cell. The initial dimensions of the specimen facilitated the computation of engineering stress and strain values Fig. 3.4.

Upon obtaining the stress-strain data, we explored multiple non-linear hyperelastic material models to identify the one that best matched our materials. The stress (σ) and stretch (λ) relationship for all three materials most accurately conformed to the Mooney-Rivlin model [69], as shown in the following equation:

$$\sigma = 2C_1\left(\lambda^2 - \frac{1}{\lambda^4}\right) - 2C_2\left(\frac{1}{\lambda^2} - \lambda^4\right) \tag{3.1}$$

Here C_1 and C_2 are the material constants involved. Additionally, the relationship between stretch (λ) and strain (ϵ) is described by:

$$\lambda = \epsilon + 1 \tag{3.2}$$

Applying the Mooney-Rivlin model to fit the engineering stress-strain curves allowed us to derive the necessary Mooney-Rivlin material parameters for each of the three materials examined. These parameters are summarized in Table 3.1 and were subsequently utilized in the numerical simulations to accurately represent the material properties of the layers

involved. Notably, the White VHB^{TM} was found to be stiffer than the Gray VHB^{TM}, aligning with our expectations. We plan to continue employing the White VHB^{TM} for bilayered structures in the forthcoming chapter, where this aspect will be explored in greater detail.

Parameter	Value	Unit
Material Constant C_1^s	22.1	KPa
Material Constant C_2^s	1.7	KPa
Thickness t^s	1.1	mm
Material Constant $C_1^k g$	17.9	KPa
Material Constant $C_2^k g$	84.5	KPa
Thickness $t^k g$	1.6	mm
Material Constant $C_1^k w$	185.8	KPa
Material Constant $C_1^k w$	1.4	KPa
Thickness $t^k w$	1.4	mm

Table 3.1: The Mooney Rivlin material parameters for the three different materials used [67] [67]

3.5 Numerical Simulations

The nonlinear large deformation of the trilayer structures was analyzed using ABAQUS software. In contrast to earlier methods [14] that employed planar shell simulations for kirigami deployables, the incorporation of an additional layer necessitated adopting 3D simulations to more comprehensively understand the structures' out-of-plane deformations.

To facilitate the execution of the ABAQUS simulation, a MATLAB script was developed. This script required inputs such as geometric properties, material characteristics, the applied pre-stretch, and the specific kirigami design to be analyzed. Utilizing MATLAB's capabilities for geometric meshing, a planar triangular mesh was created for the kirigami and substrate layers Fig. 3.6(A). This initial 2D mesh was subsequently translated into a 3D mesh within ABAQUS, employing Solid (C3D6) prismatic elements Fig. 3.6(B). This conversion process ensured that elements at the juncture of different layers shared nodes, thereby simulating the continuity within each material section or the adherence between various sections of the composite. To accurately model the out-of-plane deformation, each material section was di-

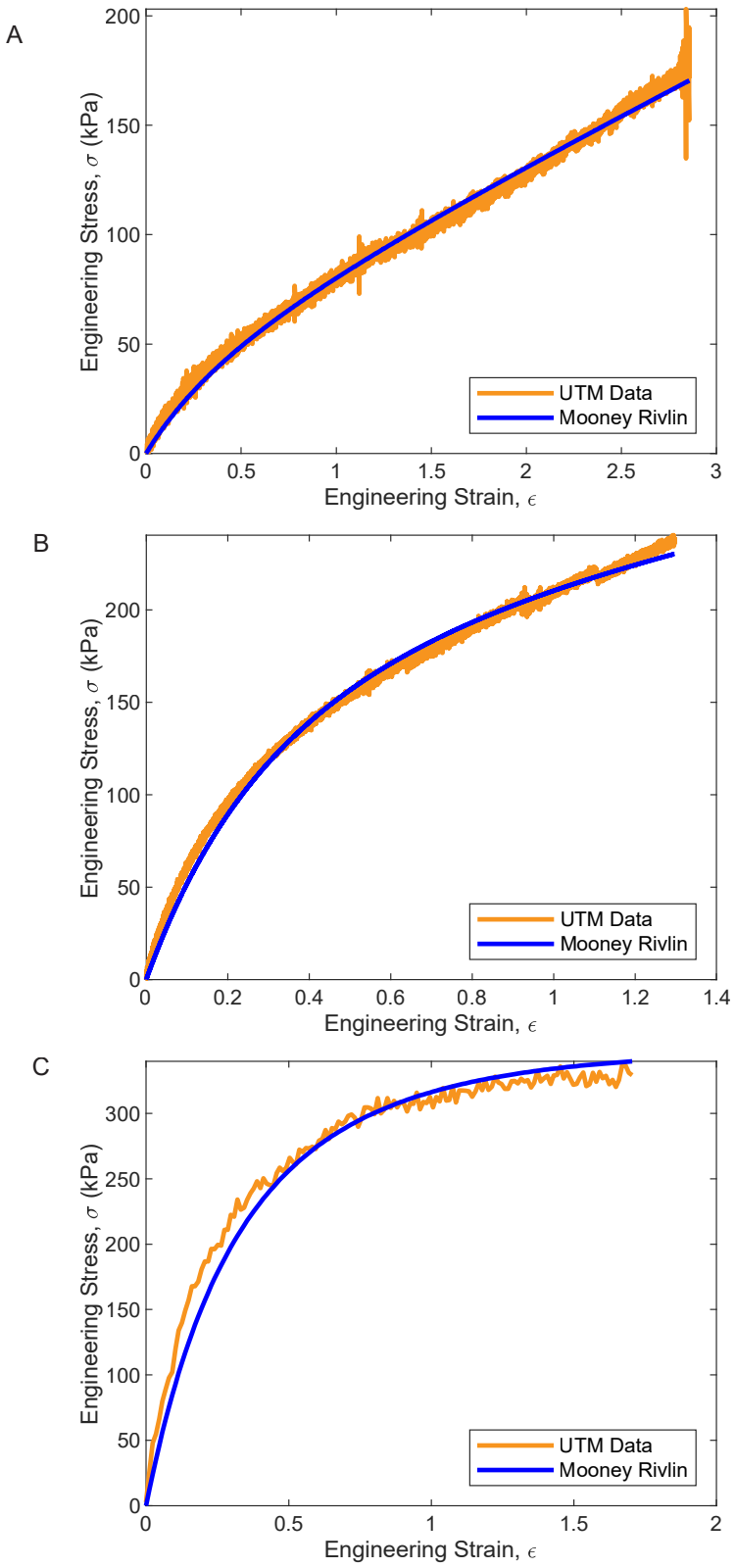

Figure 3.4: Engineering stress-strain curves from the UTM Tensile testing data with the Mooney-Rivlin curve fit for (A) Substrate (B) Gray Kirigami (C) White Kirigami.

vided into multiple sub-layers Fig. 3.6(B(ii)). These sub-layers each consisted of 4521 nodes, with the substrate and kirigami layers incorporating 2198 and 6046 elements, respectively. A series of central nodes across all substrate sub-layers (located at coordinates (0,0)) were assigned a fixed boundary condition for the duration of the simulation.

The simulation defined material properties for each section using the Mooney Rivlin model. With material constants (C_1, C_2) and the initial pre-stretch applied to the substrate layer, ABAQUS was able to calculate a predefined stress according to the previously mentioned equation. This calculated stress was then applied to the substrate layer as an initial condition for the simulation. In addition, a minimal, nonzero distributed force was applied to the structure to encourage buckling into one of two possible configurations, identified as the "positive" state. Due to the inherent geometric symmetry of the structure, identifying one configuration in the simulation implied the potential existence of its opposite configuration.

The simulation process was designed to be geometrically nonlinear and quasi-static, with the simulation's duration adjusted based on heuristic methods to allow the structure sufficient time to stabilize in its deformed state. Typically, a single numerical simulation would require between 1 to 3 minutes of real-time on a desktop computer equipped with a Ryzen 2950wx CPU @ 2.4 GHz. The simulation's outcome, stored in the output file (.odb), successfully depicted the expected transition from 2D to 3D deformation Fig. 3.6(C).

To examine the impact of different pre-stretch values on the final shape, the pyramid structure was simulated across a range of pre-stretch values. The nodal position information extracted from each output file facilitated the calculation of the maximum height (H) for the structures by considering the nodes with the highest and lowest z-coordinate values. A comprehensive exploration of this parametric variation is planned for discussion in an upcoming section dedicated to parametric variation.

This simulation framework was also employed to examine an alternative configuration to the one initially obtained. This examination involved an actuation step within the existing simulation to push the 3D pyramid structure into the opposite configuration. The process entailed two force application steps: firstly, extending the pyramid's legs outward

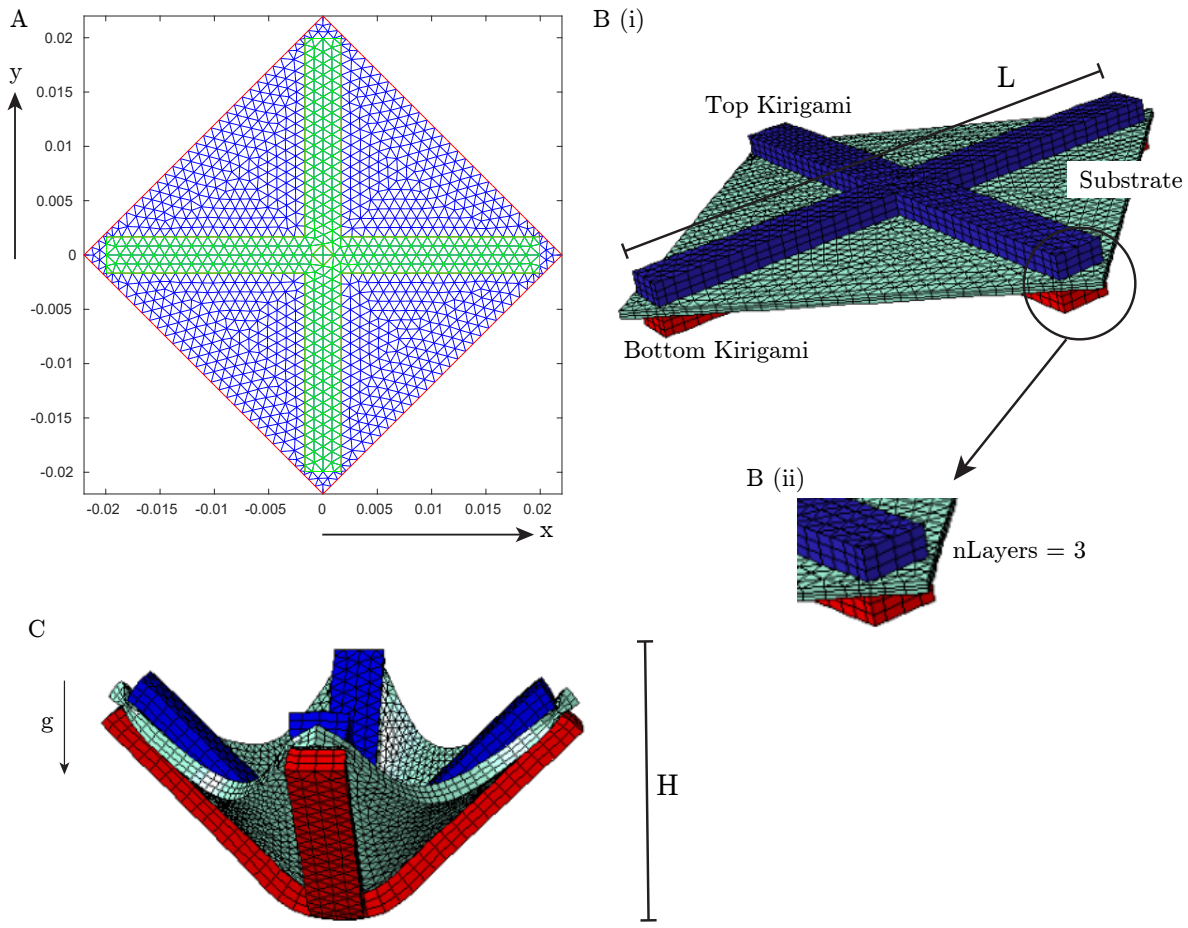

Figure 3.5: ABAQUS numerical simulations (A) 2D Mesh in MATLAB (B) (i) Undeformed trilayer structure showing the three main layers of the composite (ii) A close-up view of the multiple sublayers in the structure (C) Deformed configuration [67]

to "open" the structure, followed by pushing the legs vertically downwards towards the alternate configuration. Once the force application concluded, the structure was allowed to stabilize, revealing insights into the "negative" configuration and illuminating the multiple stable modes a structure could adopt, with further details provided in subsequent sections on bistability.

In conclusion, our simulations for the bistable structures involved a detailed analysis focusing on the speed and accuracy of the finite element framework. In our simulations, we adjusted the maximum size of mesh elements according to a shape-defining parameter, specifically half the length (L/2) of the current shapes . Following this, we determined the minimum size of the mesh elements to be half that of the maximum size. The out-of-plane

dimension of the mesh elements was defined by the count of sub-layers (*nLayers*) within the thickness of each layer in the tri-layered composite structure.

Our mesh convergence investigation was conducted in two primary phases: first, we examined the impact of an increased count of elements starting from the base 2D mesh; second, we looked into the effects of augmenting *nLayers*, which is the count of elements within the thickness of each composite layer. Our analysis revealed that adjustments to the mesh's complexity had minimal influence on the simulation's output, particularly in terms of the final structure's height Fig. 3.6(A,B). These findings suggest that even with variations in mesh complexity, the simulation outcomes remained consistent.

Furthermore, we evaluated how the size of the mesh affected the overall computational time required for the simulations. Our observations Fig. 3.6(C,D) indicated a significant increase in simulation time when the element count exceeded 2500, especially as we expanded the number of *nLayers* beyond three. Thus, our mesh study indicates that while it is feasible to simplify the mesh to substantially reduce computational demand, such simplification does not detract from the simulation's output accuracy. This balance allowed us to optimize computational resources without compromising the quality of our simulation results outcomes.

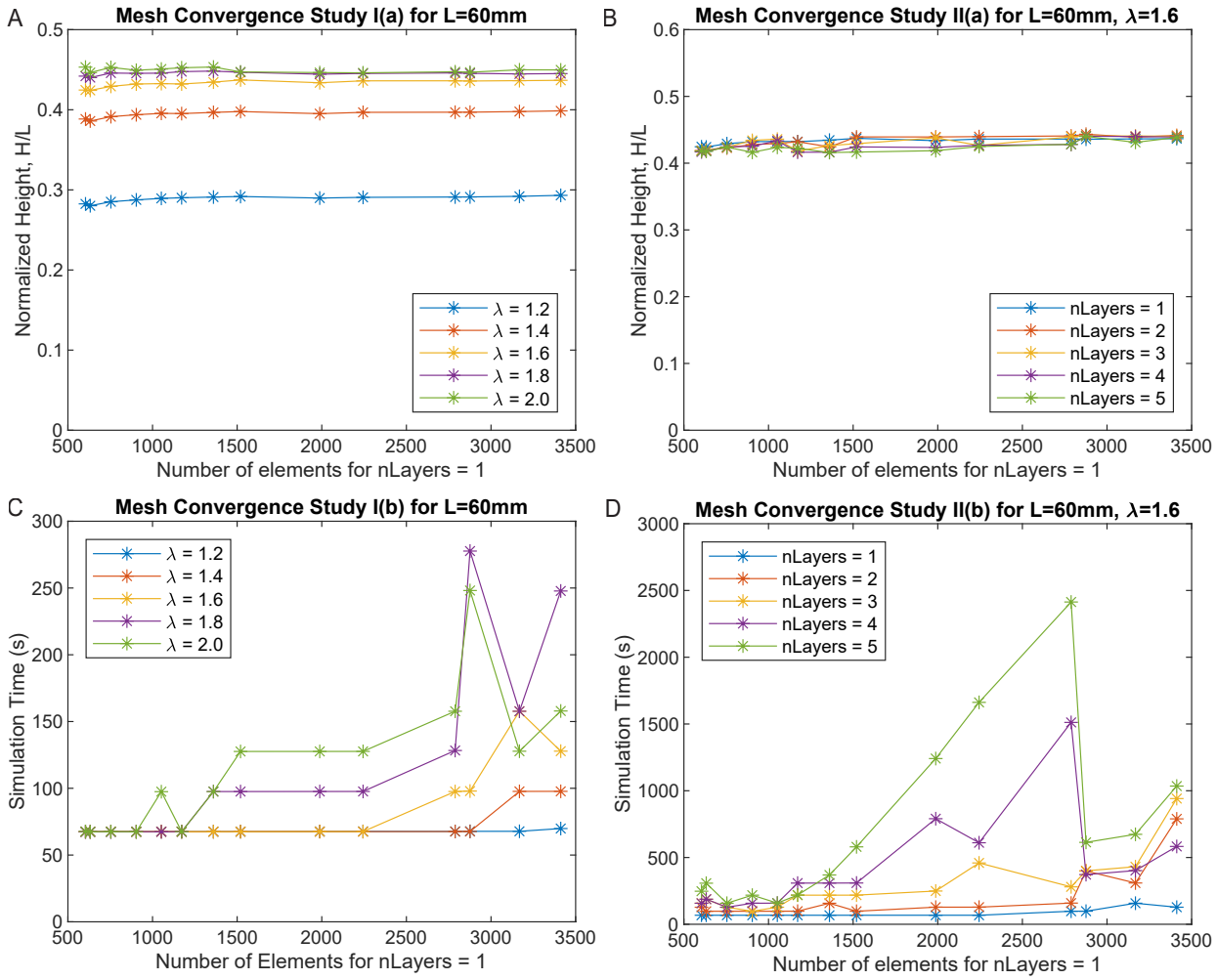

Figure 3.6: (A-B) Effect of the mesh on final height output. (C-D) Effect of the mesh on simulation time. (A)(C) Varying mesh element size for L=60mm. (B)(D) Varying number of nodes along the thickness of each composite layer for L=60mm, $\lambda = 1.6$ [67]

3.6 Analytical Formulation

The thicknesses of the substrate and kirigami layers are denoted as t_s and t_k respectively, all properties given in Table 3.1. It is assumed that following the phenomenon of free buckling, the initial stretching energy of the substrate layer is transformed into the bending energy of the whole composite structure. This transformation is energetically advantageous, as bending energy requires less energy than compression for thin shells, which is a critical consideration in the design of flexible structures [70]

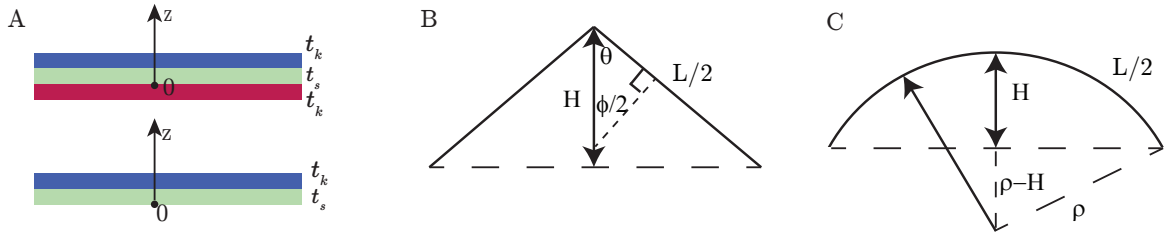

Figure 3.7: A) Cross-sectional view of the trilayer and bilayer composite structure (B) Sketch of the side view for a pyramid with height H. (C) Sketch of the side view for a spherical cap with height H [67]

Given the hyperelastic nature of the materials used, the stretching-induced energy E_s is calculated using the equation:

$$E_s = C_1 \left(2\lambda^2 + \frac{1}{\lambda^4} - 3\right) + C_2 \left(\lambda^4 + \frac{2}{\lambda^2} - 3\right) A t_s \tag{3.3}$$

where $\lambda = \frac{L_f}{L} = 1 + \epsilon$ represents the pre-stretch, which is the ratio of the stretched substrate size L_f over the unstretched size L. The area A of the unstretched substrate, assuming a Poisson's ratio of 0.5, for a square-like substrate, is calculated as:

$$A = \left(\frac{L}{\sqrt{2\lambda}}\right)^2 \tag{3.4}$$

Using linear material approximation, the stretching-induced energy for the substrate layer can be simplified to:

$$E_s = \frac{1}{2} A C_s \epsilon^2 \tag{3.5}$$

where $C_s = \frac{E_s t_s}{1-\nu_s^2}$, E_s and ν are the Young's modulus and Poisson's ratio of the substrate layer, respectively.

We further assume a small strain criterion to calculate the bending energy as follows:

$$E_b \approx \frac{1}{2} A D_{eq} \kappa^2 \tag{3.6}$$

where D_{eq} is the equivalent bending stiffness.

The equivalent bending stiffness of these composite structures is calculated based on the

mechanical properties and geometric configuration of the layers comprising the structure equivalent to that of composite beams.

For the trilayer structures Fig. 3.7(A(i)), the equivalent bending stiffness D_{tri} is derived by considering both the mechanical contributions of the kirigami and substrate layers (E, ν), as well as their placement (moment of inertia of each part about the composite's neutral axis, which is at the geometric center line):

$$D_{\text{tri}} = n\frac{2E_k\left[\frac{t_k^3}{12} + t_k\left(\frac{t_k}{2} + \frac{t_s}{2}\right)^2\right] + E_s\left[\frac{t_s^3}{12}\right]}{1-\nu^2} + (1-n)\frac{E_s\frac{t_s^3}{12}}{1-\nu^2} \tag{3.7}$$

where n is the fraction of the area covered by the kirigami layer, t_s and t_k are the thicknesses of the substrate and kirigami layers, respectively, and E_s and E_k represent the Young's modulus of the substrate and kirigami layers. The term $(1-\nu^2)$ in the denominator corrects for the Poisson effect.

For bilayer structures Fig. 3.7(A(ii)), the calculation of the equivalent bending stiffness D_{bi} also requires consideration of the neutral axis position $\bar{z}$, which shifts based on the relative stiffness and thickness of the layers:

$$\bar{z} = \frac{t_k\left(\frac{t_k}{2} + t_s\right) + \left(\frac{E_s}{E_k}\right)t_s\left(\frac{t_s}{2}\right)}{t_k + \left(\frac{E_s}{E_k}\right)t_s} \tag{3.8}$$

Utilizing $\bar{z}$, the bending stiffness for bilayer configurations is given by:

$$D_{\text{bi}} = n\frac{E_k\left[\frac{t_k^3}{12} + t_k\left(\frac{t_k}{2} + t_s - \bar{z}\right)^2\right] + E_s\left[\frac{t_s^3}{12} + t_s\left(\frac{t_s}{2} - \bar{z}\right)^2\right]}{1-\nu^2} + (1-n)\frac{E_s\frac{t_s^3}{12}}{1-\nu^2} \tag{3.9}$$

From the observation of the deformed 3D shapes, we further assume that the deformed shape is close to a pyramid shape, with the side view sketched in Fig. 3.7(B) For the pyramid-like shape, the curvature κ is related by the angle ϕ, the half-length of the cross shape $L/2$,

and the height of the pyramid H via the equations:

$$\kappa = \frac{4}{L}\tan\left(\frac{\phi}{2}\right) \tag{3.10}$$

$$H = \frac{L}{2}\sin\left(\frac{\phi}{2}\right) \tag{3.11}$$

Combining these equations provides a pure geometric relationship:

$$\frac{H}{L} = \frac{1}{2}\sin\left(\frac{\phi}{2}\right) = \frac{1}{2}\sin\left(\arctan\frac{\kappa L}{4}\right) \tag{3.12}$$

Since the $\arctan\left(\frac{\kappa L}{4}\right)$ function is bounded between 0 and $\frac{\pi}{2}$, the normalized height H/L is bounded between 0 and 0.5. Looking at it from a physics point-of-view, a perfect fold would yield $H/L = 0.5$. This relationship explains why in both simulations and experiments, the normalized heights plateau at very large amounts of pre-stretches, as depicted in Figure 4.

By balancing the stretching-induced energy in Eq. 3.5 and the bending energy in Eq. 3.6, the curvature κ can be calculated as:

$$\kappa = \pm\sqrt{\frac{2E_s}{AD_{eq}}} \approx \pm\sqrt{\frac{C_s}{D_{eq}}}\frac{\epsilon}{1+\epsilon} \tag{3.13}$$

This suggests that the system is bistable, capable of maintaining both positive and negative configurations.

Hence, H/L can be analytically estimated from the external pre-stretch as:

$$\frac{H}{L} = \pm\frac{1}{2}\sin\left(\arctan\sqrt{\frac{C_s}{D_{eq}}}\frac{\epsilon}{1+\epsilon}\frac{L}{4}\right) \tag{3.14}$$

For 3D shapes close to spherical caps, as shown in Fig. 3.7(C), the relationship between normalized height and curvature can even be further simplified as follows:

$$\frac{H}{L} = \frac{\kappa L}{8} \tag{3.15}$$

This arises from the fact that the curvature of a spherical cap (κ) is constant. Hence, the length of the entire curve (L) can be computed as:

$$(L/2)^2 = \rho^2 - (\rho - H)^2 + H^2 \tag{3.16}$$

where ρ is the radius of the hemisphere, which is related to the curvature κ via $\kappa = 1/\rho$.

To summarize, we have made multiple simplifications in deriving this analytical model. Firstly, we have assumed that all stretching energy gets converted to bending energy. Secondly, we have employed a linear approximation of a highly non-linear material model. Finally, we have employed multiple small deflections assumptions through the derivation. However, as we show later, these simplifications still produce a reasonable analytical formulation which greatly agrees with the experimental and numerical data.

3.7 Parametric Variation

In this study, we investigate the influence of size and pre-stretch on the final 3D shape of pyramid structures. The overall length of the kirigami (L) and the thickness of the substrate (t_s) serve as the key parameters defining the size of the planar precursor, while the degree of pre-stretch (λ) is examined as another critical variable in our analysis.

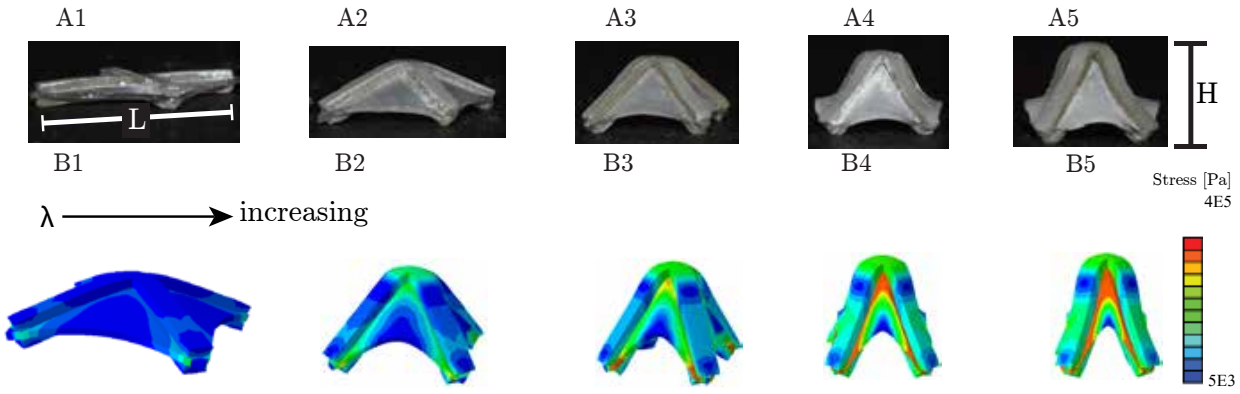

Figure 3.8: (A) Comparison of the free-buckling shapes in (A1-A4) simulation and (B1-B4) experiment for the cross-shaped kirigami composite structure (L=40 mm) at different amount of pre-stretch $\lambda = 1.2, 1.4, 1.6, 1.8, 2.0$. The colorbars correspond to the distribution of stress in the deformed trilayer structure [67]

Our approach begins by holding the size of the structures constant and systematically varying the pre-stretch, as depicted in Fig. 3.8. It is observed that the height of the structure escalates with an increase in pre-stretch Fig. 3.9(A-C) . This trend is anticipated, as the strain energy within the structures also rises with increasing pre-stretch Fig. 3.9(D), thereby enhancing the bending energy and resulting in a taller buckled structure. Additionally, we identify a buckling threshold beneath which no out-of-plane deformation occurs. Beyond a specific pre-stretch level, the height of the structure reaches a plateau, constrained by the dimensions of the 2D precursor. Despite the simplifications inherent in the analytical model, the experiments, simulations, and analytical predictions all display a consistent trend.

Further analysis involves altering the size of the 2D precursor by modifying the ratio (L/t_s). This adjustment reveals similar patterns in the relationship between height and pre-stretch, as evidenced in the figures. Interestingly, at a given pre-stretch, the normalized height of the structure increases with size. A corresponding increase in strain energy with size is also noted. Notably, a dip in the height value is observed at a ratio of L/t_s=80 Fig. 3.9(C) with an increase in pre-stretch. This anomaly becomes clearer in discussions related to additional stable buckling modes that emerge in larger structures, as detailed in a subsequent section.

3.8 Switching Force

The force required to switch between the two configurations of the trilayer bistable structures was analyzed through a methodical approach. A force indentation testing was performed to compute the force variation during the switching process. Positioned on a specially designed platform with a center hole, this setup allowed the structures to transition between their two stable states under controlled conditions. The measurement of force-displacement curves was facilitated by attaching a rigid indenter to a Mechanical Test System (MultiTest, Mecmesin) Fig. 3.10(A), operating under displacement control. This precise setup enabled the capture of the force variation with the switching, as is portrayed in Fig. 3.10(B). Each parameter set underwent repeated testing to ensure the reliability of the data, with the standard deviation

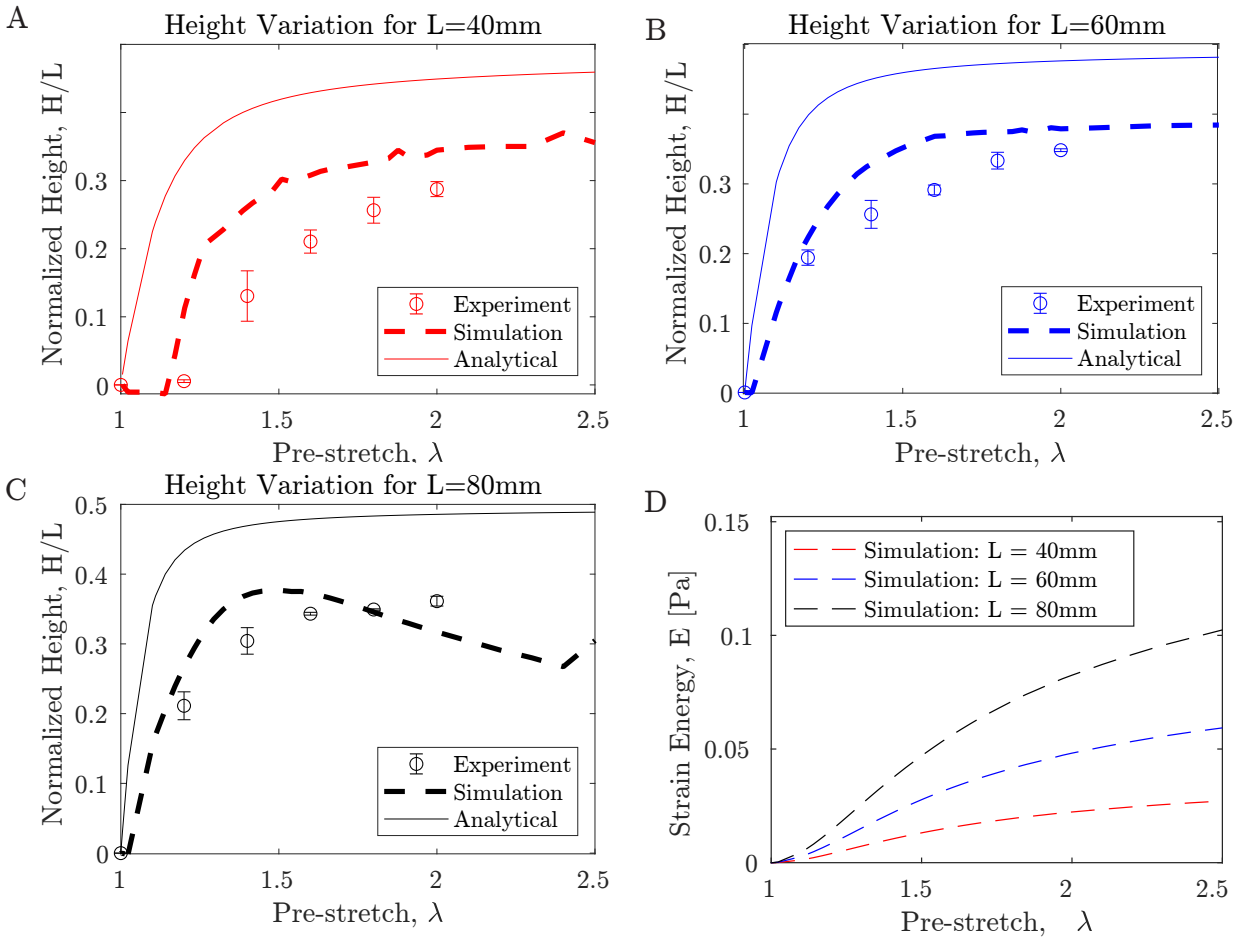

Figure 3.9: (A-C) The variation of the normalized height of the free-buckling shape as a function of the pre-stretch. Three examples showing different length/thickness ratio with diameter/width ratio fixed. (A) $\frac{L}{t_s} = 40$. (B) $\frac{L}{t_s} = 60$. (C) $\frac{L}{t_s} = 80$. (D) Variation of the energy landscape at different pre-stretch. Below a certain threshold, the composite structure hardly buckles [67]

calculated for each to quantify variability and consistency.

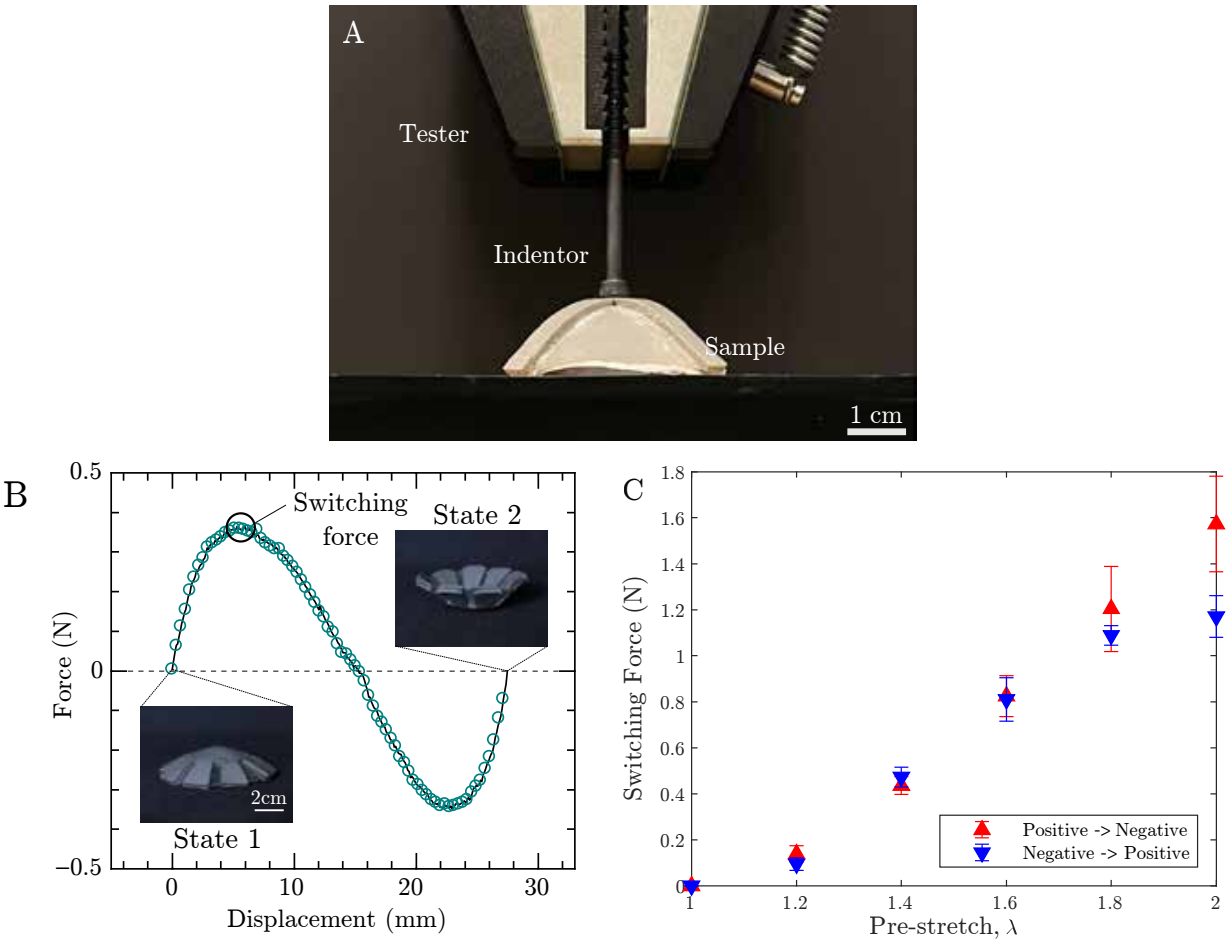

Figure 3.10: (A) Experimental setup for measuring the switching force during indentation (B) To demonstrate its bistability, the force-displacement curve of the trilayer soft structure was obtained experimentally, indicating that the structure can switch from one stable configuration to the other. The force required to change the state is defined as the switching force. (C) Variation of switching force required to switch between the two configurations (L = 60mm) [67]

The force-displacement curves obtained from this meticulous experimental process gave us more insight into the bistability of the trilayer soft structures. These curves are crucial for understanding the mechanical properties of the structures, particularly the specific force needed to induce a state change, labeled the switching force. We see that the switching force grows nonlinearly as the pre-stretch increases. This force ranges from about 0.1 N to 1.8 N (Fig. 3.10(C)) for the pyramid structures studied in this research.

3.9 Reversibility

To assess the long-term stability and reversibility of trilayer bistable structures, we embarked on a rigorous experimental process with a specimen whose properties are detailed later (Table 3.2). This process began with the precise measurement of the structure's height in both its positive and negative configurations, setting a baseline for subsequent evaluations. The experimental protocol involved performing cyclic tests where the structure was transitioned from its positive to negative state and back to positive, defining a complete cycle. After every set of 50 cycles, we meticulously measured the heights in both configurations, diligently documenting any changes to assess the structures' mechanical resilience and dimensional stability over time.

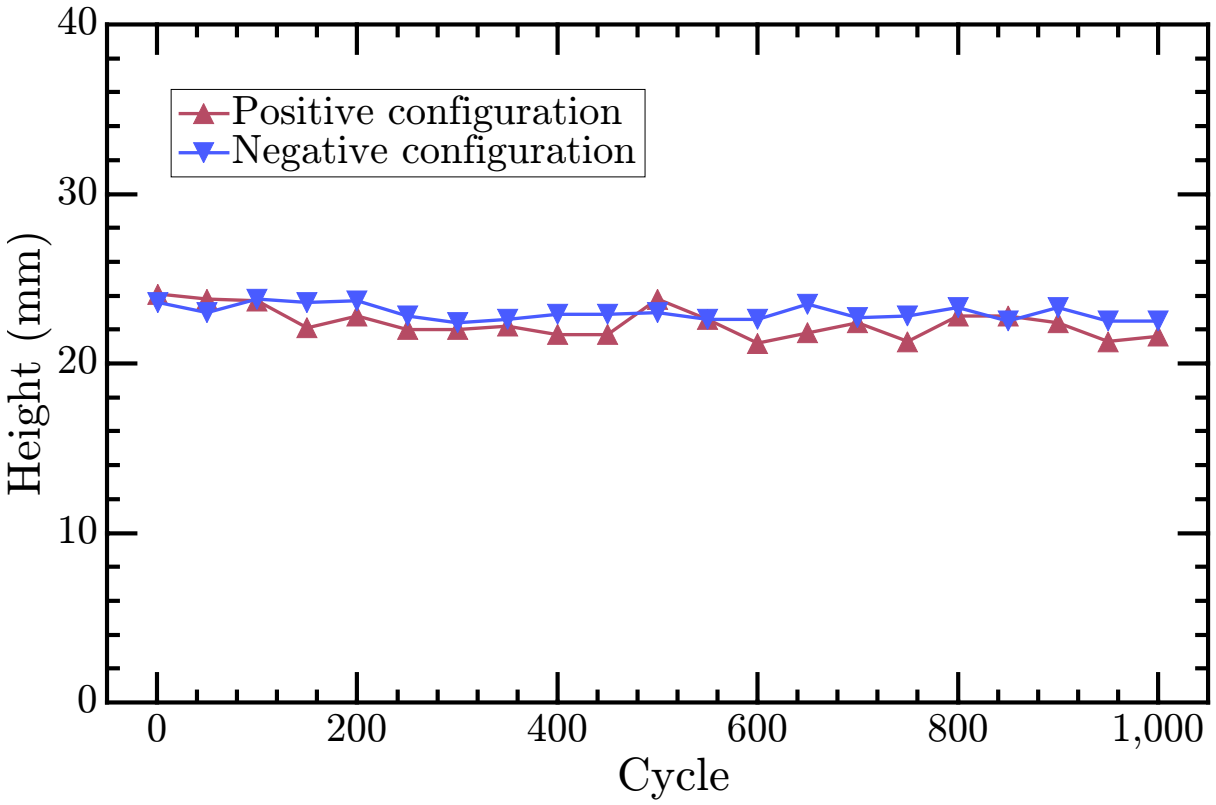

Figure 3.11: Cycling test of a bistable dome. The height of the dome as a function of cycling number over time. The switching of the dome between its two was achieved by manual manipulation by hands. After every 50 cycles, we measured the heights in both positive and negative configurations [67].

Extending this cyclic testing to over 1000 cycles allowed us to thoroughly investigate the

endurance and consistency of the bistable structures under repeated use. This exhaustive testing regimen revealed that the heights of the structures in both their positive and negative configurations exhibited only marginal variations, even after extensive cycling. The results, illustrated in Fig. 3.11, underscore the remarkable reversibility and robustness of these trilayer bistable structures. The negligible changes in dimensions after a significant number of cycles highlight their potential for applications requiring durable and reliable mechanical performance.

3.10 Multistability

As the ratio $\frac{L}{t_s}$ increases to around 80 (with $L = 80$ mm), we observe the emergence of multiple free-buckling mode shapes in the positive and negative configurations, as illustrated in Fig. 3.12(A,B). This phenomenon is not evident in composite structures with smaller $\frac{L}{t_s}$ ratios, as depicted in Fig. 3.9(A,B). For the kirigami composite with $L = 80$ mm, a systematic variation reveals that at a low pre-stretch, the free buckling shape is predominantly characterized by mode 1, as defined in Fig. 3.12(A,B). As the pre-stretch increases, a transition to mode 2 becomes apparent. In this mode, the four edges of the cross-sections begin to buckle locally, leading to different buckling directions in the two modes. This results in variations in the height of the two modes, presented in Fig. 3.12(C). Given the symmetry of the trilayered structure, the soft structures in this scenario exhibit four stable configurations. Such multistable behavior not only enhances the mechanical properties of the structure but also paves the way for conducting systematic analytical research to comprehend the mechanisms underlying the multi-stability phenomena in future studies.

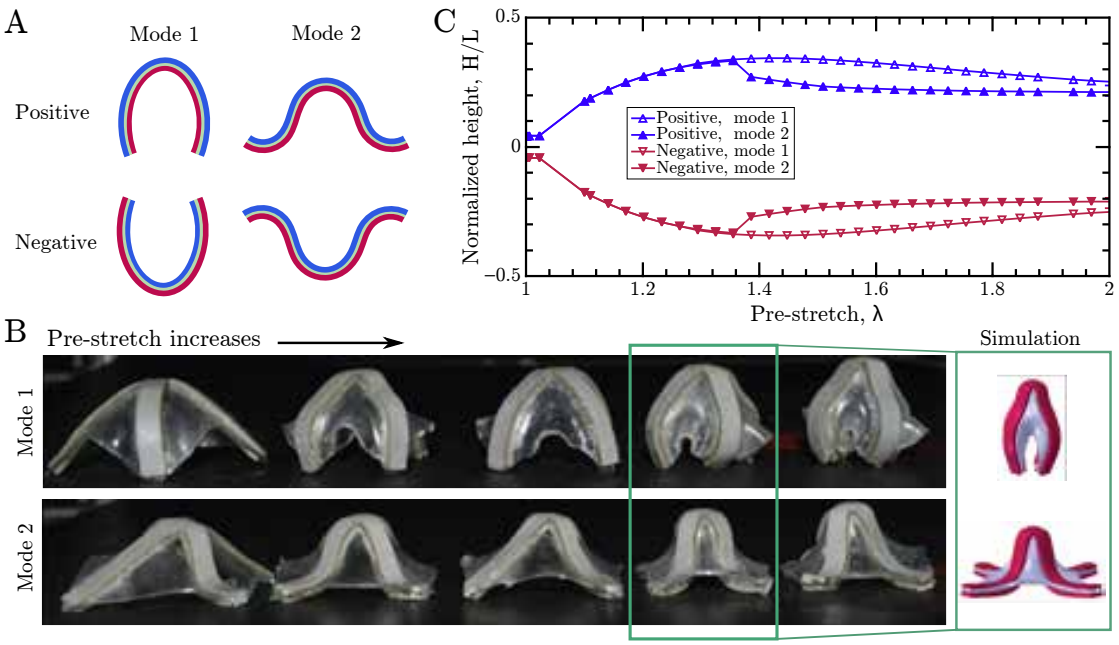

Figure 3.12: (A) Sketches of free-buckling mode shape 1 and mode shape 2 in the "positive" and "negative" configurations. (B) The free buckling shapes for the cross-shaped kirigami composite structure (L = 80 mm) at different amount of pre-stretch λ = 1.2, 1.4, 1.6, 1.8, 2.0. The Mode 1 and Mode 2 are also predicted in simulations. (C) The simulated variation of normalized height of the two modes in the "positive" and "negative" configurations as a function of pre-stretch λ [67]

3.11 Soft Gripper

3.11.1 Introduction

Using the bistable krigiami deployables we created a universal, nondestructive soft gripper Fig. 3.13, that is capable of stably grasping delicate items such as strawberries or butter packets, demonstrating significant potential for applications across wearable devices, soft robotics, and multifunctional medical devices.

The soft gripper is primarily constructed from a bistable dome, which incorporates cross-shaped kirigami layers, weighing a mere 4.2 grams. This dome is functionally integrated with an extending shape memory alloy (SMA) spring and a mechanical pusher. The bistable nature of the dome means it maintains one of two stable states: an upward stable equilibrium

which is its default state, and a downward position which it snaps into under activation. The central component, the bistable dome, is affixed at the end of a rail which facilitates linear motion. The SMA spring, anchored at one end of the rail, connects to the pusher at the other end. Activation of the spring through Joule heating allows the pusher to slide along the rail, forcing the dome to snap through to its alternate stable state. This enables the gripping and releasing processes for the gripper.

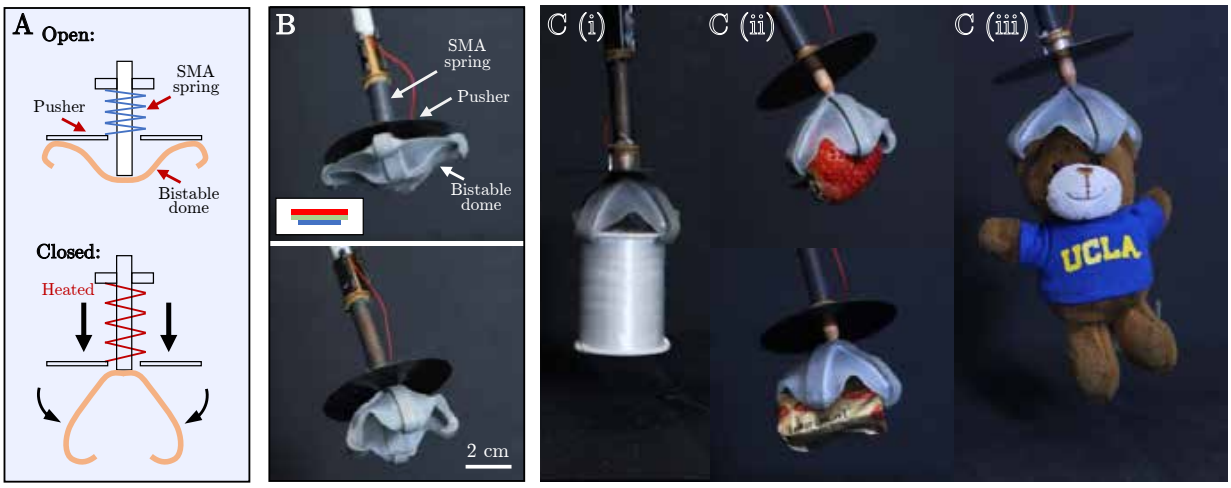

Figure 3.13: A) The mechanism of a soft griper composed of a bistable dome actuated by an extending shape memory alloy(SMA) spring. (B) The detailed structure of the gripper with labels. (C) The gripper has the ability to gently grasp delicate objects of different shapes and sizes [67]

The pyramid-shaped kirigami deployable was used to create the soft gripper. By extending the top kirigami and substrate layers at the edges, the device was modified to include hook-shaped tips that improved grip. This modification not only aided in grasping but also showcased the potential of our design approach to create more sophisticated 3D structures through a simple, monolithic planar process.

	Soft-Gripper	Autonomous Flytrap
Final 3D Shape	Pyramid	Hemispherical Cap
Kirigami Shape	Plus, L = 60 mm, w = 5 mm	Lotus with 8 petals and 30% material cut
Substrate Shape	Square	Circle
Size	Length/thickness = 60	Outer Radius = 40 mm Inner Radius = 16 mm
Pre-stretch λ	80%	80%

Table 3.2: The design parameters used for the soft robotic applications [67]

Our demonstrations highlighted the gripper's capability to handle a variety of fragile objects with ease. It successfully grasped items ranging from a 15-gram strawberry to a 25.3-gram cable spool, showcasing its versatility and reliability under moderate disturbances. Notably, the gripper requires energy only during the transition between stable states, not for maintaining a grip. This energy efficiency is particularly advantageous for applications requiring prolonged periods of gripping, potentially reducing operational costs significantly in applications where longer grasping time is necessary.

3.11.2 Analytical Formulation

The design of our kirigami-deployable grippers assumes point contacts with the grasped object at the four edges of the cross-shaped kirigami layer. This design enables precise control over the gripping force applied to the object, ensuring both stability and minimal risk of damage. Herein, we present the analytical formulation for the gripper which predicts the maximum weight that it can hold if created from a given kirigami deployable structure.

In our model, as detailed in Fig. 3.14, the weight of the object is counteracted by two primary forces at the contact points: the normal force N and the friction force f. The relationship between these forces is dictated by the coefficient of friction μ, where the friction force f is given by:

$$f = \mu N = \frac{2\mu E_k I_k \kappa_k}{L} \tag{3.17}$$

E_k represents the bending stiffness, and I_k is the moment of inertia of the kirigami strips,

which can be approximated by $2L^3w/12$ where L and w denote the length and width of the strips forming the cross shape kirigami, respectively.

The curvature κ_k of the gripper, essential for understanding its mechanical response, is related to the height H of the pyramid-like 3D shape. This relationship is expressed through the geometric arrangement of the gripper:

$$\kappa_k = \frac{2}{L}\tan\left(\arcsin\left(\frac{2H}{L}\right)\right) \tag{3.18}$$

From this, using force balance, the total force G that the gripper can exert on an object, combining the effects of both friction and normal forces, is derived as:

$$W = 4(f\cos(\theta) + N\sin(\theta)) = 8E_kI_k\kappa_k(\mu\cos(\theta) + \sin(\theta))/L \tag{3.19}$$

where θ is the angle of inclination of the force, calculated as:

$$\theta = \pi/2 - \arctan\left(L\kappa_k/2\right)) \tag{3.20}$$

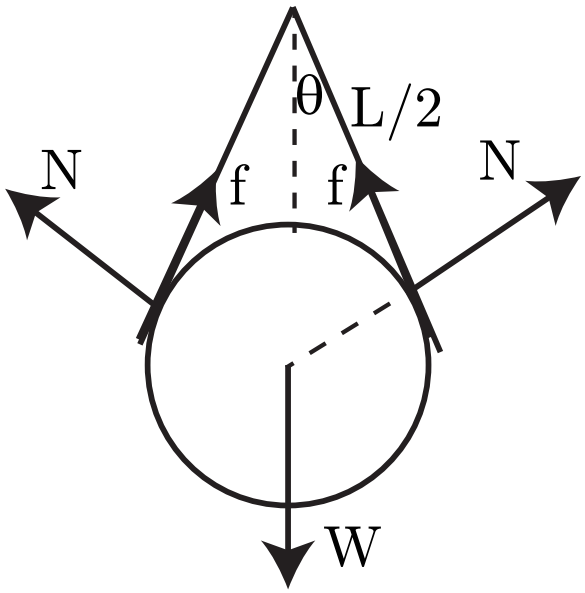

Figure 3.14: The sketch of a gripper grasping an object of mass m [67]

Given a friction coefficient μ of approximately 0.1 for the gray VHB^{TM}, and using the derived formulas, the gripper is designed to securely hold objects weighing close to 24 grams, consistent with experimental validations using a cable spool of similar weight Fig. 3.13(C(i)). This calculation underscores the efficacy of the gripper in handling delicate and lightweight objects, ideal for applications requiring precision and care.

3.12 Autonomous Flytrap

3.12.1 Introduction

We also use the bistable kirigami deployables to create an autonomous flytrap inspired robot Fig. 3.15. This device is designed to autonomously and passively sense and capture objects, leveraging the quick-acting mechanics inspired by the natural motion of a Venus flytrap. The bistability inherent in these structures allows the robot to maintain two different stable states — an open state ready for object detection and a closed state for capturing the object.

In the open state, the flytrap-inspired robot remains passively waiting for interaction with an external object. The transition to the closed state is triggered by a minimal loading force that overcomes the energy barrier set by the bistable configuration. In these demonstration we include a small magnet to push the transition to happen. Furthermore, this force is calculated based on the bending stiffness of the structure and the curvature designed into the kirigami layers. Upon detecting a sufficient force — generally through direct contact by an object — the bistable mechanism is activated, causing the robot to swiftly snap to its closed position. This action is rapid, occurring within fractions of a second, mimicking the fast response of biological flytraps. This rapid closure is essential for effectively capturing moving or suddenly appearing objects within the robot's operational environment.

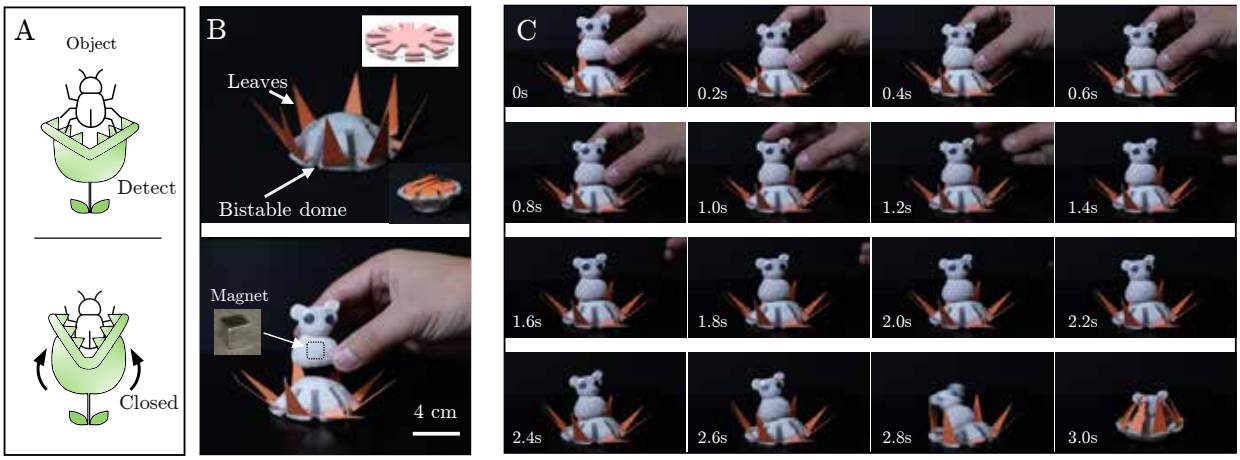

Figure 3.15: (A) This strategy can be mimicked by mechanically embedding sensing and actuation into structures by using a bistable dome. (B) A magnet was inserted into the bottom of the object. With the help of the magnetic force, the snap-through of the dome could be directly triggered by the touch of the toy. (C) Snapshots show the autonomous object detection and quick closing of leaves without requiring external sensing, control, and actuation. To help overcome the energy barrier of the bistable dome, we attached a permanent magnetic bead on the bottom of the object while placing another one underneath the platform [67].

The entire system is designed to function without the need for continuous energy input or complex sensor systems. The simplicity of the mechanical design reduces the need for maintenance and energy consumption, making it highly efficient for prolonged use in field applications where power resources may be limited.This flytrap-inspired robot not only demonstrates the potential for these structures to replicate complex biological movements but also opens up possibilities for designing autonomous soft machines capable of interacting with their environment in innovative ways.

3.12.2 Analytical Formulation

To demonstrate the flytrap, we have used the hemishperical cap kirigami deployable with properties defined in Table 3.2. The force required to trigger this autonomous flytrap-inspired robot is calculated as follows:

$$G = \left.\frac{\partial E_b}{\partial z}\right|_{z=H} = \left.\frac{\partial \frac{1}{2} A D_{\text{eq}} \kappa^2}{\partial z}\right|_{z=H} \tag{3.21}$$

In this expression, $\kappa = 8z/L^2$ represents the curvature, related to the vertical displacement z and H is the specific height at which this restoring force is calculated. From these parameters, it's determined that a minimum force of about 0.7N is needed to overcome the energy barrier and close the gripper.

This mechanism's functionality is demonstrated using a soft toy resembling a UCLA plush bear Fig. 3.15, weighing approximately 12.6 grams $>$ 0.7 N. The rapid snap-through action of the robot's dome allows it to quickly and safely grasp the toy, exemplifying the practical application of the calculated force in a real-world scenario. The closing of the gripper happens within 0.4 seconds, showcasing not only the speed but also the precision and reliability of the device in handling delicate objects without causing damage. This fast actuation and gentle grasping capability highlight the potential of such bistable mechanisms in applications requiring quick response and sensitive handling

3.13 Bistable Actuator

3.13.1 Introduction

With a concept very similar to that of the trilayered composites, we also present our work on the bistable actuators [71]. Bistable actuators are advanced devices in soft robotics that can maintain two distinct stable configurations without the need for continuous energy input. These actuators operate on the principle of snap-through instabilities, which allow them to switch quickly and reversibly between their configurations through short, controlled impulses of stimulation Fig. 3.16(B). This ability to change shape rapidly while conserving energy makes bistable actuators particularly valuable for applications requiring dynamic shape adaptation with minimal power consumption.

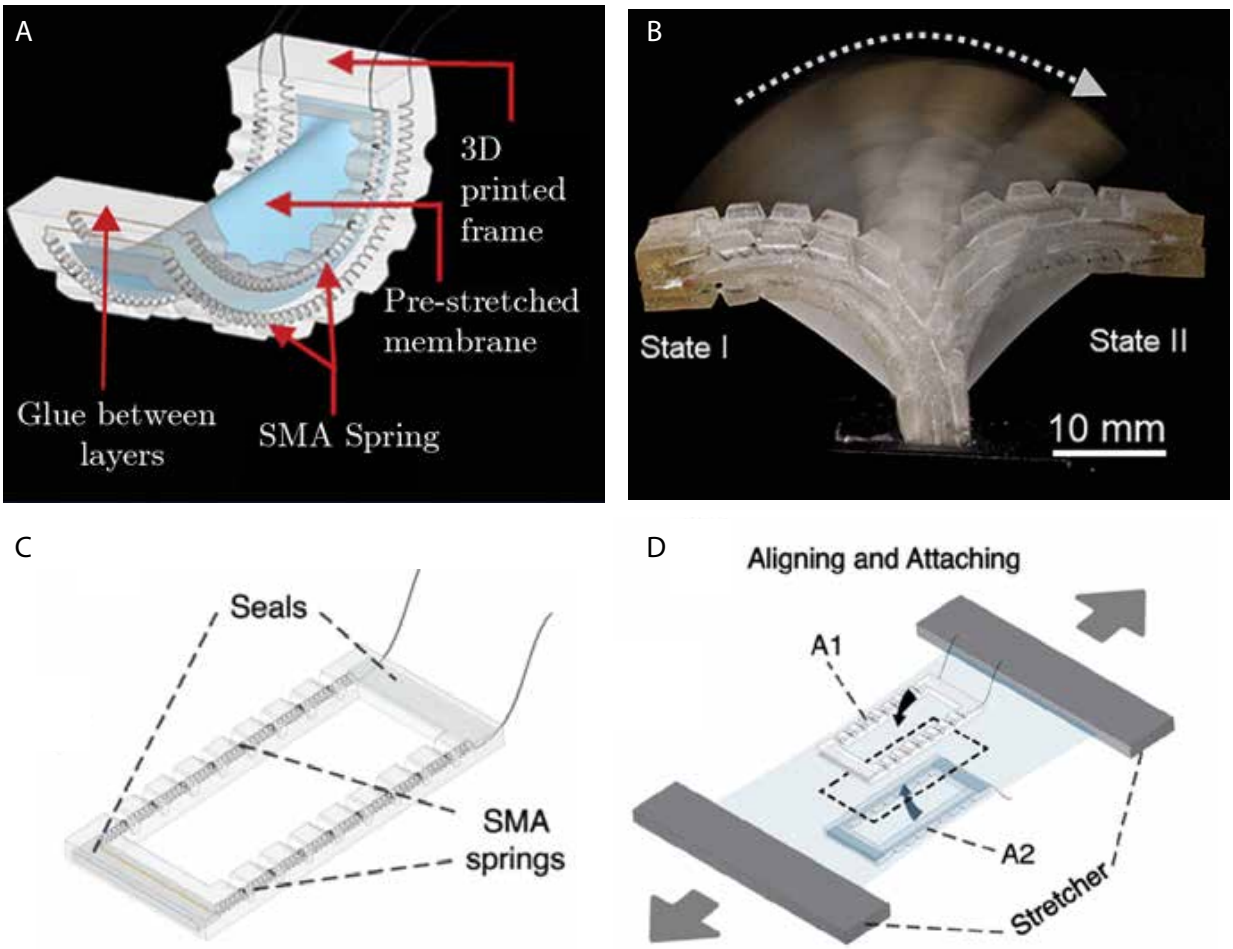

Figure 3.16: (A) Schematic view of bistable actuator (B) Picture of bistable actuator triggered from state I to state II (C) Creation of the frame with the included SMA wire (D) Putting together the layers - the two frames and the stretched membrane - of the composites to create the bistable actuator [71].

Applications of bistable actuators are diverse and impactful across multiple fields. They can be used in the design of soft robots capable of high-speed locomotion and adaptive morphology, soft grippers for fast and secure grasping, soft valves for precise fluid control, and even in the development of reconfigurable 3D electronics. Each application benefits from the ability of bistable actuators to perform reliable, energy-efficient, and rapid transformations, which enhance the functionality and adaptability of soft robotic systems.

The bistable actuators, however, were created similar to the way trilayer kirigami composites were manufactured as shown in Fig. 3.16(A). A VHB^{TM} tape was stretched uni-

directionally and two identical pieces of 3D-printed soft rubber frames were connected on the top and the bottom Fig. 3.16(D). SMA wires were embedded within the kirigami frames Fig. 3.16(C) to later initiate the snap-through actuation between the two stable configurations. The ends of the SMA coils within the frames are secured using a durable urethane adhesive to ensure they remain in place

Owing to this method of manufacturing, the simulations presented in section, could be extended to simulate these actuators. However, with different materials involved made it necessary to again carry out a detailed material modelling process to enumerate the properties. Hence, the following sections talk in detail about the simulations for these bistable actuators.

3.13.2 Material Modelling

The material modeling of the VHB^{TM} 4905 tape, used in the construction of bistable actuators, was approached similarly to that of trilayer kirigami deployables. This modeling began with conducting tensile tests on the VHB^{TM} tape, an integral component akin to the layers used in trilayer structures. The tests utilized samples laser-cut into the shape of ASTM D412 specimens, with orientation ensuring that the longest dimension was placed in the tensile direction. The strain rate for these tests was set at 10 mm/min, and the resulting stretch-stress data were meticulously recorded [71].

Curve fitting techniques were then applied to this data to extract parameters for various hyperelastic models, including the Yeoh, Ogden, and Mooney-Rivlin [69]. The results of these fittings were illustrated in Fig. 3.17, with the experimental data depicted as a black solid line and the fitted curves as red dashed lines.

These fitting results were crucial in applying analytic and numerical models to predict the stable state curvature of the bistable actuators. Predictions from the (Yeoh Fig. 3.17(A,B)), (Ogden Fig. 3.17(C,D)), and (Mooney-Rivlin Fig. 3.17(E,F)) models were compared against experimental observations of bending curvature at static equilibrium. This comparison showed that all three models provided reasonable matches with the experimental data. No-

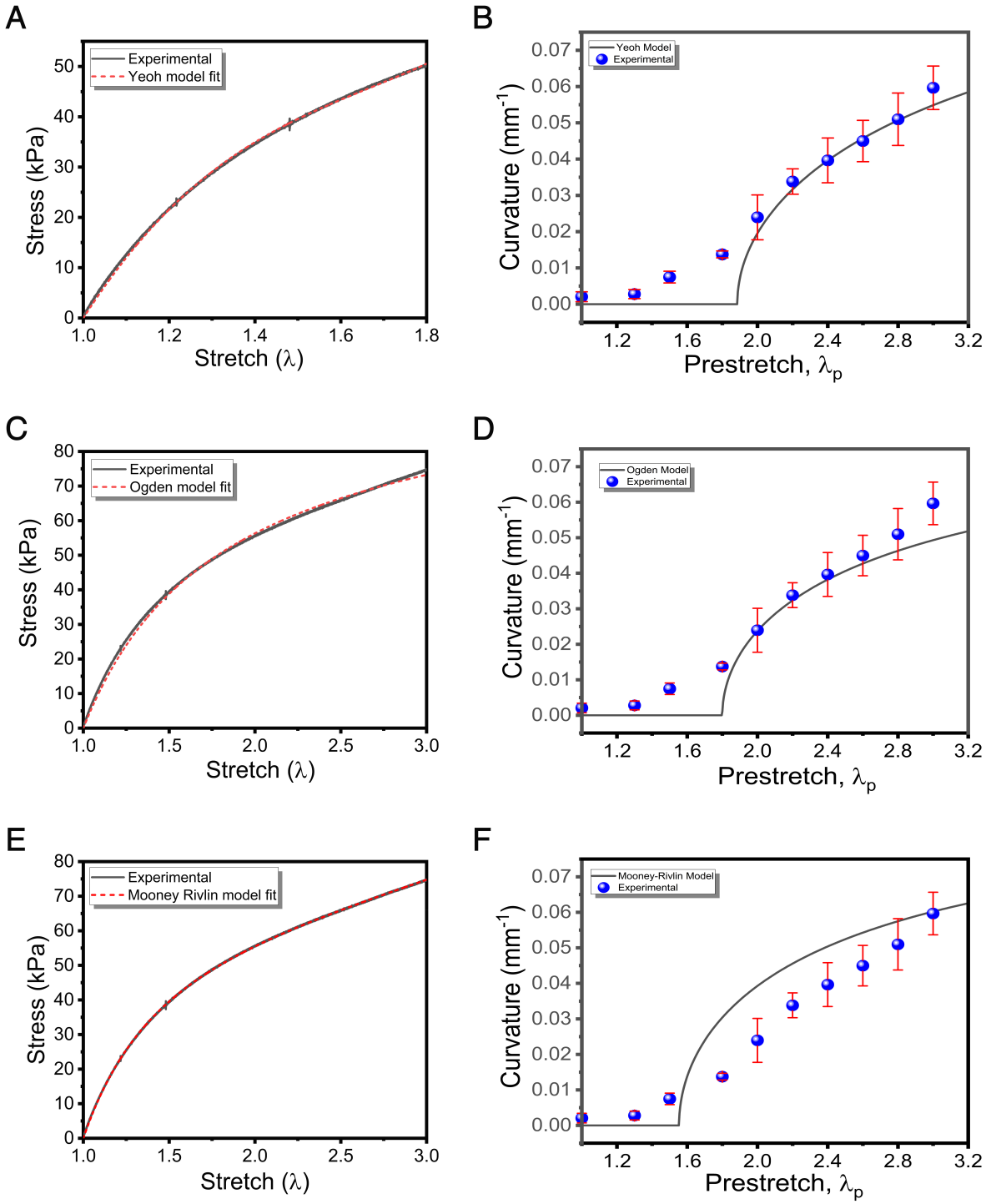

Figure 3.17: (A) The stretch-stress curve fitting result of the Yeoh model. (B) The comparison of the Yeoh model's prediction of stable-state angle and the experimental data points. (C) The stretch-stress curve fitting result of the Ogden model. (D) The comparison of the Ogden model's prediction of stable-state angle and the experimental data points. (E) The stretch-stress curve fitting result of the Mooney-Rivlin model. (F) The comparison of the Mooney-Rivlin model's prediction of stable-state angle and the experimental data points [71].

tably, the Ogden and Mooney-Rivlin models demonstrated excellent agreement with the experimental data. We observe particularly the Ogden model, which exhibited superior agreement across the full range of prestretches relevant to the fabrication of the bistable actuators.

The Ogden model was thus, chosen for the numerical simulations owing to its excellent agreement and consistency over a higher range of pre-stretches involvedin the manufacturing process. The engineering stress-pre-stretch relation for this model was given as:

$$\sigma_{\text{Ogden}} = \mu(\lambda^{\alpha-1} - \lambda^{-(\frac{\alpha}{2}+1)}) \tag{3.22}$$

where μ and α are the Ogden parameters of the substrate. The values of these parametesrs for the fitted data turn out to be $\mu = 71.3127457kPa$ and $\alpha = 1.1679539$

The flexural rigidity of the frame was determined using a buckling test, as illustrated in Fig. 3.18. Initially, a bistable actuator was fabricated with a non-stretched membrane, i.e., $\lambda_p = 1$. Given the relative thinness of the membrane, its contribution to the flexural rigidity was significantly lower than that of the frame, rendering its effect negligible in the buckling test. The setup for the test involved placing the stacked frame such that both ends are rotation-free but translation-fixed, as depicted in Figure S3. The strain rate applied during the buckling test is 10 mm/min.

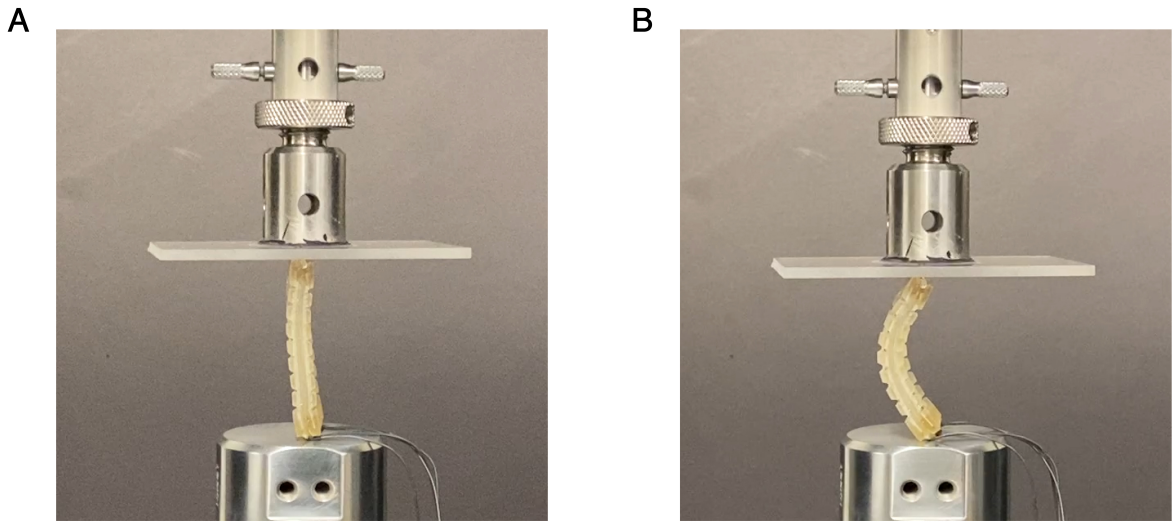

Figure 3.18: Testing the flexural rigidity of the frame (A) The default placement of the load cell and the stacked frame with a nonstretched VHB$^{\text{TM}}$ membrane. (B) The structure bends to form a curved shape under a buckling load [71].

According to Euler's formula for critical load, the relationship between the critical load F_{critical} and the flexural rigidity D_f was given by:

$$D_f = \frac{F_{\text{critical}} \cdot (KL_f)^2}{\pi^2} \tag{3.23}$$

Here, the factor K was set to 1, due to the boundary conditions of the frame being rotation-free and translation-fixed. Based on the average maximum load observed during the tests, the calculated approximation of the flexural rigidity of the stacked frame was $D_f = 6.6654 \times 10^{-5}\,\text{N} \cdot \text{m}^2$

Using this value of flexure rigidity, and a Poisson's ratio of 0.5 (fully plastic), we assumed a linear elastic model and computed the Young's moduls (E_f) of the frame as:

$$E_f = \frac{12D_f}{A_f} \tag{3.24}$$

whereA_f is the area of the frame. Doing so, provided the value of $E_f = 411.444kPa$.

Finally, since the two ends of the frame were fully sealed, the existence of the glue

exhibited considerably greater rigidity compared to the bending portion of the frame. Consequently, the elastic modulus of these two ends was set at a value 1000 times greater than that of the rest of the frame, which was 411.444 MPa.

3.13.3 Numerical Simulations

The numerical simulation was conducted using the finite element method (FEM) in ABAQUS (SIMULIA, Dassault Systèmes). The above defined three different material models were utilized to model the sandwich structure of the actuato. To simplify the computational complexity, a conventional shell model was employed, utilizing a 3-node conventional shell element with reduced integration (S3R type) for each of the three layers. These layers were differentiated solely by the position of the elements in the X-Y plane. This was done by changing the material property of each element based on the existence of the frame or kirigami layer at that position. They were modeled as being perfectly bonded to each other through tie constraints using the SPOS-SNEG shell contact definitions.

One corner of the structure was fixed, while the other three corners were set as roller-based boundary conditions to restrict motion in the vertical direction (Z-direction), facilitating the generation of stable simulation videos. A pre-defined tensile stress was applied in the X-direction on the membrane, corresponding to the prestretch λ_p, using the stretch-stress formula of the Ogden hyperelastic model. It is important to note that the input for the simulation was true stress, thus necessitating a conversion from engineering stress as defined by:

$$\sigma_{\text{Ogden,true}} = \lambda \cdot \sigma_{\text{Ogden}} = \mu(\lambda^{\alpha} - \lambda^{-(\alpha/2)}) \tag{3.25}$$

A nonlinear, quasi-static solution procedure was implemented, with a non-zero but tiny distributed gravitational load to nudge the simulation towards one of the two bistable configurations of the actuator. As the simulation progressed for various prestretches λ_p, local deformation Fig. 3.19(A,C,E,G) and local stress Fig. 3.19(B, D, F, H) were recorded. Observations indicated that under low prestretch, the local stress on the elastic membrane was more uniformly distributed, while under high prestretch, stress concentrations were more

pronounced at the two ends of the membrane, particularly at the four edges where yielding in the actual actuator was predominantly observed.

Finally, the nodal coordinates of the structure were collected for curvature output. These configurations were analyzed in MATLAB, selecting five equally distributed points along one of the long sides of the frame to perform a circular fit. The stable state curvature derived from the numerical simulation results was as displayed with green dots in Fig. 3.20, aligning with the experimental data (shown as blue dots) and the Ogden analytic model (depicted as a black line) in terms of trends. The curvature showed slight deviations at large prestretches, which could be attributed to the errors introduced by the simplifications in the shell model.

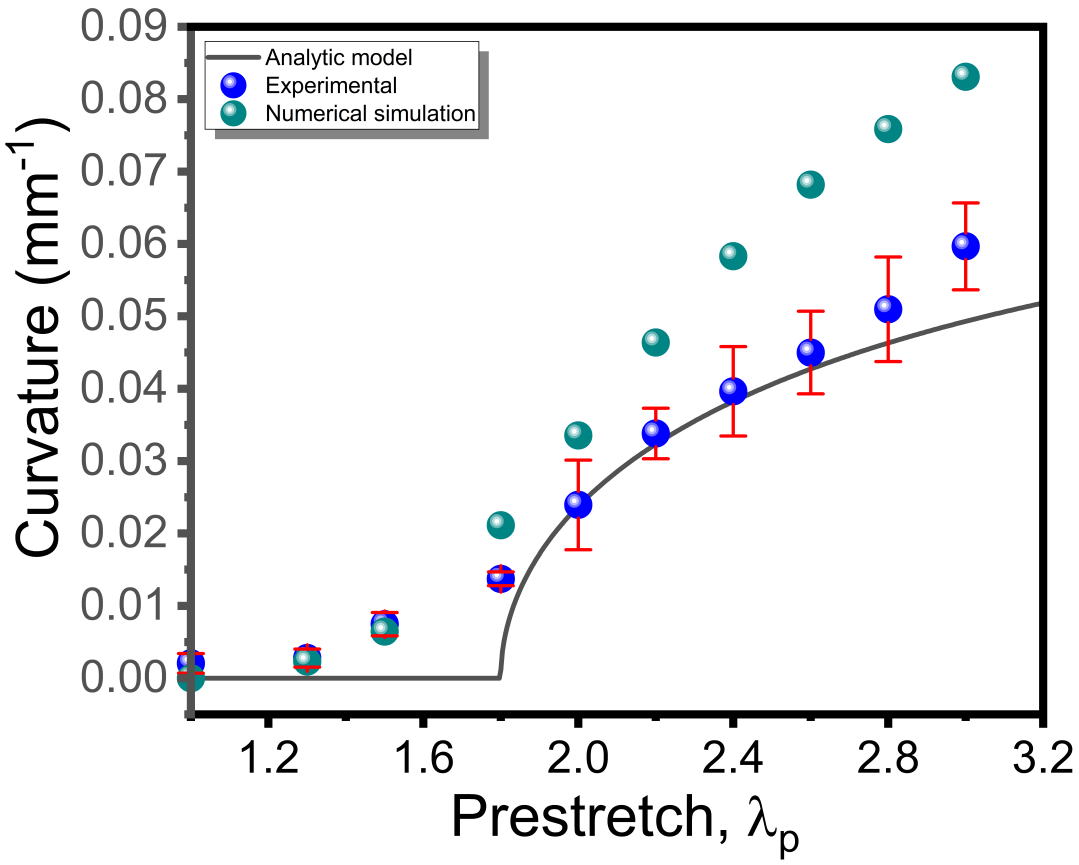

Figure 3.20: Initial curvature of bistable actuator for experimental, analytic (Ogden) model and numerical simulation with different prestretch (λ_p) [71].

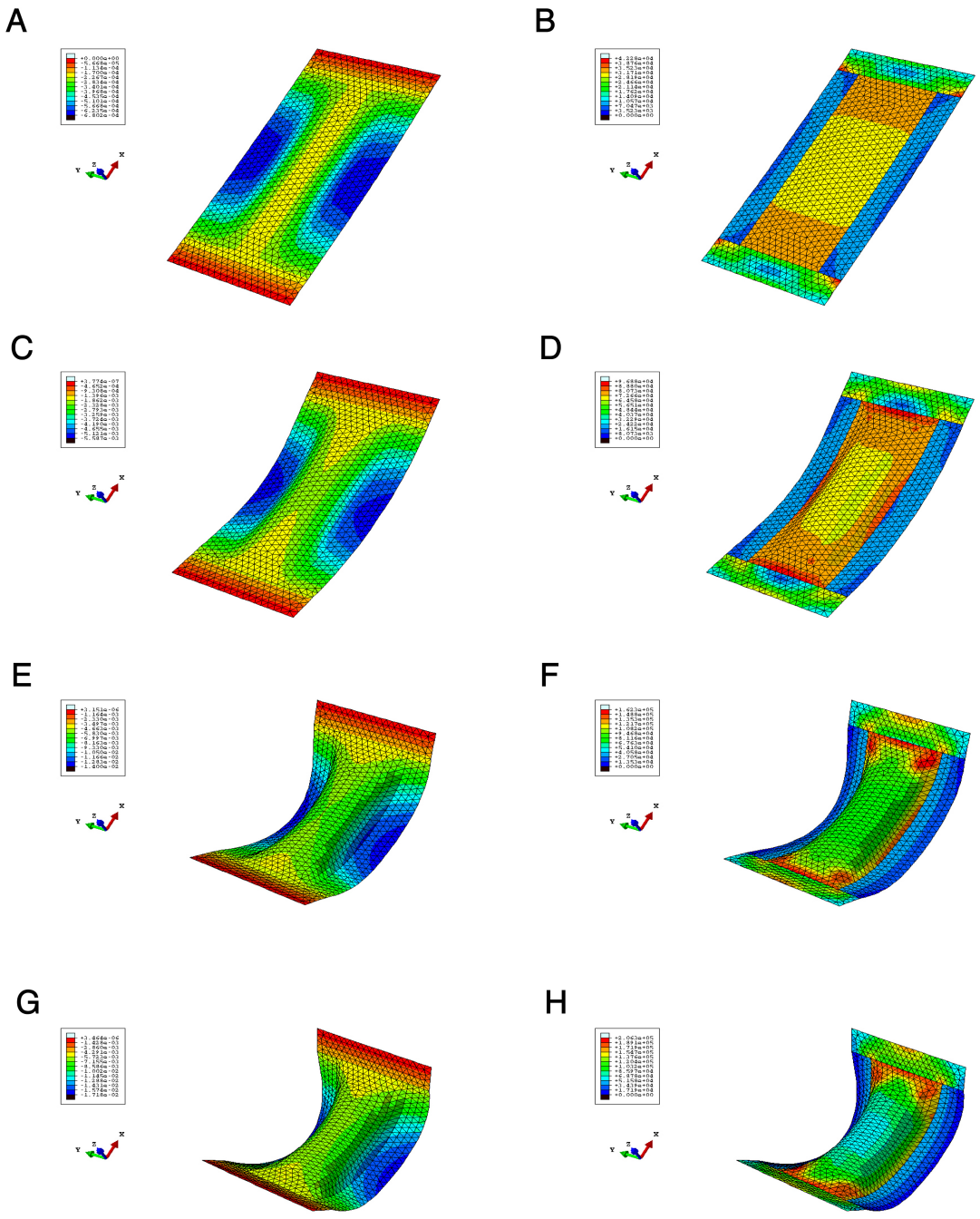

Figure 3.19: Numerical simulation result. (A) Deformation and (B) stress result when $\lambda_p = 1.3$. (C) Deformation and (D) stress result when $\lambda_p = 1.8$. (E) Deformation and (F) stress result when $\lambda_p = 2.4$. (G) Deformation and (H) stress result when $\lambda_p = 2.8$ [71].

3.14 Conclusion

In this section, we explored the concept and development of bistable kirigami deployables, beginning with the motivation for creating structures capable of multiple stable configurations. We detailed the design and experimental manufacturing processes that enable these deployables to switch between configurations smoothly, similar to biological motions. This included the application of bi-axial stretches and the integration of kirigami cuts, enhancing the functionality and adaptability of the structures.

Further, we delved into material modeling and numerical simulations, which are crucial for understanding the behavior of these deployables under various conditions. Material modeling focused on identifying the hyperelastic behavior of the used materials, while simulations helped validate the design concepts and predict the deployables' responses under mechanical stress. These sections collectively highlighted the potential of bistable kirigami deployables in applications ranging from soft grippers to robotic actuators.

CHAPTER 4

Inverse Design Algorithm for Kirigami Deployables

4.1 Introduction

Having established a method to fabricate deployable structures that assume predetermined shapes through soft kirigami composites, our objective extends to crafting any specified target shape. This necessitates predicting all requisite design parameters tailored to the specific application in question. The primary parameters in this context include the prestretch, size, and kirigami patterns of the structure. Consequently, to provide a robust solution, it is imperative to address the inverse design problem associated with these deployable structures, delineating a methodological approach for determining the optimal configurations that meet the desired functional and aesthetic criteria.

Inverse design is an essential methodology in modern engineering and technology, where the desired outcome dictates the design process rather than traditional methods that start with predefined parameters. This approach is necessary in applications where specific performance characteristics are paramount, such as in the creation of optical devices [72], materials with unique properties [73], [74], and complex structural forms [75]–[77]. Traditionally, solving these inverse design problems often involved extensive simulations and iterative physical prototypes, which can be both time-consuming and resource-intensive.

However, these conventional approaches often struggle with the vastness of the design spaces and the nonlinear nature of the problems [78]–[80], making the process inefficient and sometimes unfeasible without significant computational and experimental resources. To address these challenges, modern techniques have shifted towards more computational approaches, such as machine learning [73], [76], [78]–[80], to better navigate the design space.

In the specific case discussed here [81], the inverse design problem of bilayered kirigami structures [14] is approached using Variational Autoencoders (VAEs) [82], [83] and active learning algorithms, marking a significant advancement in the field. VAEs are utilized to manage the complexity and high dimensionality of the design space. By encoding the kirigami cut patterns into a lower-dimensional latent space Fig. 4.1(A(i)), VAEs simplify the design parameters while retaining the ability to explore a wide variety of design configurations. This dimensionality reduction is crucial as it allows for quicker and more focused exploration of potential designs, reducing the computational load significantly.

Active learning further enhances this process by intelligently selecting the most informative data points for simulation Fig. 4.1(A(ii)). This method strategically directs the computational resources to areas of the design space where the model's uncertainty is highest or where the potential to improve the design is significant. Active learning thus ensures that each simulation contributes maximally to the model's learning, improving efficiency and accelerating the convergence towards optimal design solutions.

Together, VAEs and active learning provide a powerful framework for inverse design. This approach is distinguished by its efficiency and effectiveness, allowing for rapid iterations and adjustments based on computational predictions rather than physical prototypes. Such capabilities are especially advantageous in engineering domains where design conditions are stringent or where traditional methods fail to provide feasible solutions within reasonable time frames. This methodology not only exemplifies the evolution of design practices but also highlights the growing role of machine learning in enabling more sophisticated, adaptive, and efficient engineering solutions.

Utilizing upon these techniques, this chapter demonstrates the creation of various 3D shapes starting from a planar kirigami composite. By applying the outlined method, we successfully generate structures exhibiting reflectional symmetry, four-fold radial symmetry, and even structures characterized by a single axis of symmetry. The congruence between the predicted configurations and the actual manufactured shapes shows remarkable agreement, underscoring the efficacy of our approach. Moreover, we extend the application of this algorithm to the development of trilayered bistable kirigami structures [67]. This en-

hancement encapsulates our research, enabling the creation of any kirigami deployable, be it monostable or multistable, by accurately predicting its design parameters and subsequently manufacturing it to meet any specified target shape.

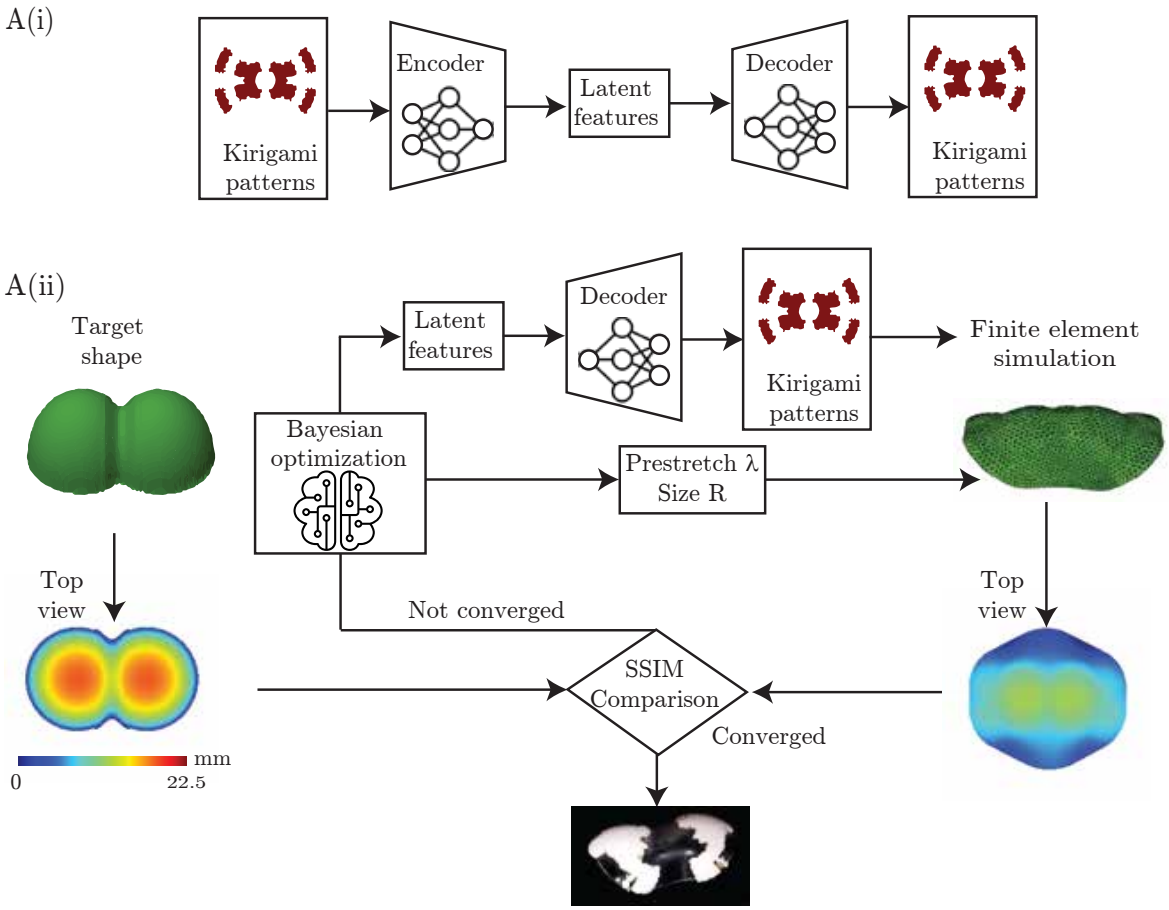

Figure 4.1: Flow chart of the data-driven design and optimization of soft kirigami composite. A(i) A VAE to reduce the dimension of kirigami patterns to a small number of latent variables. A(ii) A Bayesian Optimization loop that iteratively searches the optimal combination of latent kirigami pattern variables, size of the structure, and amount of prestretch that results to the target 3D topology [81].

4.2 Numerical Simulations

Numerical simulations form the backbone of the active learning process, which implies they should be accurate and computationally efficient. The finite element software ABAQUS is employed to simulate the nonlinear large deformation of hyperelastic composite structures.

Both the substrate and the kirigami layers were made from hyper-elastic materials, specifically 3M^{TM} VHB^{TM} tapes. In this instance, we opted for the white VHB^{TM} tape, previously used for bilayer structures, due to its higher stiffness which compensates for the absence of an additional layer compared to the trilayer setup. All material properties are provided in Table 3.1.

To optimize computational resources, each layer within the composite structure is represented as a shell similar to the simulation of the bistable actuators. The finite element analysis incorporates 3-node triangular shell elements for meshing both the substrate and kirigami layers. Specifically, the substrate is segmented into 2,772 triangular elements, which sufficiently prevents issues such as wrinkling and stress concentration. Both shell structures are aligned to ensure matching normals, and the center of the composite is anchored in place. The prestretch in the layers is simulated as isotropic thermal expansion. Herein, the thermal expansion coefficient of the krigami layer is set to 0 and that of the substrate is set to one. Since, this is a reverse process to that of extension, we have to employ a modified value for the temperature-based contraction.

$$\alpha = 1 \implies \epsilon_{sim} = \Delta T$$

$$\text{Experimental Stretch: } 1 + \epsilon = \text{ Simulation Contraction: } \frac{1}{1 - \epsilon_{sim}}$$

$$\implies \delta T = \frac{\lambda - 1}{\lambda}, \text{ where } \lambda = 1 + \epsilon$$

The 3D shape emerges from the planar precursor as you run the simulation. Each numerical simulation demands 1-3 minutes of wall clock time on a desktop computer with a Ryzen 2950wx CPU at 2.4 GHz, accumulating to approximately 5 hours for 100 simulations. Our machine learning-enhanced framework further reduces from potentially millions of simulations to about 100, without sacrificing accuracy, highlighting its efficiency and effectiveness.

4.3 Experiments

To validate our algorithm, it was essential to fabricate the kirigami shapes and compare the outcomes with our predictions. We employed a setup similar to that used for the trilayer kirigami composites[67], though here only a single kirigami layer was used. Fig. 4.2 depicts our experimental setup and the critical steps in the fabrication process. Herein there is only one kirigami layer as opposed to the two used in trilayer structures.

Similar to before, the kirigami patterns were precisely cut using a laser cutter. To address designs that included many isolated pieces resulting from randomly generated kirigami patterns, we maintained minimal connections between these pieces, such as a bounding circle, which could be easily severed later, until they were affixed to the substrate. Isolated pieces smaller than approximately 2 mm for a 5 cm large planar precursor were disregarded as they did not significantly impact the final shape.

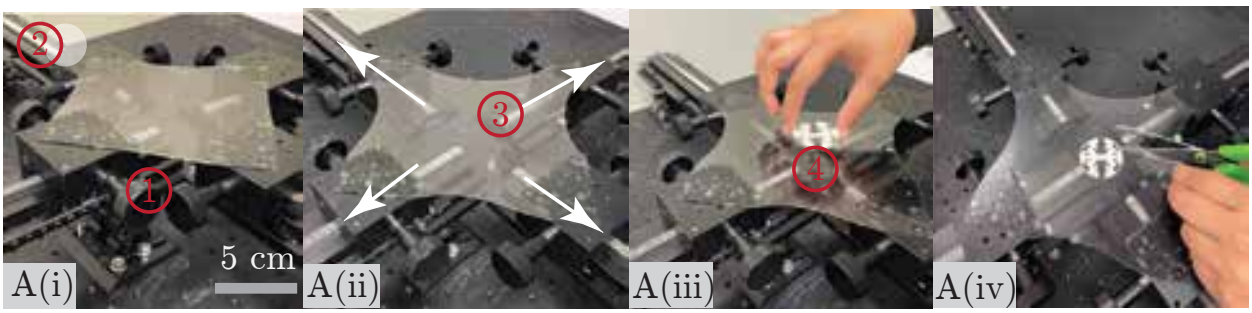

Figure 4.2: Experimental setup. A(i) Schematic representation of the system consist of two-knob stages (1) on 250 mm tracks (2) knobs to adjust the stage location. A(ii) Snapshot of the system when the substrate layer (3) is stretched. A(iii) Attach a kirigami layer (4) on top of the substrate layer. A(iv) Release the prestretch by cutting along the outline of the circular substrate [81].

4.4 Machine Learning Inverse Design Framework

4.4.1 Overview

Our framework leverages advanced machine learning techniques to transform two-dimensional kirigami patterns into complex three-dimensional shapes, specifically exemplified by the de-

sign of a soft peanut. This approach simplifies the exploration and optimization of the vast kirigami design space through a combination of variational autoencoders (VAEs) and Bayesian optimization, enhancing the precision and speed in achieving the desired final shapes. The process begins with the generation of diverse kirigami patterns, encoding these into a latent space for efficient exploration, and iteratively optimizing these patterns to meet specific morphological targets, achieving an SSIM as high as 0.91 in validation tests.

4.4.2 Dimension Reduction: Efficient Encoding of Kirigami Patterns

We use a VAE to compress the extensive, high-dimensional space of kirigami patterns into a manageable latent space, crucial for handling the complex patterns required to achieve the peanut shape. Each kirigami configuration is represented as a 64×64 binary matrix. These configurations were generated bye exploiting symmetry as described in later subsections. Using the VAE, this large set of configurations is then encoded into a latent space of significantly reduced dimensionality (Fig. 4.1(A)), typically six latent variables. This dimension reduction preserves the essential characteristics necessary for effective transformation while significantly reducing computational overhead. This setup allows for the generation of novel kirigami configurations that can effectively achieve complex shapes, specifically demonstrated through the peanut-shaped design.

4.4.3 Active Learning for Optimizing Kirigami Designs

Bayesian optimization is utilized to navigate the latent space effectively after dimension reduction. It strategically selects new data points that balance the need for exploring untested regions and exploiting known promising areas. This optimization uses the structural similarity index measure (SSIM) as a performance metric, which has proven to guide the optimization toward effective designs closely matching the peanut shape's target 3D structure.

Each iteration evaluates kirigami designs' performance, with SSIM scores guiding the selection process. The Bayesian model is continuously updated based on these evaluations, refining its predictions and selections to hone in on the optimal kirigami pattern that achieves

the highest fidelity in shape reproduction.

4.4.4 Generation of Candidate Kirigami Patterns

To populate the training dataset for the VAE, kirigami patterns are algorithmically generated to cover a diverse set of geometrical and symmetrical properties. These patterns, tailored to the specific symmetry requirements of the peanut shape, are first created in one quadrant and then symmetrically extended across the entire design space through mirroring and rotation (Fig. 4.3(A)). Similar method is followed for structures with four-fold radial symmetry where we started with half of the first quadrant before replicating it around. Both these methoda are displayed in Fig. 4.3(B). This method ensures a rich and varied dataset, enhancing the VAE's ability to learn and generalize from a comprehensive range of potential transformations.

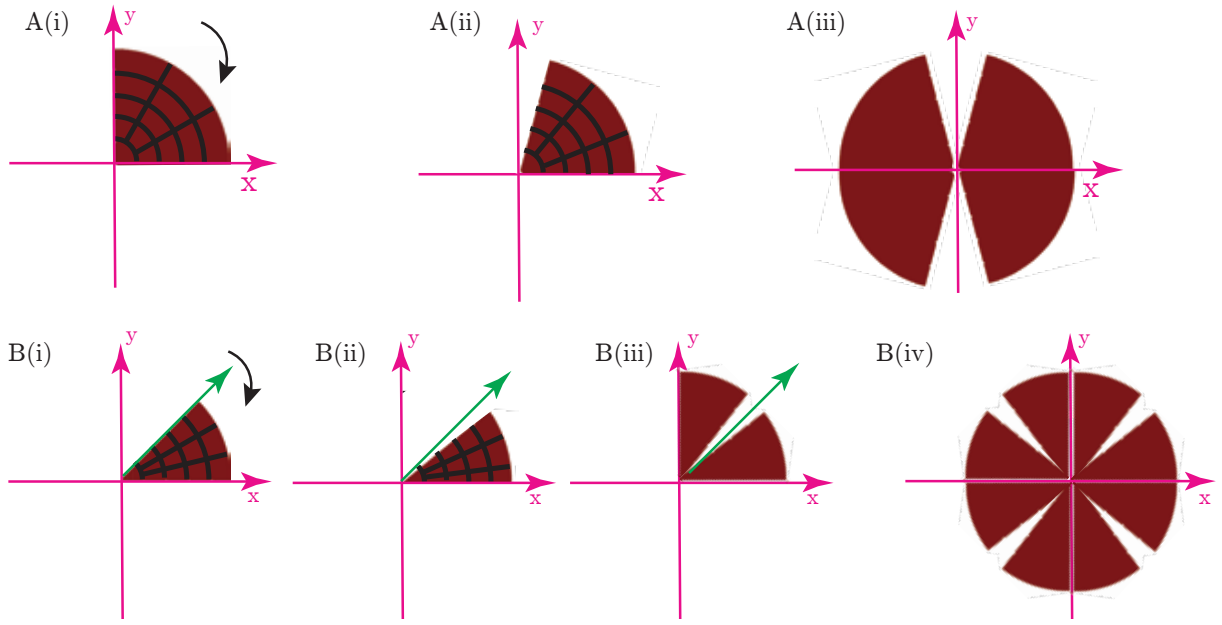

Figure 4.3: (A) Kirigami patterns that have reflectional symmetry. (B) Kirigami patterns that have four-fold radial symmetry [81].

4.4.5 Optimization Process and Evaluation Metrics

The optimization process critically refines kirigami pattern selection using Bayesian optimization, which iteratively improves design choices based on SSIM evaluations. Simulations

and physical prototype testing are conducted iteratively to match the kirigami designs to the peanut shape, with SSIM scores used to quantify the closeness of the match. During optimization, adjustments to latent variables directly influence the kirigami design outcomes, with the process continuing until an SSIM score approaching 0.91 is consistently achieved (Fig. 4.4(A)), indicating a high degree of similarity between the designed and target shapes.

It was observed that with a similar SSIM, multiple different optimum kirigami designs were predicted to achieve the same target shape. Theses predicted patterns also varied with the initialization shapes for the algorithms. However, closer observation showed that these kirigami designs had a certain similarity in pattern. Most importantly, for e.g. in the deign of the peanut, more material was concentrated near the two lobes of the peanut across the various kirigami designs (Fig. 4.4(B)). This led us to believe that minor differences in th kirigami design did not affect the final 3D shape. This further justifies the removal of tiny isolated pieces while experimentally manufacturing the structures simplifying the manufacturing process without affecting the overall shape.

However, despite the great variations in kirigami designs, the pre-stretches and radii of the different algorithm runs converged to values in a particular region (Fig. 4.4(B)). This leads us to the inference that even though there could be variations in the krigiami patterns, there exists an optimal range of these other design parameters to achieve a particular target shape.

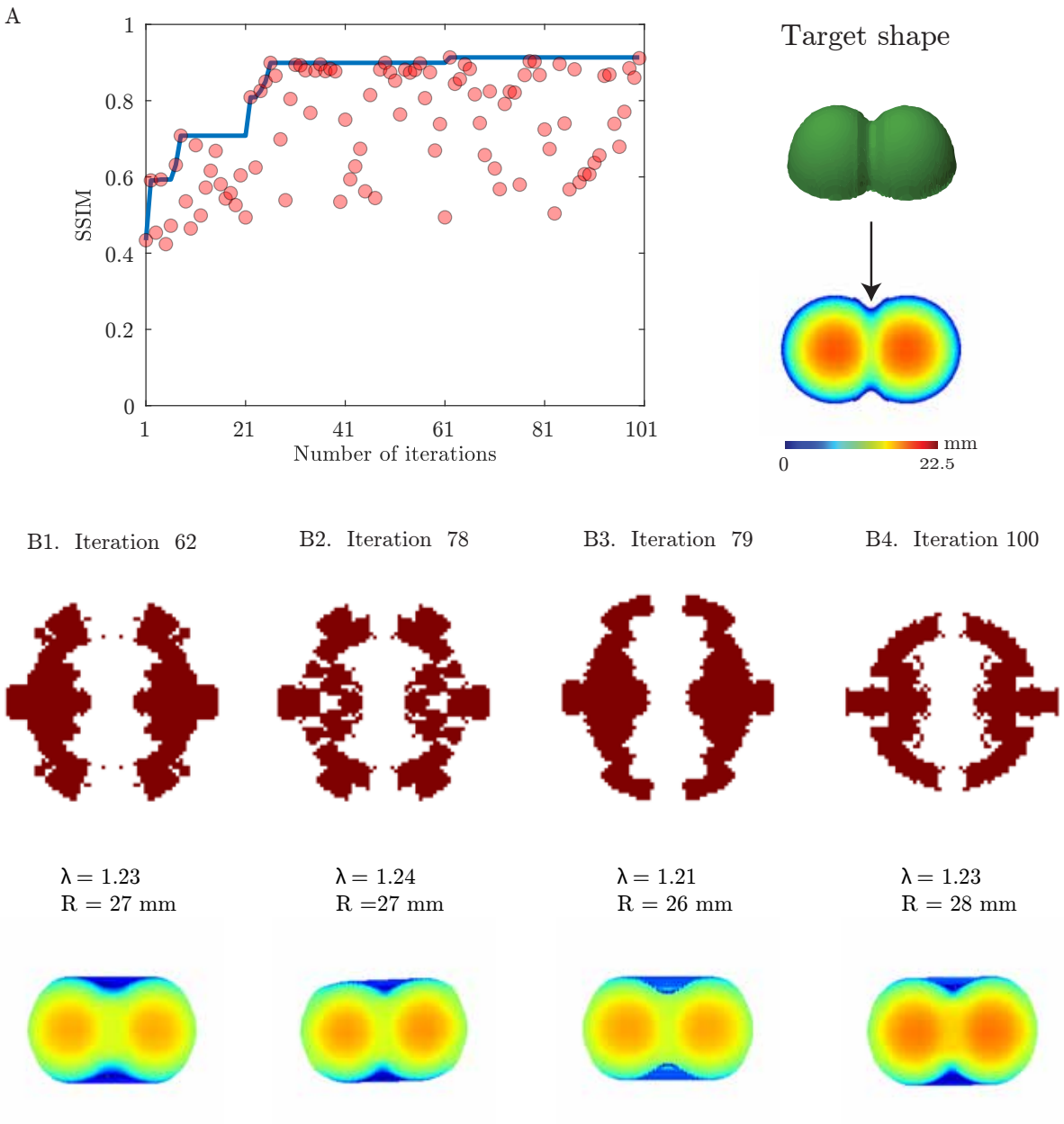

Figure 4.4: A) Search trajectory Variation of SSIM between target peanut shape and predicted free buckling shape over iterations. B) Multiple optimal solutions B1–B4)The top four optimal design solutions, including the kirigami patterns, prestretch and kirigami size. The corresponding height distribution for each design is presented at the bottom. [81].

4.5 Exploration Design of Various 3D Kirigami Shapes

In our study, we applied this machine learning inverse design framework to a diverse array of complex three-dimensional shapes, demonstrating the adaptability and depth of our approach across different symmetries and structural complexities. The peanut, pringle and ship hull shapes Fig. 4.5, featuring two-fold symmetry, were pivotal in testing the framework's ability to handle symmetrical yet intricate transformations. The peanut and pringles achieved a high structural similarity index measure (SSIM), confirming the model's precision. The ship hull challenged our approach with its pronounced curvatures and asymmetrical features that mimic the bow and stern of a ship, refining our ability to manipulate kirigami cuts for complex symmetrical shapes.

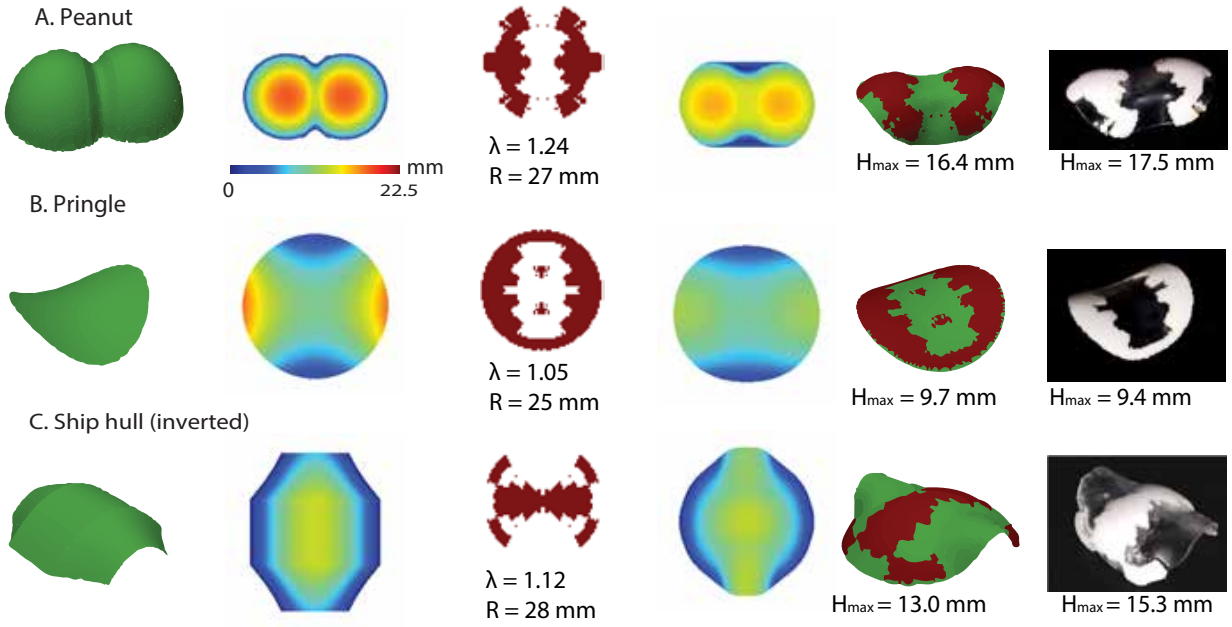

Figure 4.5: Inverse design of shapes with two reflectional axes of symmetry: Target 3D shapes: the first column shows different 3D shapes (A. a peanut, B. a pringle, and C. a ship hull) input to the optimization algorithm. Height-coded 2D image representations: the second column shows distribution of height for the target 3D shape. Optimal design parameters: the third column presents the optimized kirigami patterns, prestretch, and radius selected after 100 iterations. Height-coded 2D image representations of the optimal predicted shapes: the fourth column presents the height distribution of predicted 3D topology obtained from finite element simulation using the optimal design parameters. The SSIM are approximately in 0.9. The predicted 3D shapes: the fifth column shows the predicted 3D shape in simulation. The maximum heights for the 3D images are shown in the bottom. Experimentally realized morphing 3D soft structures with desired shapes: the sixth column shows the experimental result of the 3D topology given the optimal parameters [81]

Additionally, shapes with four-fold radial symmetry such as the flower and pyramid Fig. 4.6 further tested the framework's capability to generate patterns that maintain rigorous symmetry across multiple axes, essential for producing the detailed petal-like structures of the flower and the sharp, geometric lines of the pyramid. These shapes demonstrated the model's proficiency in managing radial symmetry and enhancing the aesthetic qualities of the designs.

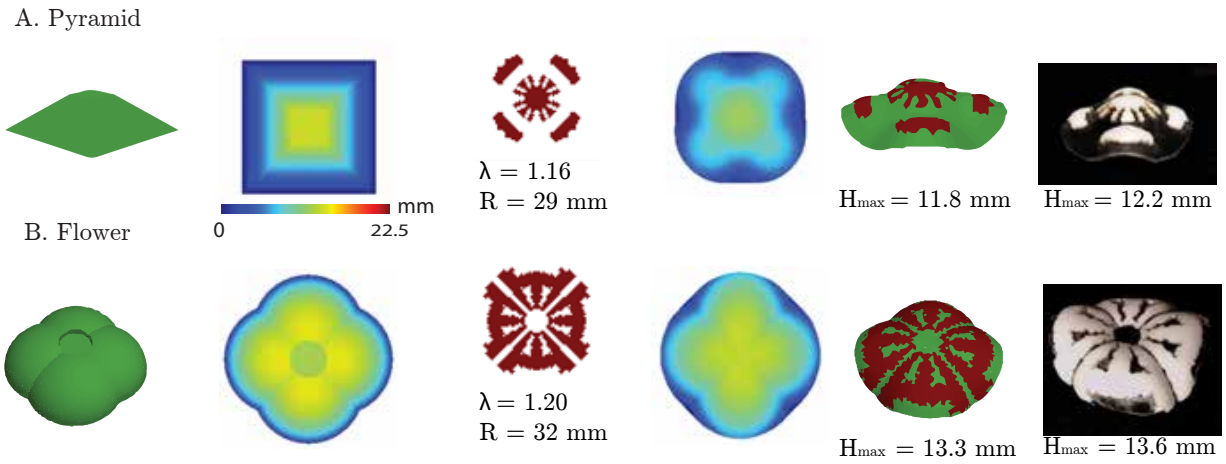

Figure 4.6: Inverse design of shapes with four-fold radial symmetry: Target 3D shapes: the first column shows different 3D shapes (A. a pyramid, and, B. a flower) input to the optimization algorithm. Height-coded 2D image representations: the second column shows distribution of height for the target 3D shape. Optimal design parameters: the third column presents the optimized kirigami patterns, prestretch, and radius selected after 100 iterations. Height-coded 2D image representations of the optimal predicted shapes: the fourth column presents the height distribution of predicted 3D topology obtained from finite element simulation using the optimal design parameters. The SSIM are approximately in 0.9. The predicted 3D shapes: the fifth column shows the predicted 3D shape in simulation. The maximum heights for the 3D images are shown in the bottom. Experimentally realized morphing 3D soft structures with desired shapes: the sixth column shows the experimental result of the 3D topology given the optimal parameters [81]

Finally, we explored asymmetric shapes like an asymmetric peanut and a butterfly Fig. 4.7, presenting unique challenges in achieving non-uniform curvatures and structural balance. These shapes required innovative adjustments to kirigami cuts to ensure that the final deformations closely matched the intended designs, pushing the boundaries of what is achievable with kirigami-based transformations.

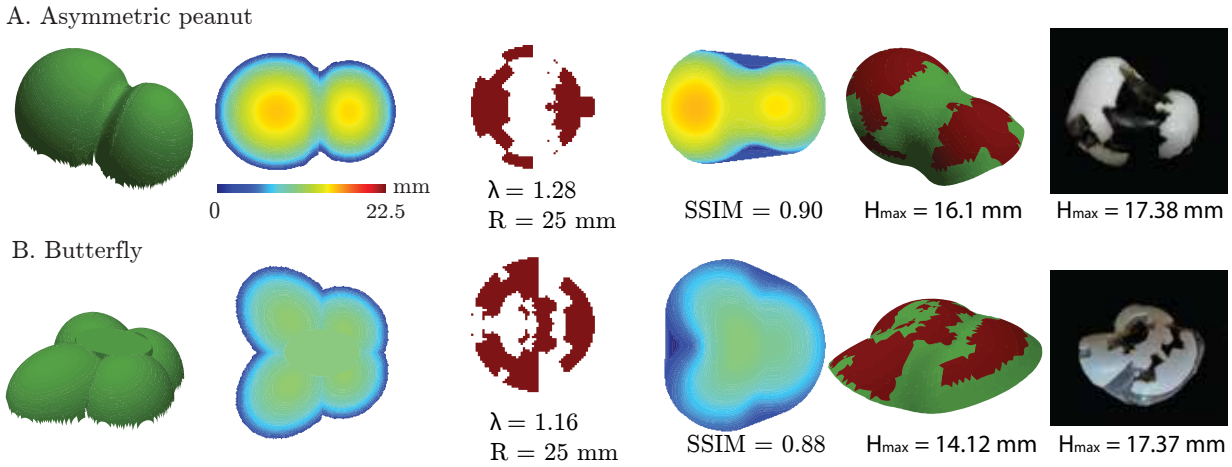

Figure 4.7: Inverse design of shapes with one axis of asymmetry: Target 3D shapes: the first column shows two different 3D shapes (A. an asymmetric peanut, B. a butterfly) input to the optimization algorithm. Height-coded 2D image representations: the second column shows distribution of height for the target 3D shape. Optimal design parameters: the third column presents the optimized kirigami patterns, prestretch, and radius selected after 100 iterations. Height-coded 2D image representations of the optimal predicted shapes: the fourth column presents the height distribution of predicted 3D topology obtained from finite element simulation using the optimal design parameters. The SSIM are approximately in 0.9. The predicted 3D shapes: the fifth column shows the predicted 3D shape in simulation. The maximum heights for the 3D images are shown in the bottom. Experimentally realized morphing 3D soft structures with desired shapes: the sixth column shows the experimental result of the 3D topology given the optimal parameters [81]

Herein, we measured the maximum height of the predictions and the manufactured shapes for preliminary comparisons. In the later section, we employ a 3D scanning technology to conduct a more detailed local comparison in the shapes between predictions and experiments.

4.6 3D Scanning and Point-by-Point Analysis

Utilizing a 3D scanner with 0.1 mm resolution, we captured the geometric details of the structures shown in Fig. 4.5,4.6 and 4.7. The scans generated a point cloud, which provided Cartesian coordinates for numerous points on each structure's surface, facilitating a quantitative analysis against our computational models.

Fig. 4.8(A) displays a side-by-side qualitative evaluation of the experimental 3D scans

(gray surface) and the computationally predicted shapes (green point clouds) for seven distinct target forms. For a more quantitative assessment, we introduced a relative error metric, δ, to measure the deviation in the z-coordinate (representing the height) of each point in the 3D scan relative to its predicted position. The formula for this metric is:

$$\delta = \frac{1}{\max\left(|z^i_{\text{scan}}|\right)} \sum_{i=1}^{N_p} \frac{\left|z^i_{\text{pred}} - z^i_{\text{scan}}\right|}{N_p},$$

where N_p denotes the total number of points in the point cloud, z^i_{scan} is the z-coordinate of the i-th point in the 3D scan, and z^i_{pred} is the z-coordinate of the corresponding point in the predicted shape. The absolute values are summed and normalized by the maximum absolute value of the z-coordinates in the scan data.

Fig. 4.8(B) illustrates this error metric across various shapes, typically remaining under 10%. The peak deviation occurs for the complex shape of a ship hull, which is still capped at at approximately 20%.

The alignment between the experimental scans and the computational predictions is noteworthy, especially considering that the simulations used a hyperelastic (Mooney-Rivlin) model, which omits time-dependent viscous deformations that occur in practice. This model, while phenomenological, provides a reasonably accurate representation of the material behavior under the experimental conditions.

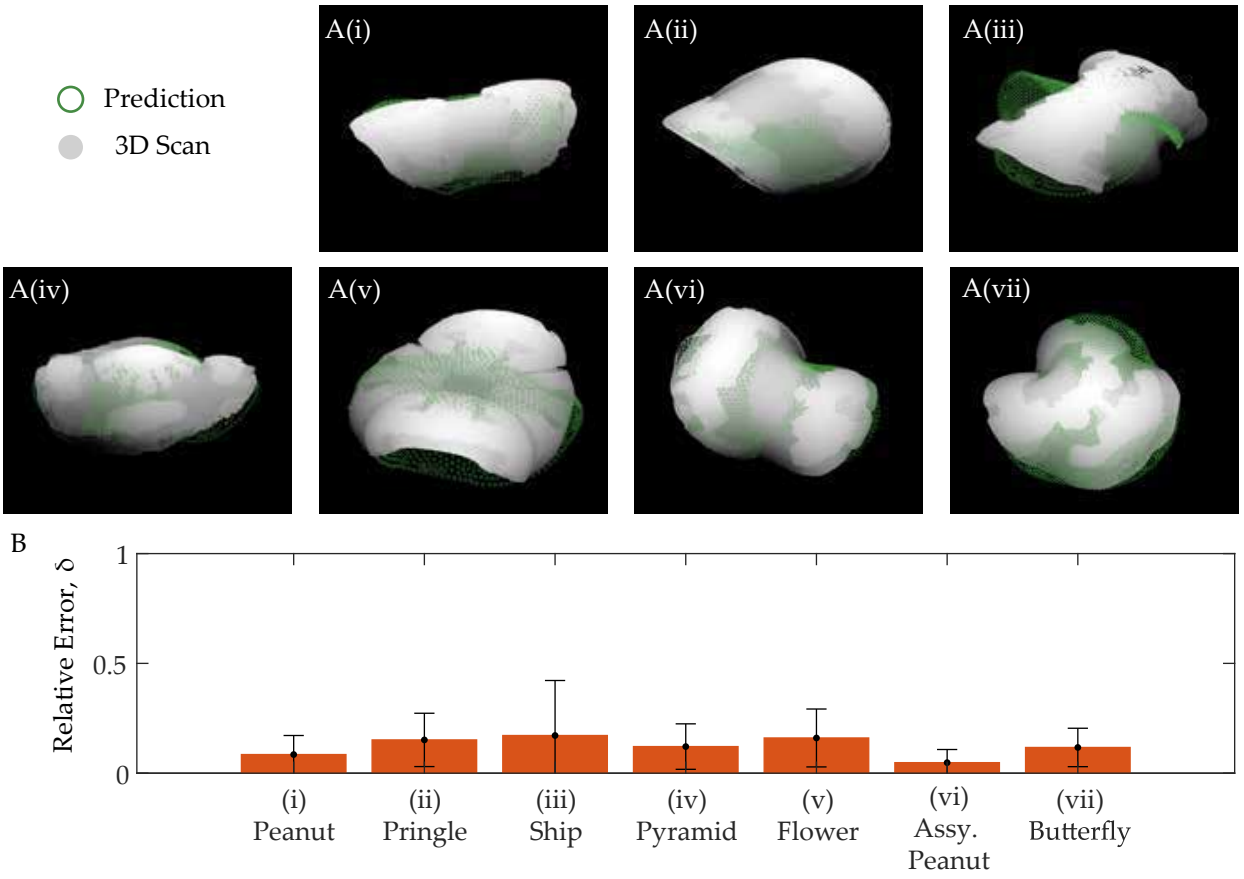

Figure 4.8: Comparison between experiments and numerical results. A) Qualitative comparison between the experimental 3D scans (gray surface) and the predicted shapes (green point cloud): (i) Peanut (ii) Pringle (iii) Ship (iv) Pyramid (v) Flower (vi) Asymmetric Peanut (vii) Butterfly. B) Quantitative comparison: The bar graph shows the relative error between experiments and numerics across various shapes considered in this paper. The error bars represent standard deviation of the error [81].

4.7 Extension to trilayer structures

The previous chapter shows that by adding additional another kirigami layer to a bilayered composite, one can create structures that attain bistability, expanding their potential applications. In this section, we want to test whether we can achieve similar targeted 3D bistable structures just by modifying the size and the amount of pre-stretch while keeping the optimized kirigami patterns the same as the bilayered counterparts. To achieve this goal, we make use of the scaling analysis derived from analytical formulation in Sec. 3.6

The 3D shapes we focus on in this section are previously discussed examples throughout this research. Fig. 4.9 shows the kirigami patterns in the first column can be used to create a target structures in the second column using bilayered kirigami composites. For these 3D shapes, we can assume the curvature is approximately the same everywhere. In this case, the relationship between the initial size and height is derived in Sec. 3.6. Then, the normalized height H/L can be approximated by using Eq. 3.14

So we see, for the structure of a certain radius R, the bending stiffness D_eq for the trilayer Eq. 3.7 is about 3 times of the bilayer counterpart Eq. 3.9. Moreover, the material constants for the kirigami layer leading to unilobe structures are C_{kg1} and C_{kg2} (gray kirigami), while the constants for kirigami that creates the bilobe shape are C_{kw1} and C_{kw2} (white kirigami) (Table 3.1). This indicates the increase in the overall stiffness of the structure.

Now, if we apply the same amount of pre-stretch to the trilayer structure of the same size as the bilayer counterpart, then the free-buckling shape is still flat in the plane as shown in Fig. 4.9. This is due to the increased stiffness in the system. To create the targeted 3D shapes of similar height ratio H/L, the pre-stretch and size simply need to be adjusted according to Eq. 3.14. The last column in Fig. 4.9 shows when the pre-stretch varies near the value for the bilayer counterpart, but the radius of the structure is increased, we can still fabricate shapes of similar H/L using these trilayer composite structures.

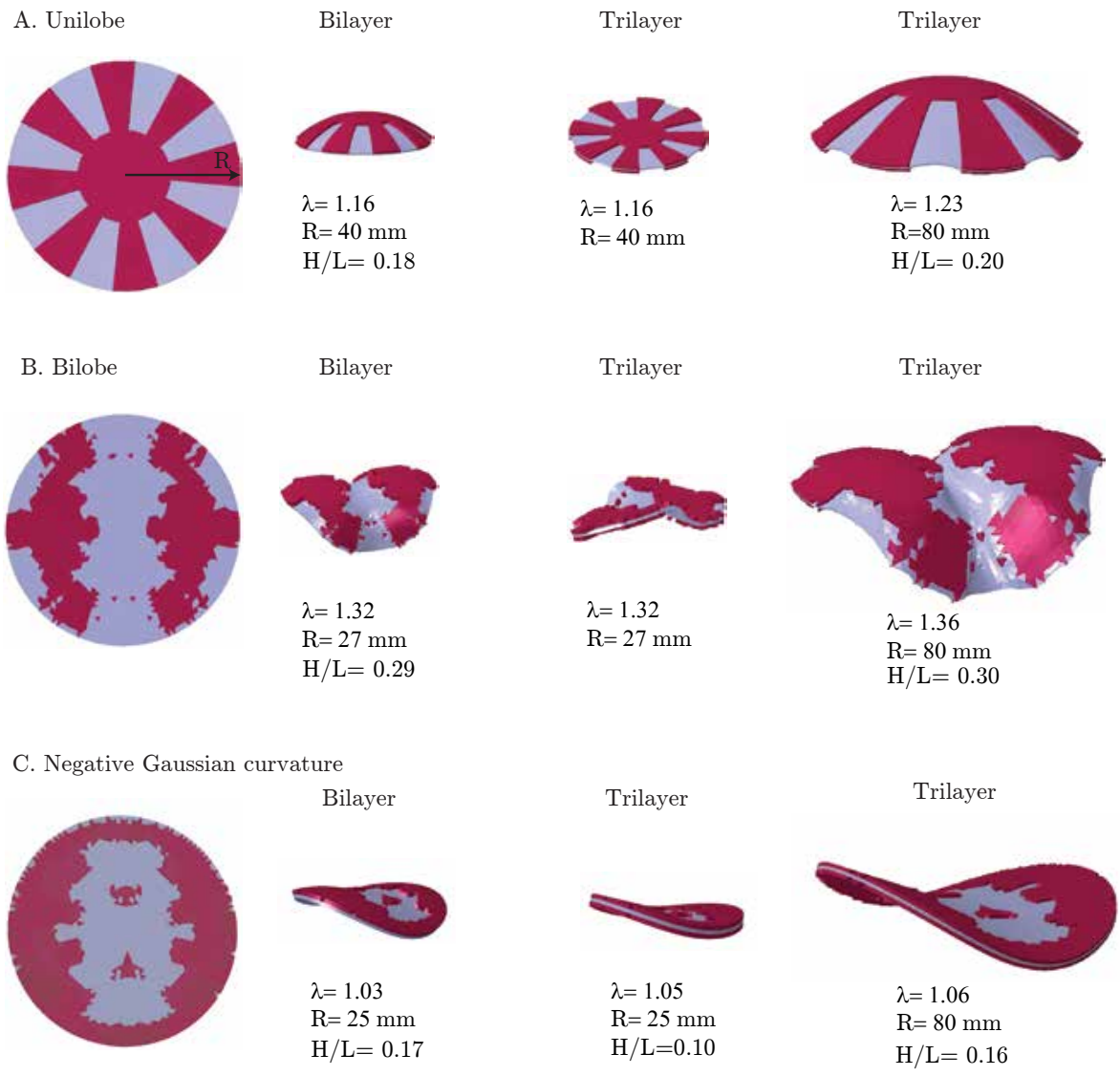

Figure 4.9: Comparison of the free buckling shape for bilayer and trilayer soft kirigami composite. The kirigami patterns is fixed, and the structures can create three target shapes (A) Unilobe structure. (B) Bilobe structure. (C) Structure with negative Gaussian curvature. First column: kirigami patterns in red and circular substrate in blue. Second column: Bilayer structure with specific combination of pre-stretch and initial radius. Third column: Trilayer structure with the same combination of pre-stretch and initial radius as the bilayer counterpart. Fourth column: Trilayer structure with adjusted pre-stretch and radius [81].

Thus, we have successfully extended this inverse design algorthm to design bistable soft kirigami structures using the same kirigami designs and other modified design parameters.

4.8 Conclusion

In conclusion, this part of the research has successfully illustrated the application of an inverse design algorithm to precisely tailor kirigami deployables to any specified target shape. By leveraging advanced machine learning techniques, notably VAEs and active learning, the methodology not only enhances the precision of our designs but also significantly accelerates the process, allowing for rapid prototyping and optimization of complex three-dimensional shapes. The congruence between the computational predictions and actual fabrications underscores the efficacy of this approach, offering a robust solution to the inverse design problem in soft kirigami deployables. Furthermore, it not only can predict design parameters for mono-stable kirigami shapes but can also be extended to trilayered bistable structures. This enables us create any target shape depending on the application by using the planar fabrication techniques of soft kirigami composites.

CHAPTER 5

Shrinky Dink based Kirigami Deployables

5.1 Motivation

The development of deployable structures often involves complex and costly processes, which may require the assembly of multiple rigid components or the utilization of sophisticated materials. Looking out our previous research in this field, though we have achieved the creation of pre-programmed deployables through a single flexible composite, the fabrication frequently demands specialized manufacturing equipment (such as laser cutters and linear stages), which can be expensive and challenging to acquire. Addressing these limitations, we further present an innovative series of deployable structures that streamline both design and production [84].

These deployables are similarly designed with "embedded instructions" within their kirigami based composition, dictating the specific three-dimensional configuration they should adopt upon deployment very similar to those in nature Fig. 5.1(A). However, an essential advancement of the structures is their production methodology, which is both intuitive and inexpensive. The techniques employed are accessible, using straightforward processes and equipment that are both cost-effective and widely available. This approach ensures that the benefits of advanced deployable structures can be realized more broadly, extending beyond high-tech environments to more resource-limited settings.

Furthermore, it is interesting to note that the deployables outlined so far in this thesis instantaneously assume their three-dimensional shape upon release of the planar design. However, real-world applications of deployables often necessitate precise deployment control. The structures developed herein also incorporate a mechanism for 'at-will' deployment. This

capability allows the structures to be stored indefinitely in a compact form and deployed precisely when required, combining convenience with functional adaptability.

In summary, this set of deployable structures not only feature embedded deployment instructions but also are simple and economical to produce with flexibility of controlled deployment timing. To do so, they employ the stimulus of environmental temperature change to switch forms from planar to 3D Fig. 5.1(B). These innovations hold significant potential for a wide array of applications, providing a practical solution that addresses the traditional complexities and costs associated with deployable structures. Fig. 5.1(C) displays a few such practical applications such as a soup spoon and bowl set and a functional mouse cover.

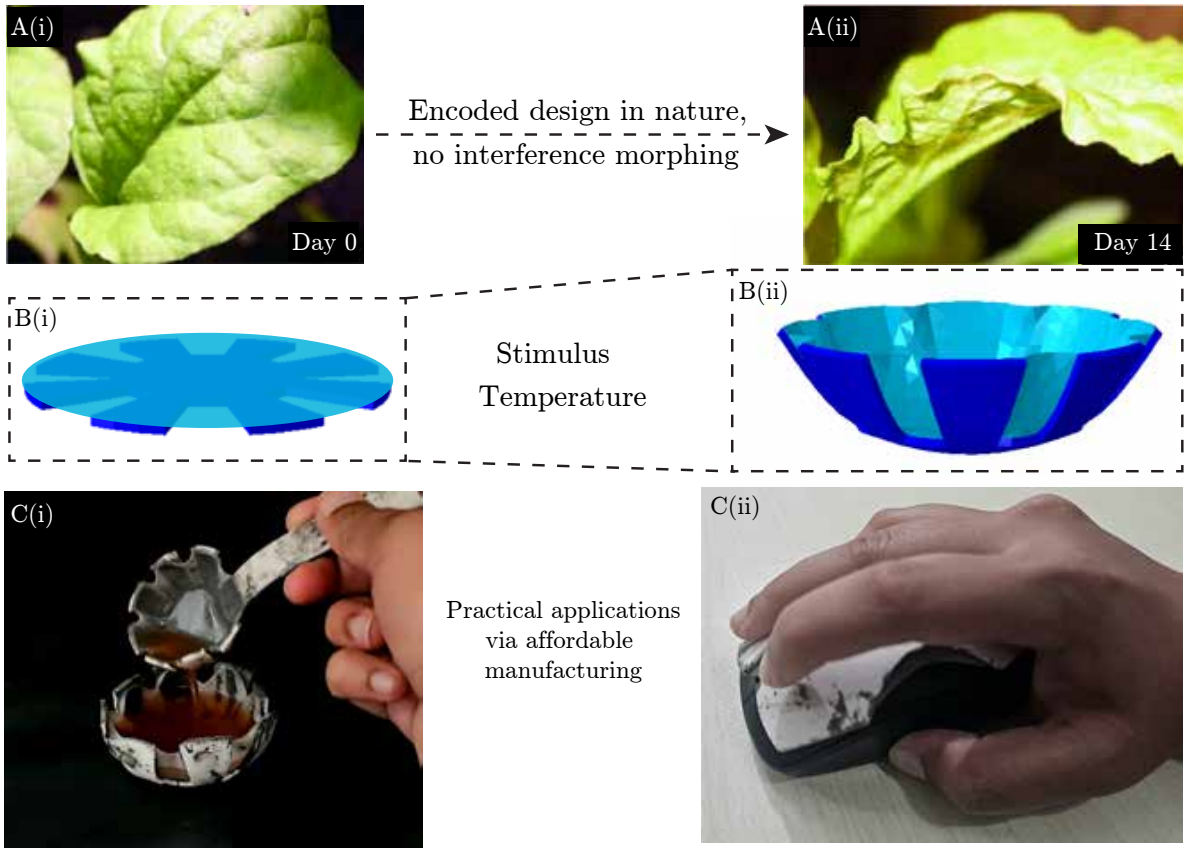

Figure 5.1: Introduction to Kirigami-Enhanced Shrinky Dink 3D Morphing A(i-ii) Nature portrays no-interference, growth-based morphology in various organisms (Images reproduced with permission from Sharon et.al. [5]) B(i-ii) The Shrinky Dink deployables mimic this process to morph from one form to other without design interference. C Using this technology, one can simply use easily available equipment to create practical objects such as (i) Soup bowl and spoon (ii) Functional mouse cover [84]

5.2 Methodology

Here, we capitalized on the well-known temperature-sensitive behavior of Shrinky Dinks. These materials dramatically shrink in their lateral dimensions and thicken when heated, typically reducing to about one-third of their original size. Traditionally, they're used to crafting compact and sturdy items like keychains and jewelry, often decorated with hand-drawn or printed designs. We took a new approach—instead of applying ink directly to the Shrinky Dink surface, we attached 3D printed elements to it, creating what we call a "Shrinkle" composite. This setup takes advantage of the Shrinky Dinks' natural tendency to contract with heat. The addition of the 3D printed parts helps to counterbalance this contraction, resulting in an interesting stress-induced buckling that transforms the composite into a three-dimensional shape.

We then moved on to refine the control over the final shapes of our composites by using the kirigami deployable technique. Instead of using random patterns, we specifically designed and 3D printed tailored kirigami patterns onto the Shrinky Dinks. This allowed us to direct the final three-dimensional form that emerges during the heating process. By strategically incorporating these kirigami designs, we were able to achieve pre-defined, intricate three-dimensional structures, all while harnessing the creative potential of 3D printing technology. By carefully choosing our kirigami patterns and meticulously managing other geometric variables, we opened up possibilities for producing a diverse range of distinct three-dimensional shapes. The technique has be described in Fig. 5.2. Furthermore, in an advancement beyond the kirigami deployables, these structures do not automatically assume a 3D form upon release of the design. Instead, they can be activated to transform into their three-dimensional shape precisely when needed by simply heating them at the desired moment.

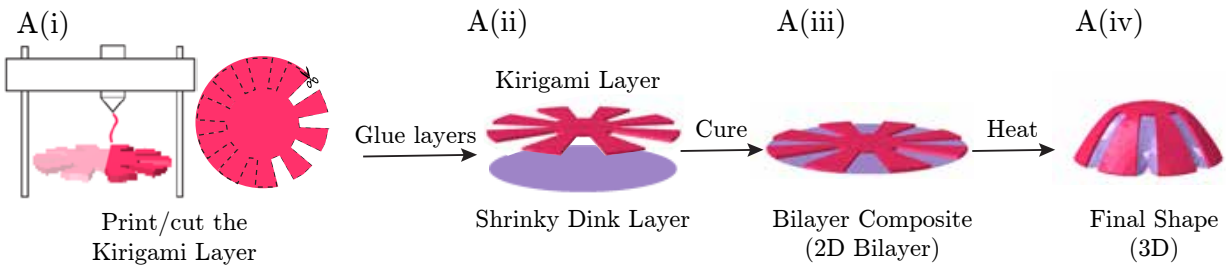

Figure 5.2: Schematic of the Shrinky Dink deployable method: Start by designing a kirigami pattern. Adhere it firmly with a Shrinky Dink sheet to create a Shrinkle composite. When ready, heat the composite, to deploy it to the 3D shape [84]

5.3 Experimental Method

In the production of a Shrinkle composite and subsequent three-dimensional shapes, our process begins with the 3D printing of a carefully chosen kirigami design Fig. 5.3(A(i)). For this explanation, we selected a lotus-shape kirigami design with a circular shaped Shrinky Dink substrate aimed at achieving a 3D bowl shape. We chose ABS filament for its excellent durability and heat resistance properties. After completing the 3D printing, we enhance the adherence capabilities of one side of the print. To achieve this, we gently roughen the surface using either sandpaper or a hand file, ensuring an optimal bonding surface.

Next, we take a piece of Shrinky Dink sheet and precisely cut it into the desired shape. For this design, we use a circular piece of Shrinky Dink, which aligns with the final 3D structure's requirements. Once the Shrinky Dink material is prepared in the necessary shape, we roughen one side, mirroring the preparation done on the 3D printed piece. Before the crucial bonding step, we diligently clean the work surfaces with 99 percent isopropyl alcohol, ensuring a debris-free environment for effective adhesion.

With both the 3D printed piece and the pre-cut, prepped Shrinky Dink sheet ready, we move to the bonding stage. We apply a thin layer of epoxy glue to the roughened surface of the 3D printed component and carefully position it onto the pre-cut Shrinky Dink substrate Fig. 5.3(A(ii)). We use the JB Weld steel epoxy for this process for a few reasons. Firstly, this glue is strong, heat resistant at the required temperature and easily and economically

available online and in-store. Secondly, the gray color of this glue is beneficial to ensure that the entire surface is uniformly coated with the glue. However, this might aesthetically leave back glue patches over the kirigami surface visible in experimental pictures throughout this research, but these can be simply covered by paint without affecting the final shape. For the curing process, the composite is then placed under a substantial load for at least 48 hours to ensure that the glue spreads evenly and the two layers adhere firmly, securing a robust bond. This setup guarantees not only the strength of the bond but also uniformity across the joined surfaces.

Once cured, this composite can be stored indefinitely and deployed at any desired time without requiring immediate activation.

To deploy the composite to its 3D shape Fig. 5.3(A(iv)), it is subjected to heat upon completion of the curing period Fig. 5.3(A(iii)). We preheat an oven to 270°F, opting for a temperature slightly below the usual range of 300-325°F recommended for Shrinky Dink toys. This lower temperature is chosen deliberately to slow the contraction process, allowing for greater control over the buckling phenomenon that occurs during heating. Typically, the specific structures we create require about 1-2 minutes in the oven to fully assume their three-dimensional form, although the exact duration can vary depending on the initial design parameters. Also, the composite is placed in the oven Shrinky side down so that the weight of the kirigami layer forces a slow, uniform deformation of the composite.

The process uses a cost-effective setup, employing a basic home 3D printer for the printing steps, acquiring Shrinky Dink sheets from easily accessible e-commerce platforms like relying on readily available JB Weld steel epoxy for bonding. The transition from a 2D composite to a 3D structure can be accomplished using a standard domestic oven, which is common in most households. Although such ovens do not offer precise temperature control, with noticeable fluctuations especially when opening or closing the oven door, the Shrinky Dink material still deforms effectively at the adjusted temperature. We document these temperature fluctuations to provide a detailed understanding of the entire process, ensuring that our research captures all variables that impact the transformation of the composite into its final three-dimensional shape.

Additionally, supporting tools such as alcohol, sandpaper, scissors, and other common supplies are both cost-effective and widely accessible, further emphasizing the accessibility and simplicity of this innovative manufacturing method for a broad audience of enthusiasts and researchers alike. This carefully orchestrated and straightforward manufacturing process allows us to craft a diverse array of precisely engineered three-dimensional structures, as detailed in the subsequent sections of this study.

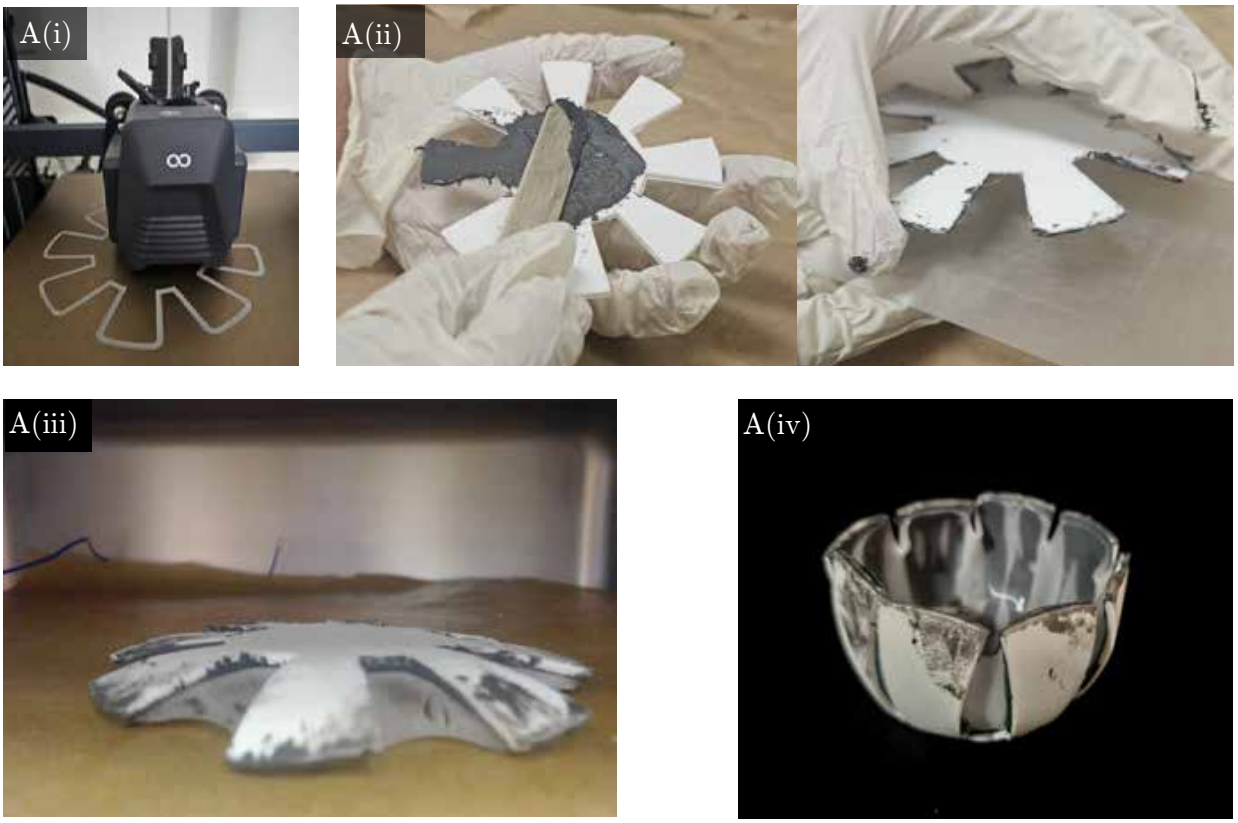

Figure 5.3: Experimental process to manufacture Shrinky Dink deployables A(i) Cut or 3D print a kirigami design A(ii) Glue it firmly to a Shrinky Dink layer of suitable shape A(iii) When cured, heat the composite in the oven at home A(iv) The final shape of the composite [84]

5.4 Temperature Logging

Since, we use a domestic oven for this experiment, it is a challenge to maintain the exact temperature throughout the experiment. This combined with the non-uniform, unpredictable

deformation of the Shrinky Dink sheet can lead to varying final results based on the temperature variation throughout the process and the total time of heating. Thus, throughout each experimental run, we record the temperature fluctuation with respect to time. This gives anyone who potentially recreates the experiment an idea of the fluctuations in the design parameters.

We start the logging when the composite is placed in the oven. Next, we note the first moment of visible deformation in the Shrinky Dink to pinpoint the exact start of the process. The temperature variation is then recorded over the whole duration of the deformation until the composite is removed from the oven. The temperature log for an hemispherical bowl shape studied later has been presented in Fig. 5.4

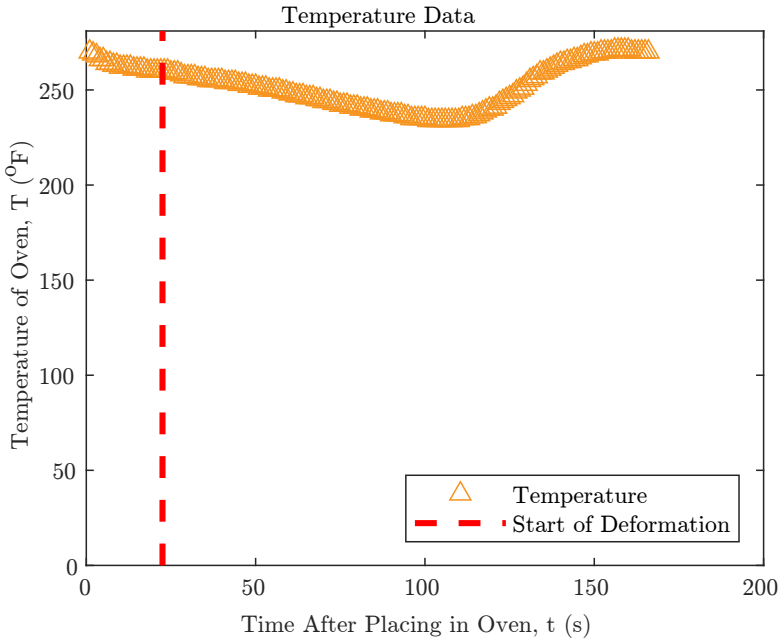

Figure 5.4: This represents the temperature log portraying the fluctuation of temperature over the entire deformation process. It also displays the start time of the deformation [84]

5.5 Material Modelling

To comprehensively analyze these structures, we require material properties such as Young's modulus and Poisson's ratio. Additionally, due to the nature of the deformation, the ther-

mal coefficients of the materials involved are also necessary. Thus, material modeling in our study is a two-stage process. Initially, akin to our previous methods, we employ an ASTM D412 sample and conduct tensile testing on both the 3D printed kirigami and the commercially purchased Shrinky Dink. For the kirigami, we print a sample using the same parameters as in our experiments, maintaining a thickness of 1.8 mm, which is commonly used in creating various shapes in the process. Despite obtaining non-linear stress-strain curves from our tests, we employ a linear material approximation to simplify the complexity of our simulations. This choice is driven by the limitations of our simulation tools and the deformation characteristics of the materials.

Specifically, the Shrinky Dink layer exhibits orthotropic deformation when subjected to temperature changes. However, ABAQUS, the software we use for numerical simulations, does not accommodate the complex hyperelastic materials typically necessary for accurately modeling orthotropic deformations. As a result, we opt to apply a linear material model for both layers in the composite to ensure compatibility with our simulation capabilities. To derive this linear approximation, we equate the area under the stress-strain curve to the strain energy obtained via a linear model given by $\frac{1}{2}E\epsilon^2$, where E is Young's modulus, and ϵ is the strain. The stress-strain responses of the two materials are shown in Fig. 5.5(A). We also assumed a fully plastic material, leading to a value of $\nu = 0.5$. We used these approximated values of Young's modulus for the remainder of our numerical simulations.

The next phase of material modeling involves determining the thermal coefficients of the two materials. We prepared 3 cm x 3 cm specimens of both materials and placed them in the oven. As expected, the Shrinky Dink contracted across its area and expanded in the out-of-plane direction. The 3D printed piece, due to its intricate crisscross infill pattern, contracted slightly in all three dimensions. We noted the values of the initial and final lengths shown in Fig. 5.5(B) and the fixed temperature difference. This process allowed us to determine the thermal coefficients of the materials as well. All material properties have been detailed in Table 5.1. Equipped with this information, we proceeded to formulate the numerical simulations for analyzing these composites.

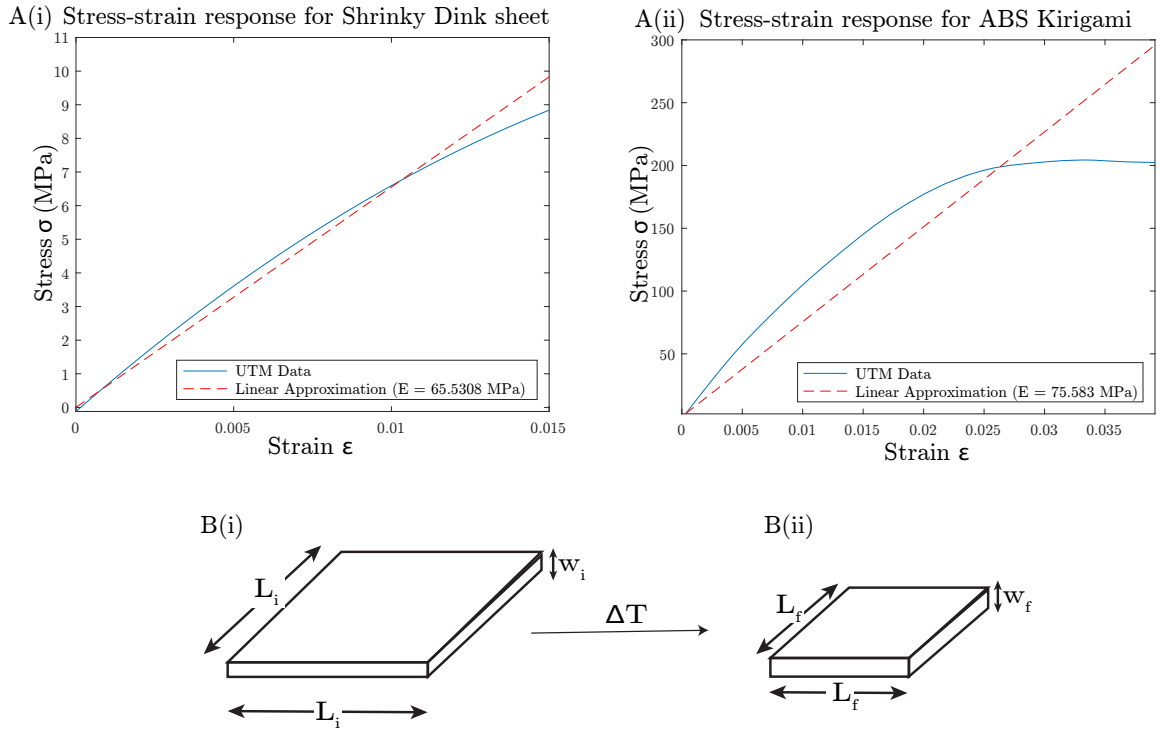

Figure 5.5: This represents the material modelings of the involved materials: (A(i))Stress strain response of the Shrinky Dink sheet (A(ii))Stress strain response of the ABS layer (B) Thermal contraction of a designated square piece of each material on placing in an oven [84]

Parameter	Value	Unit
Young's Modulus E^s	655	MPa
Thermal Coefficient α^s	-0.005	K^{-1}
Thickness t^s	0.1	mm
Young's Modulus E^k	755	MPa
Thermal Coefficient α^k	-0.0001	K^{-1}
Thickness t^k	1.8	mm

Table 5.1: The approximate linear material parameters for the two different materials used (1) Shrinky Dink (2) Kirigami (ABS)

5.6 Numerical Simulation

The numerical simulations for these structures are carried out in ABAQUS with crucial modifications to accommodate the specific deployment mechanisms and material behaviors

of the composites. A significant change from previous kirigami deployable simulations is the shift from pre-stretch based deformation to temperature-based deformation. This adjustment is essential because, unlike traditional methods that utilize pre-stretching, the deployment of these composites is driven by temperature changes.

To accurately simulate the temperature-induced deployment, the simulations must account for the orthotropic nature of the Shrinky Dink's thermal contraction. Therefore, the setup begins with defining the kirigami and Shrinky Dink patterns in MATLAB and ABAQUS, similar to previous simulations. The central node is fixed and designated as the origin of the coordinate system. Two nodes are strategically placed along the X and Y axes, a short distance from the center, to assist in defining the plane. Additionally, a node in a layer above the bottom layer is selected to define the Z axis. These nodes, along with the central origin node, establish the orthotropic coordinate system necessary for modeling the specific directional properties of the Shrinky Dink's contraction.

The complexity and partially unknown properties of the materials involved lead to simulations that primarily offer qualitative insights into the deformation behavior. The thin glue layer between the kirigami and Shrinky Dink layers is omitted from the simulation in the present. Due to the complicated nature of the materials and the various simplifying assumptions made at the material modeling level, the simulation has to be run for a modified ratio of bending stiffnesses (β_E) and difference between the thermal coefficients (δ_α) of the two involved materials. Also, currently within the confines of the ABAQUS meshing, the code requires a lower deformation for convergence to be reached.Thus, presently, the values used herewith employ a heuristically reduced δ_α while keeping the rest consistent with the experiments.

Thus far, the simulation is run for the hemispherical bowl shape as it is one of the fundamental shapes for the research. This simulation aids in getting a qualitative idea of the parametric variation as is portrayed in later section. However, it still falls short quantitatively as the reduced δ_α leads to underestimation of the deformation. The upcoming manuscript on this research aims to resolve this issue by further modifying the ABAQUS simulation and material parameters (β_E and δ_α) to achieve values close to the ones in the experiments.

This would have to be done by compensating for the material modeling insufficiency by working within the simulation software capabilities. Once, this has been achieved, simply by replacing the meshes, the simulation would be extended to the different shapes involved in this research. In the future, with advancements in machine-learning-based material and numerical modeling, as discussed in previous chapters, this methodology could serve as a significant step toward fully understanding these deployable composites.

5.7 Variation of Shapes

We have the capability to shape the final 3D structure by adjusting the designs of the individual layers within the composite, particularly the 3D printed part and the Shrinky Dink sheet. Addressing the inverse design challenge for these configurations is an ongoing effort, but we have identified three approaches that help predict the initial design parameters needed to achieve the desired 3D end shape. This section explores these strategies, enhancing our ability to craft custom 3D shapes using the straightforward experimental methods we've detailed earlier.

5.7.1 Heuristic understanding

Inspired by previous research in kirigami deployables, our initial exploration involved creating a 3D hemispherical bowl Fig. 5.6(A) from a lotus-shaped kirigami [14]. We utilized a lotus-shaped design petals, which produced the depicted bowl. We also crafted a simple pyramid shape [85] Fig. 5.6(B) using an appropriate kirigami-Shrinky Dink combination. These primary forms are crucial for understanding and subsequently developing more intricate 3D models in later.

Additionally, by studying familiar shapes, we sought to replicate them through our techniques. Drawing from seashell contours, we could design a seashell 3D shape from this methodology as well Fig. 5.6(C). Moving beyond basic shapes like hemispherical bowls, we replicated the upper cover of a computer mouse Fig. 5.6(D) by analyzing a standard mouse's dimensions and creating a custom kirigami piece to achieve the necessary bi-axial curva-

ture. A strategic separation was designed between the mouse cover's key areas to facilitate individual clicking actions, demonstrating the method's simplicity and cost-effectiveness in producing practical shapes.

5.7.2 Machine Learning assisted understanding

It is ideal to reproduce any desired 3D shape using this method, requiring us to solve the inverse design problem. Though addressing this complex challenge remains a thing of the future, we can extend existing inverse design solutions to this technique. Herein, we present structures created using the designs predicted in our previous work [81] using the Shrinky Dink methodology.

But even though we share many basic design principles with these approaches, uncertainties about size and temperature adjustments remain. The increased rigidity of the material layers used in our experiments means many kirigami designs need alterations to form meaningful shapes.

In this context, we introduce some shapes to further explore this expansion of the inverse design problem. We begin with a peanut shape, using the predicted kirigami design with minor size adjustments, as illustrated in the Fig. 5.7(A). However, trying to reproduce a four-petal flower proved the design from previous inverse solutions inadequate due to the material's increased flexural rigidity, which only allows for a single fold instead of the needed two folds. Yet, through intelligent design tweaking to the predicted flower kirigami pattern and via heuristic insights, we successfully create an attractive butterfly 3D shape using the Shrinky Dink methodology Fig. 5.7(B). While current machine learning tools may not fully encompass this new methodology, many shapes can be replicated without modifications, and others can provide delightful alternatives with minor tweaks.

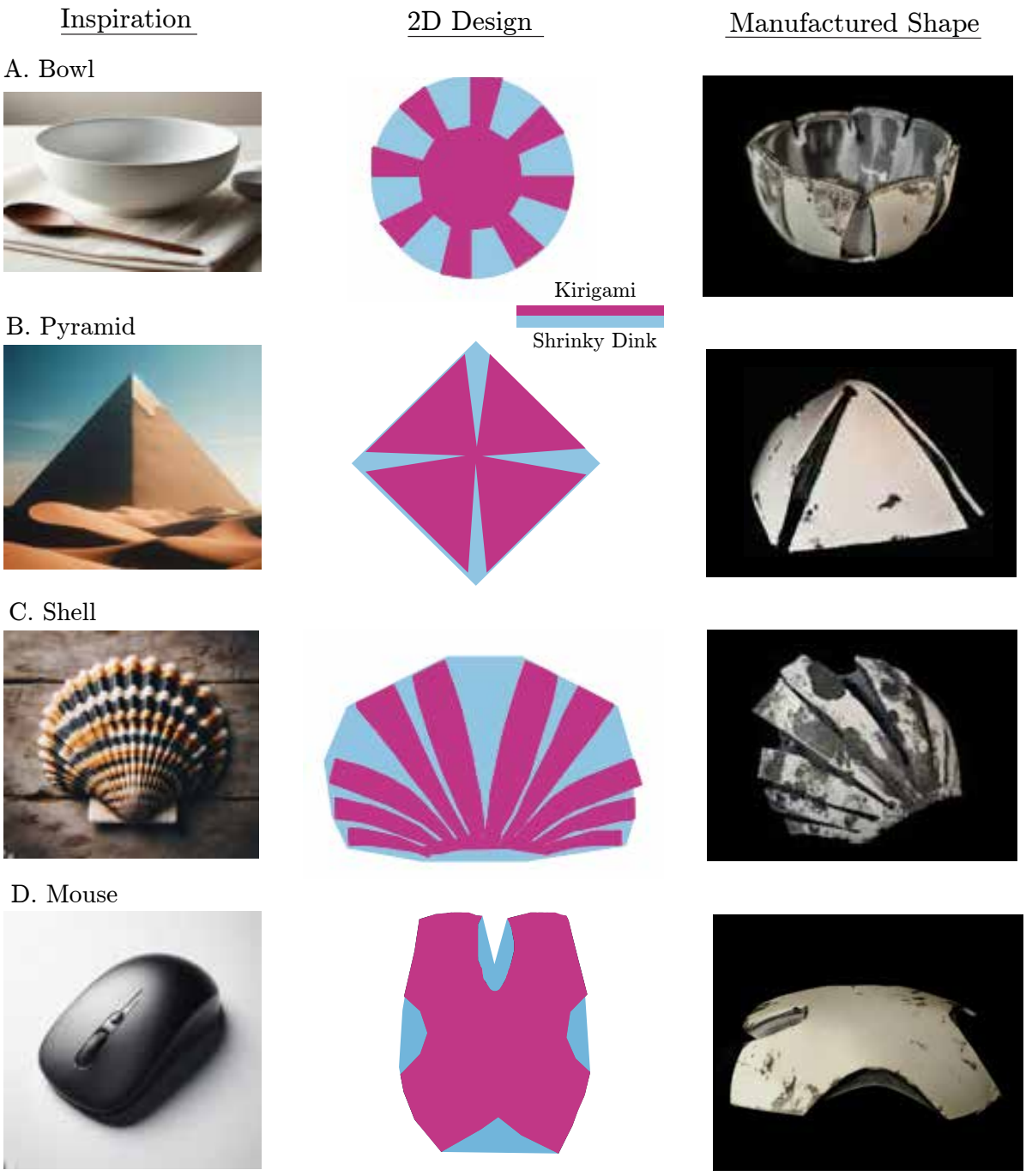

Figure 5.6: This represents the creation of the Shrinky Dink deployables through heuristic designs: (A) a hemispherical bowl, (B) a pyramid, (C) a shell and, (D) a mouse cover. The first column shows the inspiration [86] behind creating the shape, the second column shows the kirigami and Shrinky Dink shapes used to manufacture it and the third column displays the final manufactured shape [84]

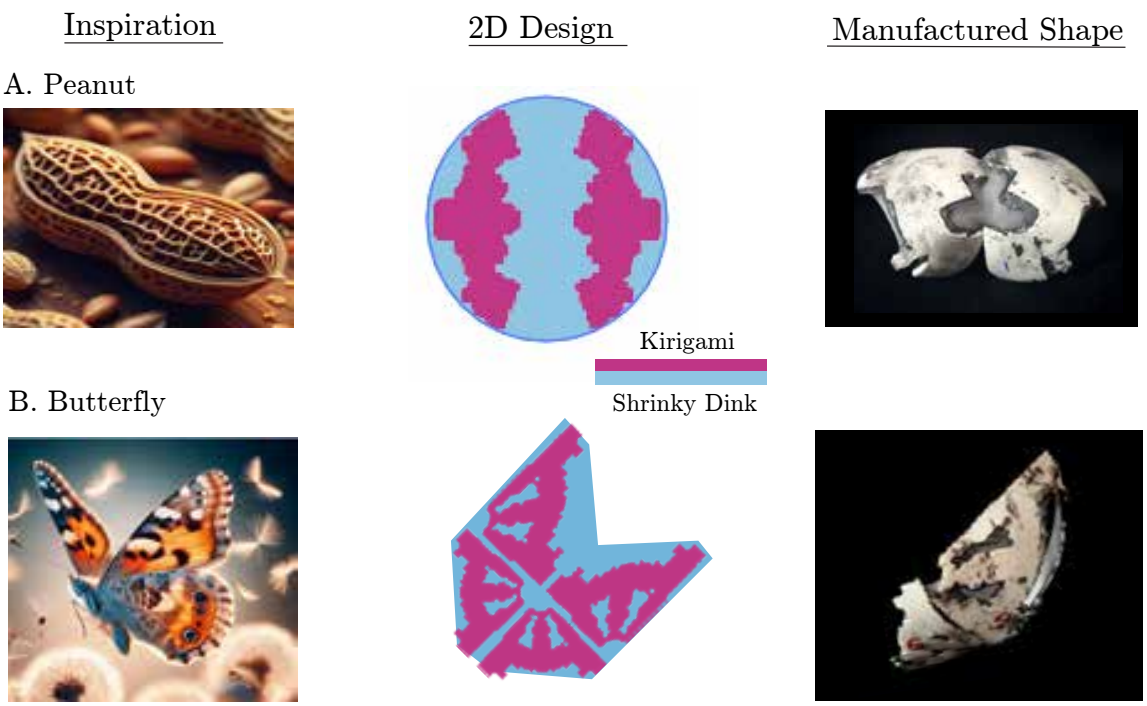

Figure 5.7: This represents the creation of the Shrinky Dink deployables using the inverse algorithm [81]: (A) a peanut and, (B) a butterfly. The first column shows the inspiration [86] behind creating the shape, the second column shows the kirigami and Shrinky Dink shapes used to manufacture it and the third column displays the final manufactured shape [84]

5.7.3 Combination of Existing Shapes

With a range of design-shape combinations at our disposal, we are now positioned to construct more complex 3D structures. This process involves merging two basic designs into a new kirigami configuration, with meticulous observation and fine-tuning to ensure a smooth transition between the two designs. To do so, rather than using a single continuous Shrinky Dink cutout, we attach separate Shrinky Dink pieces to each side of the kirigami, ensuring a flawless curvature transition as shown in Fig. 5.8(A). For example, consider the task of creating a soup spoon, which requires a curved hemisphere at one end, a shape we have previously developed and a simple bimaterial curved arch. To fabricate the spoon, we create a new kirigami pattern incorporating these two existing designs into one Fig. 5.8(B(i)) with three layers in the composite. Upon heating, this composite assembly takes on a spoon-like 3D form. Similarly, we create a similar axisymmetric shape, a rimmed soup bowl by

carefully placing the Shrinky Dink and kirigami layers Fig. 5.8(B(ii)). Equipped with multiple heuristic shapes and designs derived from previous algorithms, we can explore various combinations to craft an even broader array of complex shapes.

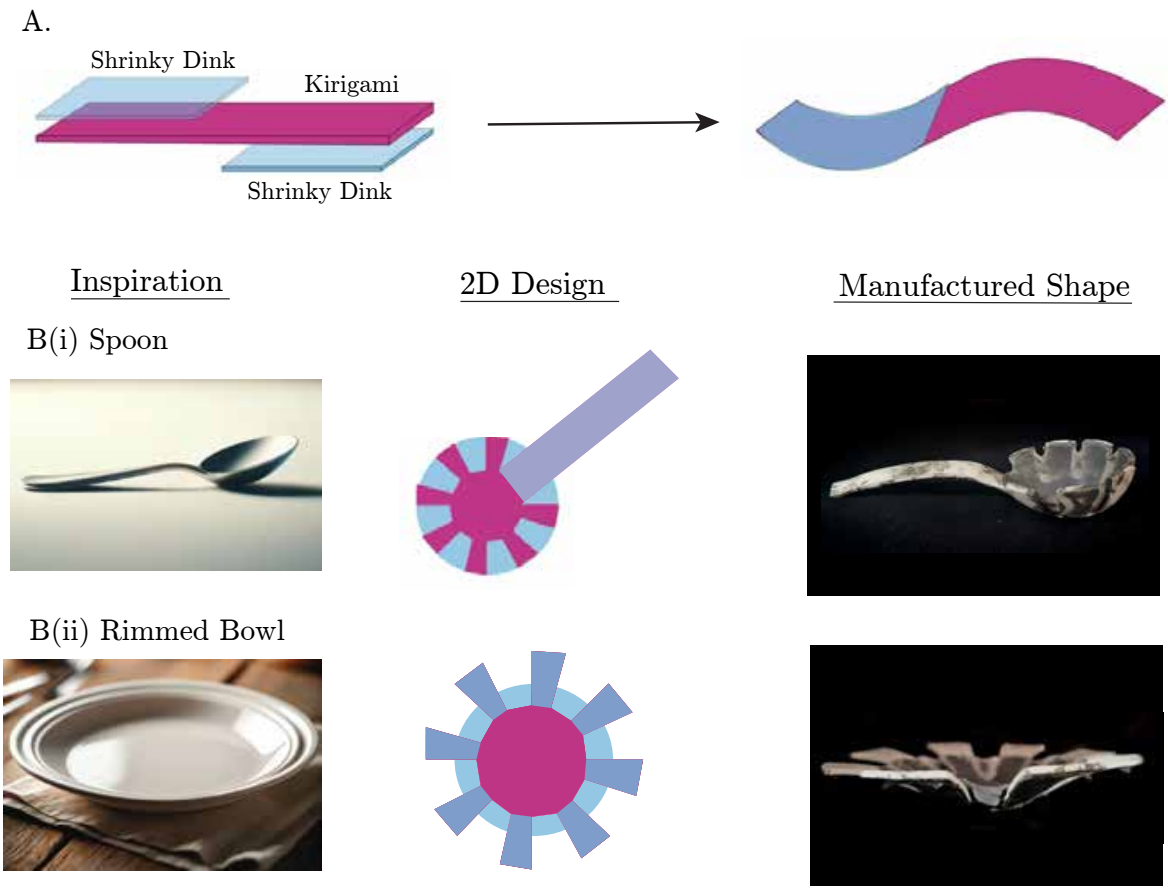

Figure 5.8: This represents the creation of the Shrinky Dink deployables through combination of existing shapes: (A) The positioning of the Shrinky Dink and kirigami layers to create a shape with a smoothly changing curvature. (B) The first column shows the inspiration [86] behind creating the shape, the second column shows the kirigami and Shrinky Dink shapes used to manufacture it and the third column displays the final manufactured shape (i) a spoon (ii) a rimmed bowl

5.8 Parametric Variation

We conduct a study to understand the variation of the final 3D shape based on the initial parameters. For this purpose, we use the hemispherical bowl shape as a basis for comparison. We maintain consistent parameters, such as the outer radius and thickness of the circular

foundation in the kirigami design, as shown in Fig. 5.9(A(i)). To examine the effect of changes in the kirigami design on the final 3D shape, mainly the final height shown in Fig. 5.9(A(i)), we vary the amount of material removed. Specifically, we use the same kirigami design with 8 equally spaced petals and alter the radius ratio ($\gamma = r/R$) between the inner radius (r) and the outer radius (R).

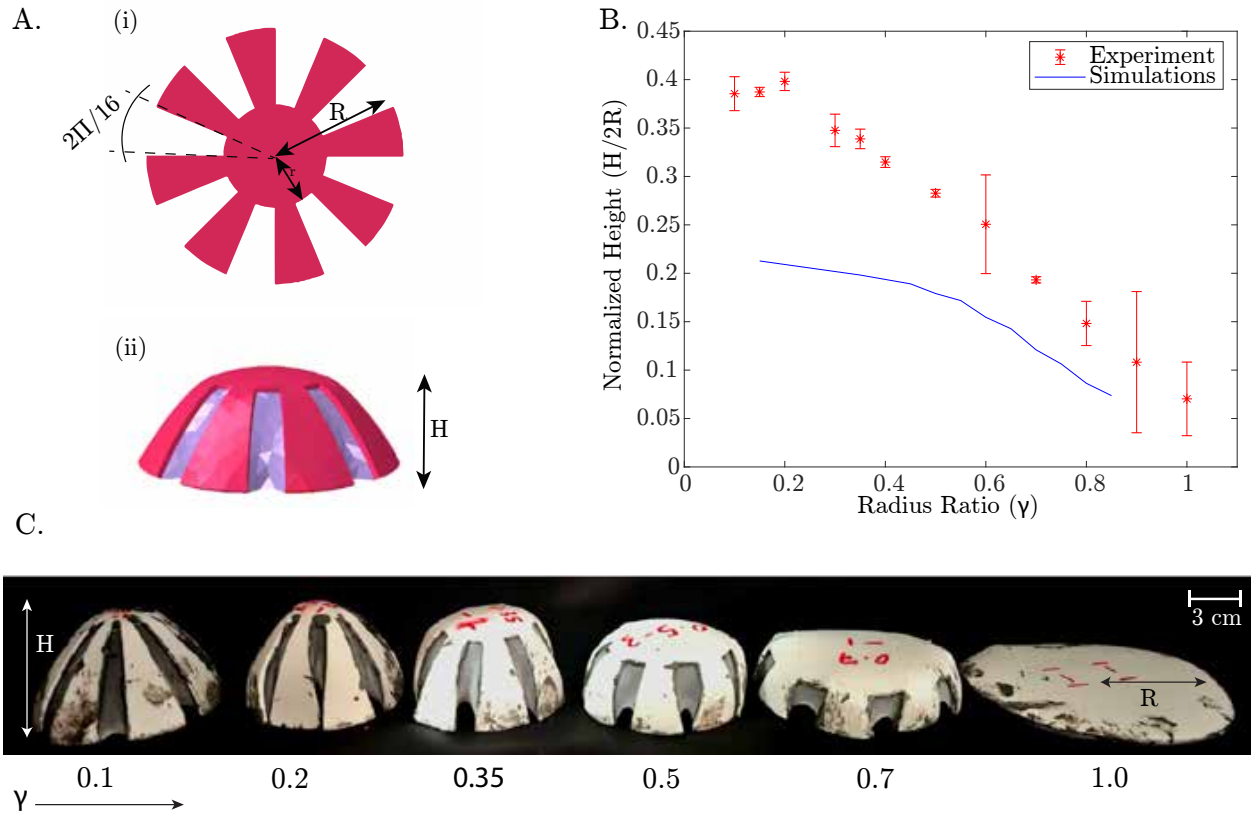

Figure 5.9: Variation of the 3D shape with change in radius ratio (A) A sketch of the various dimensions used in the parametric variation in (i) planar form (ii) 3D shape (obtained via simulations) (B) A graph portraying the experimental and the numerical variation of height with respect to radius ratio γ (C) Variation of height in experimental specimens with change in γ [84]

We vary γ to study its impact on the final height of the structure. Our findings indicate that the normalized height (H/2R) decreases as γ increases from 0.2 to 1. This occurs because when less material is removed from the kirigami layer, the Shrinky Dink layer has more freedom to deform, leading to greater buckling of the composite structure. Fig. 5.9(B) illustrates this trend in both simulations and experiments.

Furthermore, Fig. 5.9(C) shows the experimental photos of the parametric variation. This visually agrees with the trend portrayed in the previous graph.

CHAPTER 6

Conclusions

In conclusion, the development and exploration of deployable or shape-morphing structures presented in this thesis are poised to significantly influence various engineering domains and beyond. By drawing inspiration from biological systems and embedding instructions for morphing directly within the materials, we revolutionize the traditional perspective on the growth and transformation of structures. This innovation not only enhances the functionality of deployable structures but also their adaptability across multiple applications.

Our work introduces multistability in deployable structures, which further broadens their applicability in critical fields such as medicine, robotics, and architecture. These multistable systems, capable of maintaining various stable configurations without continuous external energy, are a substantial advancement towards more practical and versatile applications.

Moreover, by integrating machine learning with insights from mechanics, this research stands at the forefront of the field, offering a novel method to design deployable structures from scratch. This machine learning algorithm allows for the efficient design of structures based on required target shapes, optimizing both the structural integrity and functional efficacy.

Additionally, the development of an equipment-frugal methodology democratizes the manufacturing of deployable structures, making this technology more accessible and feasible for broader applications. This approach not only simplifies the manufacturing process but also enhances the understanding and capabilities of deployable systems, fostering innovation in creating more complex structures through simpler components and methods.

Through this research, we pave the way for future advancements that could potentially transform the landscape of deployable structural design, embodying the principles of growth,

adaptation, and functionality inspired by nature.

Bibliography

[1] B. L. Hogan, "Morphogenesis," *Cell*, vol. 96, no. 2, pp. 225–233, 1999.

[2] M. Baguma-Nibasheka and B. Kablar, "Mechanics of lung development," *Adv. Anat. Embryol. Cell Biol.*, vol. 236, pp. 131–150, 2023.

[3] E. Reyssat and L. Mahadevan, "Hygromorphs: From pine cones to biomimetic bilayers," *Journal of The Royal Society Interface*, vol. 6, no. 39, 951–957, 2009. DOI: 10.1098/rsif.2009.0184.

[4] A. B. Rebocho, J. R. Kennaway, J. A. Bangham, and E. Coen, "Formation and shaping of the antirrhinum flower through modulation of the cup boundary gene," *Current Biology*, vol. 27, no. 17, 2610–2622.e3, 2017, ISSN: 0960-9822. DOI: 10.1016/j.cub.2017.07.064. [Online]. Available: https://doi.org/10.1016/j.cub.2017.07.064.

[5] E. Sharon, M. Marder, and H. L. Swinney, "Leaves, flowers and garbage bags: Making waves," *American Scientist*, vol. 92, no. 3, pp. 254–261, 2004.

[6] G Anner, *Planar processing primer*. Springer Science & Business Media, 2012.

[7] S. Akamine, T. Albrecht, M. Zdeblick, and C. Quate, "A planar process for microfabrication of a scanning tunneling microscope," *Sensors and Actuators A: Physical*, vol. 23, no. 1, pp. 964–970, 1990, Proceedings of the 5th International Conference on Solid-State Sensors and Actuators and Eurosensors III, ISSN: 0924-4247. DOI: https://doi.org/10.1016/0924-4247(90)87070-Y. [Online]. Available: https://www.sciencedirect.com/science/article/pii/092442479087070Y.

[8] J. Kemmer, "Improvement of detector fabrication by the planar process," *Nuclear Instruments and Methods in Physics Research Section A: Accelerators, Spectrometers, Detectors and Associated Equipment*, vol. 226, no. 1, pp. 89–93, 1984, ISSN: 0168-9002. DOI: https://doi.org/10.1016/0168-9002(84)90173-6. [Online]. Available: https://www.sciencedirect.com/science/article/pii/0168900284901736.

[9] A. E. Del Grosso and P. Basso, "Deployable structures," *Advances in science and technology*, vol. 83, pp. 122–131, 2013.

[10] J Santiago-Prowald and H Baier, "Advances in deployable structures and surfaces for large apertures in space," *CEAS Space Journal*, vol. 5, pp. 89–115, 2013.

[11] P. Liyanage and H. Mallikarachchi, "Origami based folding patterns for compact deployable structures," in *Proceedings of 4th International Conference on Structural Engineering and Construction Mangement*, vol. 10, 2013, pp. 4139–0082.

[12] H. Huang, Z. Deng, and B. Li, "Mobile assemblies of large deployable mechanisms," *Journal of Space Engineering*, vol. 5, no. 1, pp. 1–14, 2012.

[13] D. Dureisseix, "An overview of mechanisms and patterns with origami," *International Journal of Space Structures*, vol. 27, no. 1, pp. 1–14, 2012.

[14] J. Zavodnik, Y. Wang, W. Yan, M. Brojan, and M. K. Jawed, "Soft kirigami composites for form-finding of fully flexible deployables," *Advanced Materials Technologies*, vol. 9, no. 1, p. 2 300 909, 2024.

[15] K. Sim, S. Chen, Z. Li, *et al.*, "Three-dimensional curvy electronics created using conformal additive stamp printing," *Nature Electronics*, vol. 2, no. 10, pp. 471–479, 2019.

[16] J. H. Pikul, S. Li, H. Bai, R. T. Hanlon, I. Cohen, and R. F. Shepherd, "Stretchable surfaces with programmable 3d texture morphing for synthetic camouflaging skins," *Science*, vol. 358, no. 6360, pp. 210–214, 2017.

[17] Y. Wang, S. Hu, T. Xiong, Y. Huang, and L. Qiu, "Recent progress in aircraft smart skin for structural health monitoring," *Structural Health Monitoring*, vol. 21, no. 5, pp. 2453–2480, 2022.

[18] J. Betts, "John harrison: Inventor of the precision timekeeper," *Endeavour*, vol. 17, no. 4, pp. 160–167, 1993.

[19] A. M. Abdullah, X. Li, P. V. Braun, J. A. Rogers, and K. J. Hsia, "Kirigami-inspired self-assembly of 3d structures," *Advanced Functional Materials*, vol. 30, no. 14, p. 1 909 888, 2020.

[20] L. Ionov, "Biomimetic hydrogel-based actuating systems," *Advanced Functional Materials*, vol. 23, no. 36, pp. 4555–4570, 2013.

[21] J. J. Wie, M. R. Shankar, and T. J. White, "Photomotility of polymers," *Nature communications*, vol. 7, no. 1, p. 13 260, 2016.

[22] X. Ni, H. Luan, J.-T. Kim, *et al.*, "Soft shape-programmable surfaces by fast electromagnetic actuation of liquid metal networks," *Nature communications*, vol. 13, no. 1, p. 5576, 2022.

[23] E. Siéfert, E. Reyssat, J. Bico, and B. Roman, "Bio-inspired pneumatic shape-morphing elastomers," *Nature materials*, vol. 18, no. 1, pp. 24–28, 2019.

[24] D. Ambrosi, M. Ben Amar, C. J. Cyron, *et al.*, "Growth and remodelling of living tissues: Perspectives, challenges and opportunities," *Journal of the Royal Society Interface*, vol. 16, no. 157, p. 20 190 233, 2019.

[25] L. Zhang, S. Chizhik, Y. Wen, and P. Naumov, "Directed motility of hygroresponsive biomimetic actuators," *Advanced Functional Materials*, vol. 26, no. 7, pp. 1040–1053, 2016.

[26] J. Cui, F. R. Poblete, and Y. Zhu, "Origami/kirigami-guided morphing of composite sheets," *Advanced Functional Materials*, vol. 28, no. 44, p. 1 802 768, 2018.

[27] J. J. Park, P. Won, and S. H. Ko, "A review on hierarchical origami and kirigami structure for engineering applications," *International Journal of Precision Engineering and Manufacturing-Green Technology*, vol. 6, pp. 147–161, 2019.

[28] X. Ning, X. Wang, Y. Zhang, *et al.*, "Assembly of advanced materials into 3d functional structures by methods inspired by origami and kirigami: A review," *Advanced Materials Interfaces*, vol. 5, no. 13, p. 1 800 284, 2018.

[29] T. Tachi, "Geometric considerations for the design of rigid origami structures," in *Proceedings of the International Association for Shell and Spatial Structures (IASS) Symposium*, Elsevier Ltd Shanghai, China, vol. 12, 2010, pp. 458–460.

[30] E. A. P. Hernandez, D. J. Hartl, E. Akleman, and D. C. Lagoudas, "Modeling and analysis of origami structures with smooth folds," *Computer-Aided Design*, vol. 78, pp. 93–106, 2016.

[31] B. Y. Ahn, D. Shoji, C. J. Hansen, E. Hong, D. C. Dunand, and J. A. Lewis, "Printed origami structures," *Advanced Materials*, vol. 22, no. 20, pp. 2251–2254, 2010.

[32] A. Lamoureux, K. Lee, M. Shlian, S. R. Forrest, and M. Shtein, "Dynamic kirigami structures for integrated solar tracking," *Nature communications*, vol. 6, no. 1, p. 8092, 2015.

[33] N. An, A. G. Domel, J. Zhou, A. Rafsanjani, and K. Bertoldi, "Programmable hierarchical kirigami," *Advanced Functional Materials*, vol. 30, no. 6, p. 1 906 711, 2020.

[34] Y. Tang, Y. Li, Y. Hong, S. Yang, and J. Yin, "Programmable active kirigami metasheets with more freedom of actuation," *Proceedings of the National Academy of Sciences*, vol. 116, no. 52, pp. 26 407–26 413, 2019.

[35] B. Davidovitch, R. D. Schroll, D. Vella, M. Adda-Bedia, and E. A. Cerda, "Prototypical model for tensional wrinkling in thin sheets," *Proceedings of the National Academy of Sciences*, vol. 108, no. 45, pp. 18 227–18 232, 2011.

[36] G. M. Grason and B. Davidovitch, "Universal collapse of stress and wrinkle-to-scar transition in spherically confined crystalline sheets," *Proceedings of the National Academy of Sciences*, vol. 110, no. 32, pp. 12 893–12 898, 2013.

[37] B. Davidovitch, Y. Sun, and G. M. Grason, "Geometrically incompatible confinement of solids," *Proceedings of the National Academy of Sciences*, vol. 116, no. 5, pp. 1483–1488, 2019.

[38] Z. Fan, Y. Yang, F. Zhang, *et al.*, "Inverse design strategies for 3d surfaces formed by mechanically guided assembly," *Advanced Materials*, vol. 32, no. 14, p. 1 908 424, 2020.

[39] M. Liu, L. Domino, and D. Vella, "Tapered elasticæ as a route for axisymmetric morphing structures," *Soft Matter*, vol. 16, no. 33, pp. 7739–7750, 2020.

[40] Y. Yoon, H. Shin, D. Byun, *et al.*, "Neural probe system for behavioral neuropharmacology by bi-directional wireless drug delivery and electrophysiology in socially interacting mice," *Nature Communications*, vol. 13, no. 1, p. 5521, 2022.

[41] J. Kim, A. S. Campbell, B. E.-F. de Ávila, and J. Wang, "Wearable biosensors for healthcare monitoring," *Nature biotechnology*, vol. 37, no. 4, pp. 389–406, 2019.

[42] A. J. Bandodkar, P. Gutruf, J. Choi, *et al.*, "Battery-free, skin-interfaced microfluidic/electronic systems for simultaneous electrochemical, colorimetric, and volumetric analysis of sweat," *Science advances*, vol. 5, no. 1, eaav3294, 2019.

[43] J. Conde, N. Oliva, Y. Zhang, and N. Artzi, "Local triple-combination therapy results in tumour regression and prevents recurrence in a colon cancer model," *Nature materials*, vol. 15, no. 10, pp. 1128–1138, 2016.

[44] *Hansa mouse plush*, https://hansatoystore.com/products/Mouse-Gray-5579.

[45] *3m*, https://www.3m.com/.

[46] C. V. Rocha, V. Gonçalves, M. C. da Silva, M. Bañobre-López, and J. Gallo, "Plga-based composites for various biomedical applications," *International Journal of Molecular Sciences*, vol. 23, no. 4, p. 2034, 2022.

[47] G. Surendran and A. P. Sherje, "Cellulose nanofibers and composites: An insight into basics and biomedical applications," *Journal of Drug Delivery Science and Technology*, vol. 75, p. 103 601, 2022.

[48] J. Ragain, D Umsted, B Morrow, C Powell, L Legrand, D Chavis, *et al.*, "Effects of aging and denture cleansers on the flexural strength and surface microhardness of two flexible denture materials," *Int J Dent Oral Health*, vol. 1, no. 6, pp. 476–481, 2015.

[49] X. Wang, A. Khara, and C. Chen, "A soft pneumatic bistable reinforced actuator bioinspired by venus flytrap with enhanced grasping capability," *Bioinspiration & Biomimetics*, vol. 15, no. 5, p. 056 017, 2020.

[50] P. Fiers, D. De Clercq, V. Segers, and P. Aerts, "Biomechanics of human bipedal gallop: Asymmetry dictates leg function," *Journal of Experimental Biology*, vol. 216, no. 7, pp. 1338–1349, 2013.

[51] D. M. Boston and A. F. Arrieta, "Multistable honeycomb architecture for spanwise wing morphing," in *AIAA Scitech 2021 Forum*, 2021, p. 0479.

[52] S. Sengupta and S. Li, "Harnessing the anisotropic multistability of stacked-origami mechanical metamaterials for effective modulus programming," *Journal of Intelligent Material Systems and Structures*, vol. 29, no. 14, pp. 2933–2945, 2018.

[53] J. Shi, H. Mofatteh, A. Mirabolghasemi, G. Desharnais, and A. Akbarzadeh, "Programmable multistable perforated shellular," *Advanced Materials*, vol. 33, no. 42, p. 2 102 423, 2021. DOI: https://doi.org/10.1002/adma.202102423. eprint: https://onlinelibrary.wiley.com/doi/pdf/10.1002/adma.202102423. [Online]. Available: https://onlinelibrary.wiley.com/doi/abs/10.1002/adma.202102423.

[54] P. Zhang and B. Tang, "A two-finger soft gripper based on bistable mechanism," *IEEE Robotics and Automation Letters*, vol. 7, no. 4, pp. 11 330–11 337, 2022.

[55] Y. Chi, Y. Li, Y. Zhao, Y. Hong, Y. Tang, and J. Yin, "Bistable and multistable actuators for soft robots: Structures, materials, and functionalities," *Advanced Materials*, vol. 34, no. 19, p. 2 110 384, 2022.

[56] A. Pal, V. Restrepo, D. Goswami, and R. V. Martinez, "Exploiting mechanical instabilities in soft robotics: Control, sensing, and actuation," *Advanced Materials*, vol. 33, no. 19, p. 2 006 939, 2021.

[57] Z. Zhang, X. Ni, H. Wu, *et al.*, "Pneumatically actuated soft gripper with bistable structures," *Soft Robotics*, vol. 9, no. 1, pp. 57–71, 2022.

[58] D. K. Patel, X. Huang, Y. Luo, *et al.*, "Highly dynamic bistable soft actuator for reconfigurable multimodal soft robots," *Advanced Materials Technologies*, vol. 8, no. 2, p. 2 201 259, 2023.

[59] Z.-S. Yao, Z. Tang, and J. Tao, "Bistable molecular materials with dynamic structures," *Chemical communications*, vol. 56, no. 14, pp. 2071–2086, 2020.

[60] W. Huang, X. Ma, O. Sato, and D. Wu, "Controlling dynamic magnetic properties of coordination clusters via switchable electronic configuration," *Chem. Soc. Rev.*, vol. 50, pp. 6832–6870, 12 2021. DOI: 10.1039/D1CS00101A. [Online]. Available: http://dx.doi.org/10.1039/D1CS00101A.

[61] K. Tai, A.-R. El-Sayed, M. Shahriari, M. Biglarbegian, and S. Mahmud, "State of the art robotic grippers and applications," *Robotics*, vol. 5, no. 2, p. 11, 2016.

[62] J. Shintake, V. Cacucciolo, D. Floreano, and H. Shea, "Soft robotic grippers," *Advanced materials*, vol. 30, no. 29, p. 1 707 035, 2018.

[63] L. Birglen and T. Schlicht, "A statistical review of industrial robotic grippers," *Robotics and Computer-Integrated Manufacturing*, vol. 49, pp. 88–97, 2018.

[64] Z. Samadikhoshkho, K. Zareinia, and F. Janabi-Sharifi, "A brief review on robotic grippers classifications," in *2019 IEEE Canadian Conference of Electrical and Computer Engineering (CCECE)*, IEEE, 2019, pp. 1–4.

[65] B. K. Wada, J. L. Fanson, and E. F. Crawley, "Adaptive structures," *Journal of Intelligent Material Systems and Structures*, vol. 1, no. 2, pp. 157–174, 1990.

[66] D. Wagg, I. Bond, P. Weaver, and M. Friswell, *Adaptive structures: engineering applications*. John Wiley & Sons, 2008.

[67] M. Mungekar, L. Ma, W. Yan, V. Kackar, S. Shokrzadeh, and M. K. Jawed, "Design of bistable soft deployable structures via a kirigami-inspired planar fabrication approach," *Advanced Materials Technologies*, vol. 8, no. 16, p. 2 300 088, 2023. DOI: https://doi.org/10.1002/admt.202300088. eprint: https://onlinelibrary.wiley.com/doi/pdf/10.1002/admt.202300088. [Online]. Available: https://onlinelibrary.wiley.com/doi/abs/10.1002/admt.202300088.

[68] *Astm d412*, https://www.astm.org/d0412-16r21.html.

[69] B. Kim, S. B. Lee, J. Lee, *et al.*, "A comparison among neo-hookean model, mooney-rivlin model, and ogden model for chloroprene rubber," *International Journal of Precision Engineering and Manufacturing*, vol. 13, pp. 759–764, 2012.

[70] M. Pezzulla, G. P. Smith, P. Nardinocchi, and D. P. Holmes, "Geometry and mechanics of thin growing bilayers," *Soft matter*, vol. 12, no. 19, pp. 4435–4442, 2016.

[71] D. K. Patel, X. Huang, Y. Luo, *et al.*, "Highly dynamic bistable soft actuator for reconfigurable multimodal soft robots," *Advanced Materials Technologies*, vol. 8, no. 2, p. 2 201 259, 2023. DOI: https://doi.org/10.1002/admt.202201259. eprint: https://onlinelibrary.wiley.com/doi/pdf/10.1002/admt.202201259. [Online]. Available: https://onlinelibrary.wiley.com/doi/abs/10.1002/admt.202201259.

[72] Y. Augenstein and C. Rockstuhl, "Inverse design of nanophotonic devices with structural integrity," *ACS photonics*, vol. 7, no. 8, pp. 2190–2196, 2020.

[73] Y Mao, Q He, and X Zhao, *Designing complex architectured materials with generative adversarial networks. sci. adv. 6, eaaz4169*, 2020.

[74] J. Wang, Y. Wang, and Y. Chen, "Inverse design of materials by machine learning," *Materials*, vol. 15, no. 5, p. 1811, 2022.

[75] J. Panetta, F. Isvoranu, T. Chen, E. Siéfert, B. Roman, and M. Pauly, "Computational inverse design of surface-based inflatables," *ACM Transactions on Graphics (TOG)*, vol. 40, no. 4, pp. 1–14, 2021.

[76] Z. Liu, D. Zhu, S. P. Rodrigues, K.-T. Lee, and W. Cai, "Generative model for the inverse design of metasurfaces," *Nano letters*, vol. 18, no. 10, pp. 6570–6576, 2018.

[77] R. Xue, R. Li, Z. Du, *et al.*, "Kirigami pattern design of mechanically driven formation of complex 3d structures through topology optimization," *Extreme Mechanics Letters*, vol. 15, pp. 139–144, 2017.

[78] Z. Liu, D. Zhu, L. Raju, and W. Cai, "Tackling photonic inverse design with machine learning," *Advanced Science*, vol. 8, no. 5, p. 2 002 923, 2021.

[79] J. Noh, G. H. Gu, S. Kim, and Y. Jung, "Machine-enabled inverse design of inorganic solid materials: Promises and challenges," *Chemical Science*, vol. 11, no. 19, pp. 4871–4881, 2020.

[80] Y. Dan, Y. Zhao, X. Li, S. Li, M. Hu, and J. Hu, "Generative adversarial networks (gan) based efficient sampling of chemical composition space for inverse design of inorganic materials," *npj Computational Materials*, vol. 6, no. 1, p. 84, 2020.

[81] L. Ma, M. Mungekar, V. Roychowdhury, and M. Jawed, "Rapid design of fully soft deployable structures via kirigami cuts and active learning," *Advanced Materials Technologies*, vol. 9, no. 5, p. 2 301 305, 2024. DOI: https://doi.org/10.1002/admt.202301305. eprint: https://onlinelibrary.wiley.com/doi/pdf/10.1002/admt.202301305. [Online]. Available: https://onlinelibrary.wiley.com/doi/abs/10.1002/admt.202301305.

[82] P. Z. Hanakata, E. D. Cubuk, D. K. Campbell, and H. S. Park, "Forward and inverse design of kirigami via supervised autoencoder," *Phys. Rev. Res.*, vol. 2, p. 042 006, 4 2020. DOI: 10.1103/PhysRevResearch.2.042006. [Online]. Available: https://link.aps.org/doi/10.1103/PhysRevResearch.2.042006.

[83] R. Danhaive and C. T. Mueller, "Design subspace learning: Structural design space exploration using performance-conditioned generative modeling," *Automation in Construction*, vol. 127, p. 103 664, 2021, ISSN: 0926-5805. DOI: https://doi.org/10.1016/j.autcon.2021.103664. [Online]. Available: https://www.sciencedirect.com/science/article/pii/S0926580521001151.

[84] M. Mungekar, M. R. Shankar, and M. K. Jawed, "Directed shape morphing using kirigami-enhanced thermoplastics," [Unpublished manuscript].

[85] Giudici, A., Clement, A., Duffy, D. L., Shankar, M. Ravi, and Biggins, J. S., "Multiple shapes from a single nematic elastomer sheet activated via patterned illumination," *EPL*, vol. 140, no. 3, p. 36 003, 2022. DOI: 10.1209/0295-5075/ac9e19. [Online]. Available: https://doi.org/10.1209/0295-5075/ac9e19.

[86] OpenAI, *Dall-e 3: Generating images from text*, 2024. [Online]. Available: https://www.openai.com/research/dall-e-3.